Simulating the neutral hydrogen distribution during cosmic reionization

A dissertation presented in partial fulfilment of the requirements for the degree of Doctor of Philosophy

in the Department of Physics and Astronomy

University of the Western Cape.

By:

Sultan HASSAN

Supervisor:
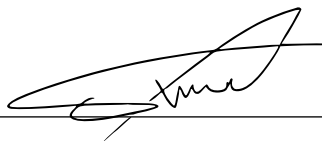
Prof. Romeel DAVÉ

March 2018

Declaration

The work presented in thesis is accomplished by the author under the supervision of Romeel Davé (University of the Western Cape/University of Edinburgh) and in collaboration with Kristian Finlator (New Mexico State University), Mario Santos (University of the Western Cape/SKA Office), Benedetta Ciardi (Max Planck Institute for Astrophysics), Sourav Mitra (Surendranath College). This collaboration resulted in the following peer-reviewed publications:

- **Hassan, S.**, Davé, R., Finlator, K., Santos, M., *Simulating the 21-cm signal from reionisation including non-linear ionisations and inhomogeneous recombinations*, 2016, MNRAS, 457, 1550

- **Hassan, S.**, Davé, R., Finlator, K., Santos, M., *Epoch of Reionisation 21cm Forecasting From MCMC-Constrained Semi-Numerical Models*, 2017, MNRAS, 468, 122

- **Hassan, S.**, Davé, R., Mitra, S., Finlator, K., Ciardi, B., Santos, M., *Constraining the contribution of active galactic nuclei to reionisation*, 2018, MNRAS, 473, 227

Chapters of this thesis are re-formulated reprints of these publications.

I hereby declare that this thesis has not been submitted to any university for a degree, and all of the work in this thesis, save for that which is properly acknowledged, is my own.

Signed: _____

Date: **16 March 2018**

Abstract

We improve on the physical treatment of ionising source and sink populations in the large scale semi-numerical simulations by implementing new physically motivated parametrizations taken from high-resolution radiative transfer simulations, in order to account for the non-linear dependence on halo mass, redshift and environment. This provides an efficient unique way to connect the small scale astrophysics to the large scale cosmology. These new parametrizations allow the model to simultaneously match all current reionization observations with only 4% photon escape fraction. These improvements result in 2-3 $\times$ 21cm power spectrum variations on small and large scales, and hence showing the importance of accurately treating ionising sources and sinks in 21cm simulations. We further implement time-integrated effects to accurately track the evolution of ionising photons, inhomogeneous recombinations and partially ionized regions during reionization. Including these effects yields larger H II regions and a more sudden reionization, which leads to an order of magnitude more 21cm power on large scales. We develop a robust parameter estimation pipeline to constrain the model astrophysical parameters against several reionization observations. We find that future 21cm observations provide tighter constraints on the astrophysical parameters and complement different derived constraints from other reionization observations. We finally employ the high redshift observations to add ionising photons from Active Galactic Nuclei (AGN), in order to assess the ability of AGN-dominated models to solely complete reionization. Unlike the case with galaxies, the AGN-only models cannot simultaneously match all current reionization observations. AGN-only models produce 21cm power spectrum that is 2 $\times$ higher on all scales as compared with galaxies-dominated models. Future 21cm surveys will play a key role to distinguishing between these two scenarios, even though AGN are highly unlikely to drive cosmic reionization.

Acknowledgements

I would like to express my deepest gratitude to my advisor, Romeel Davé, for his incredible support, continuous encouragement, and patient guidance through my PhD journey. He provided me with an excellent atmosphere for doing research. His valuable comments significantly contributed to my academic growth in all aspects including writing skills and future career plans. I have learned so much from him and I truly cannot thank him enough!.

Grateful thanks go to my collaborator Kristian Finlator for his continued support during my PhD. He generously hosted me during my visit to New Mexico State University, from which I have learned so many things through the interesting discussions we had. I am thankful to my collaborator Mario Santos for his great assistance and support, particularly in the early stages of my PhD, which helped me to understand the difficult parts of his simulation algorithm. I am thankful to my collaborator Benedetta Ciardi for hosting my long term visit at the Max Planck Institute of Astrophysics and for her caring, interesting discussions and comments. I would also like to thank Sourav Mitra for his wonderful collaboration and assistance during the third project of my PhD.

I am grateful to all members of the astrophysics group at University of the Western Cape including the group head Roy Maartens, faculty staff, postdocs, and my fellow post graduate students (Takalani, Eliab, Mahmoud, Emanuele) whose jokes and lovely characters made the office we share very enjoyable to overcome stressful times during the research work. Special thanks go to Michelle Gabler for her kind assistance on all administrative matters related to my PhD. I am also grateful to all group members of the Centre for extragalactic centre including Mika, Daniel, Nicole, Vimal, and Margherita for their discussions and comments during our group meetings.

I am thankful to the HERA members at University of Pennsylvania, James Aguirre, Saul Kohn, Paul La Plante, and Adam Lidz as well as Adrian Liu from University of California Berkeley for their wonderful collaboration during my participation in the HERA exchange program, 2017. I am thankful to Garrelt Mellema for the interesting conversations and hosting my visit at Stockholm University. I am also thankful to Andrei Mesinger, Greig Bradley, Jonathan Pober, Suman Majumdar, Girish Kulkarni, Tirthankar Roy Choudhury, Neal Katz, Jonathan Chardin, Yuxiang Qin, Jonathan Zwart for their helpful discussions.

iii

Contents

UNIVERSITY *of the*

WESTERN CAPE

List of Figures

List of Tables

"In the beginning there was nothing, which exploded."
Terry Pratchett

Chapter 1

Introduction

Over the last few decades, cosmology has entered the so-called "golden age", in which theoretical speculations have transformed into precise measurements and observational scientific facts through the great advances in the modern experiments' capabilities. These facts include the accidental discovery of cosmic microwave background (CMB), the expansion of the Universe, Nucleosynthesis of the light elements, formation of galaxies and large scale structure; all together forming the pillars of the standard model of big bang cosmology.

The standard big bang model presents a historical scenario of the universe at different epochs and the evolution of the universe through to the present day. In this model, the universe began with a big bang explosion of an extremely high density and temperature state before approximately 14 billion years ago. The universe then expanded super-luminously during the inflationary epoch. As the temperature decreases due to the expansion, the elementary basic building blocks of our universe started to form, marking the beginning of the Nucleosynthesis era. At that time, the universe contained a highly-ionised plasma state of electrons and protons. Recombination epoch began when the first electrons and protons recombined to form neutral atoms. During this epoch, the CMB photons were emitted from the last-scattering surface which specifies the horizon of the universe. The universe then entered the dark ages till the formation of the first luminous cosmic objects about 300 Myr after the big bang. This thesis focuses on this important time in the history of the universe, which is the Epoch of Reionization (EoR).

1

The EoR marks a period in the early universe, during which the birth of first luminous cosmic structures gradually reionized the neutral Hydrogen in the Intergalactic Medium (IGM). The EoR represents the last major global phase transition by which the Universe underwent from cold, opaque and highly neutral into hot, transparent and fully ionized. As an intermediate phase between the dark ages and the current transparent Universe, the EoR carries deep insights into early Universe structure formation. This epoch therefore captures a wealth of cosmological and astrophysical information about the nature of the first luminous cosmic structures as well as early stages of galaxy formation and evolution.

The EoR remains poorly constrained since it is far beyond the detection capabilities of current experiments. For this reason, it has been decided by 2010 Decadal survey committee (National Research Council, 2010) that the priority science objectives for the current and next decade experiments is to search for first stars, galaxies and black holes, and hence better constraining the EoR physics. In this light, many ongoing and forthcoming radio interferometer experiments such as the Low Frequency Array (LOFAR)[1], the Hydrogen Epoch of Reionization Array (HERA)[2], and the Square Kilometer Array (SKA)[3], are promising to detect reionization on large cosmological scales in the near future.

Reionization is a complex process which combines various small scale astrophysical and large scale cosmological effects (Barkana & Loeb, 2001; Loeb & Barkana, 2001). It begins with the formation of the first luminous collapsed objects, such as stars and black holes, due to the gravitational instability in the initial density field fluctuations that were magnified by cosmological inflation. As the Universe expands, the temperature decreases and induces the formation of more collapsed objects, including the luminous candidates responsible for reionization, in regions with density higher than average. Ionising photons travels from the core of these luminous objects, through the Interstellar medium (ISM), to eat away the neutral Hydrogen in the IGM. Through this journey, the ionising photons possibly experience scattering or absorption in the ISM due to the remaining neutral density clumps and the recombination from pre-ionised regions. This process continues till enough photons are produced to balance the recombination in the ISM and ionise the whole neutral gas in the IGM. This shows that reionization is, in fact, an evolving battle between ionising source and sink populations.

---

[1]http://www.lofar.org/

[2]http://reionization.org

[3]https://www.skatelescope.org

The current theoretical consensus suggests that reionization occurred in three different phases. The first is the pre-overlap phase during which the ionising sources are rare and forming slowly isolated ionised regions in their surroundings. With the formation of more ionising sources, the Universe enters the overlap phase. In this phase, the mean free path of the ionising photons increases such that the ionised bubbles significantly grow and intersect to form larger ionised bubbles. The final post-overlap phase begins when the IGM is almost ionised. The ionising photons here are absorbed by the final filaments and dense clouds in the remaining optically thick and self-shielding regions such as Lyman-Limit Systems (LLS).

1.1   Observational Constraints

Currently, there is a number of indirect observational constraints on cosmic reionization. The first constraint is on the IGM neutral fraction by end of reionization, which comes from the observations of high-redshift quasars. In these observations, a forest of Ly-α absorption lines appears in quasars spectrum as an evidence for neutral Hydrogen in the IGM at high-redshift. Gunn & Peterson (1965) speculated that a neutral IGM can be seen in quasars spectrum as an absorption trough. The first clear Gunn-Peterson (GP) trough was then observed by Becker et al. (2001) in a z=6.28 quasar spectrum from the Sloan Digital Sky Survey[4], where the absorption trough extends from z=5.95 to z=6.15. Using a larger SDSS sample of 19 high-redshift quasars, Fan et al. (2006b) found that the GP absorption optical depth evolves strongly towards high redshifts with complete deep troughs only appear at z > 6.1. They concluded that the presence of these deep troughs at z > 6 implies a substantial change in the IGM evolution, in the same manner as expected by end of reionization. Their work sets an upper limit on the IGM neutral fraction from $\sim 10^{-4}$ to 10^{-3} at z $\sim$ 5-6. More recent and similar work by Becker et al. (2015) using an extended sample of high-redshift quasars, found deep troughs down to z = 5.5 which indicates a slightly late end of reionization by z=5 with a constraint on the IGM neutral fraction of $\sim 10^{-5}$. Another robust model-independent constraint is provided in the work by McGreer et al. (2015) in which they use the dark pixel analysis in a large sample of high-redshift quasars. These analysis considers only zero measured flux (dark) pixels and requires no further assumptions about the IGM physical condition. This constraint sets an

---

[4]http://www.sdss.org/

upper limit on the neutral fraction of $\leq 0.06+0.05$ at z = 5.9 and $\leq 0.04+0.05$ at z = 5.6. Although some caution is needed against over-interpreting these observations (Mesinger, 2010), all these constraints suggest that reionization was (nearly) complete by z∼6.

Second constraint is placed on the photoionization rate Γ, or equivalently, the ionising emissivity $\dot{N}_{\rm ion}$ by end of reionization. Bolton & Haehnelt (2007) used a suite of hydrodynamics simulations combined with IGM Ly-α measurements (Songaila, 2004; Fan et al., 2006b) and found that the $\dot{N}_{\rm ion}$, at $2 \leq$ z ≤ 6, can be best characterized following a redshift-dependent power law expression, $\dot{N}_{\rm ion}(z){=}10^{50.5-0.06({\rm z}-6)}$ s^{-1} Mpc^{-3}, that slowly increases the emissivity towards lower redshifts, assuming a constant photon escape fraction of $f_{\rm esc} = 20\%$. Using a combined set of Ly-α forest, WMAP-7 and galaxy survey data, Kuhlen & Faucher-Giguére (2012) found exactly the opposite that the ionising emissivity increases to higher redshifts from z = 2 in order to maintain the observed photoionization rate, corresponding to an increase in the photon escape fraction from $f_{\rm esc} = 4\%$ at z = 4 up to $f_{\rm esc} = 100\%$ at the beginning of reionization. Recently, Becker & Bolton (2013) have provided new measurements of the ionising emissivity that are based on their refined measurements to the mean transmitted flux using 6065 quasars spectra taken from SDSS data release 7. They find a flat slope of the photoionization rate over $2 \leq$ z ≤ 5, whereas the emissivity (and the photon escape fraction $f_{\rm esc}$) increases from z $\sim$ 3 - 5, corresponding to 5 ionising photons per atom per gigayear at z = 4.75, consistent with Kuhlen & Faucher-Giguére (2012) and Haardt & Madau (2012) estimates.

The third constraint, which governs the size of ionized regions and opacity of neutral regions, is the mean free path ($\lambda^{912}_{\rm mpf}$) of ionising photons. The mean free path is defined as the proper distance that ionizing photons can freely travel before experiencing (1/e) attenuation (e.g. absorption or scattering). This corresponds to $\sim$ 37% photons attenuation for a medium with an unity mean free path. In the beginning of reionization, the mean free path is almost zero since the universe was fully neutral. As reionization progresses, the mean free path increases rapidly till it is set by the distribution of the remaining neutral filamentary structure by end of reionization. Past attempts (e.g. Meiksin & Madau, 1993; Madau et al., 1999) have combined Ly-α forest opacity distribution measurements with the photoionization rate estimates from quasars spectra, to infer a mean free path of $\lambda^{912}_{\rm mpf} \sim 40$ to 150 h^{-1}_{70} Mpc by z = 3. Using a stacking analysis on ensemble of

quasars taken from SDSS, Prochaska et al. (2009) have placed direct constraints on the mean free path; yielding $\lambda_{\mathrm{mpf}}^{912} \sim 50\ h_{72}^{-1}$ Mpc at z $= 3-4$. Another attempt by Fumagalli et al. (2013) using a similar stacking technique have found that $\lambda_{\mathrm{mpf}}^{912}$ $= 100 \pm 29\ h_{70.4}^{-1}$ at z $= 3$. The most recent updated constraints are provided by the Giant Gemini GMOS (GGG) survey (Worseck et al., 2014) which obtained large sample of 164 quasars at high-redshift (z > 4.4). The result of this survey showed a rapid evolution of the mean free path during z $\sim 4.5-5.2$ with $\lambda_{\mathrm{mpf}}^{912} \approx$ 10 Mpc at z $= 5.2$. All constraints on $\lambda_{\mathrm{mpf}}^{912}$ confirm that the universe was highly ionised by z ~ 5.

The Cosmic Microwave Background (CMB) observations provide the fourth constraint on the reionization history, through the integrated optical depth to Thomson scattering of CMB photons by the free electrons due to reionization. This scattering results in a large scale CMB polarization, which carries useful insights on the initial condition of the early Universe, and hence constraining the onset of reionization. On small scales, the kinetic Sunyaev & Zel'dovich (1980) effect takes place as a result of inverse Compton scattering of CMB photons by the motion of ionized regions, and hence constraining the reionization topology. The Nine-Year Wilkinson Microwave Anisotropy Probe (WMAP) CMB observations constrained the cosmological parameters (Hinshaw et al., 2013) and obtained a reionization optical depth of $\tau = 0.088 \pm 0.013$, corresponding to an early reionization by $z_{reion} \approx 10$. The Planck (2015) collaboration constrained the optical depth to $\tau = 0.066 \pm 0.016$, much lower than previous WMAP value, with a later reionization redshift $z_{reion} \approx 8$. The recent revision of reionization constraints by Planck (2016) has reported a much lower optical depth of $\tau = 0.058 \pm 0.012$, corresponding to reionization redshift range form $z_{reion} \approx 7.8$-8.8, with a shorter reionization duration upper limit of $\Delta z < 2.8$. These updated results, assuming several reionization models, suggest that approximately 10% of Universe was globally reionized before z $= 10$, and hence strongly disfavoring an early onset of reionization.

There are also other indirect constraints on reionization, including the IGM thermal history, ionising photon escape fraction, high-redshift galaxies and quasars luminosity functions, and metal abundance and evolution (for extensive review on reionization constraints see Loeb & Barkana, 2001; Ciardi & Ferrara, 2005; Fan et al., 2006; Zaroubi, 2013). However, these indirect constraints provide information about some quantities (e.g. neutral fraction, ionising emissivity) that mainly

characterize the late stages of reionization, but are unable to directly constrain the reionization process.

The most promising probe of cosmic reionization is expected from future 21cm observations (e.g. LOFAR, HERA, SKA). The 21cm line results from a hyperfine transition in the neutral hydrogen, due to a flip in the electron and proton spin orientation. The 21cm line is a forbidden transition with extremely low decay rate, and yet it is the most important tool to probe the early universe, simply because the hydrogen is the most abundant element in the universe, and hence huge 21cm emissions are expected. The 21cm brightness temperature is directly proportional to the density and ionization fields. This implies that the 21cm line carries a mixture of astrophysical information from the ionization process in the neutral gas from luminous sources, and cosmological information from the underlying density field originated from the initial seed perturbation. The 21cm signal then provides a possibility to explore the large scale structure in a three-dimensional space of neutral gas and density distribution. Future 21cm observations will enable imaging of the neutral hydrogen distribution on large cosmological scales during reionization. This will provide direct constraints on the actual reionization process and will reveal the nature and effect of first cosmic structures. For these reasons, this thesis focuses on creating more accurate predictions for future 21cm experiments, through improving the underlying astrophysics implemented in current models of reionization.

1.2 Modelling Cosmic Reionization

An intrinsic challenge for theoretical models of reionization lies in the ability to reproduce simultaneously various reionization key observables, and translate them into constraints on the astrophysical and cosmological parameters. The proper modelling of reionization requires a very high resolution to evolve radiation from ionising sources in sub-kpc scales up to the large Mpc scales of the IGM. Unfortunately, it is beyond our current computational capabilities to efficiently perform this task. For this reason, different models are usually limited to explain (few) different observational constraints, and no current model can fully satisfy all reionization modelling demands.

Currently, there are four ways to modelling reionization. First, semi-analytical models (e.g. Choudhury & Ferrara, 2005; Mitra et al., 2011) are powerful in constraining the globally averaged evolution of the IGM physical properties (e.g. thermal and reionization history) during reionization. Due to the lack of the dynamic range, these models cannot address details of reionization (e.g. ionized bubbles shapes and clumping effects) nor predicting 21cm fluctuations. Second, full radiative transfer hydrodynamics simulations (Finlator et al., 2009; Pawlik & Schaye, 2008) might be the most accurate approach to model reionization. These simulations evolve the gravity, hydrodynamics and radiation self-consistently and simultaneously with high-resolution in a particle based manner. They also achieve high accuracy of photon conservation and are able to match simultaneously various reionization and galaxy formation constraints at high and low redshift. Unfortunately, they are very expensive to run, and hence their dynamic range is usually limited to ≤ 25 Mpc. This small range allows them to study several aspects in the IGM evolution during reionization (e.g feedback effects and metal absorbers), but preventing them to evolve the 21cm signal onto large cosmological scales ($\geq$ 500 Mpc). Third, post-processed radiative transfer simulations (e.g. Mellema et al, 2006; McQuinn et al, 2007; Iliev et al., 2014) can evolve the radiation field on a grid of density and sources in order to probe larger scales, but do not self-consistently account for variety of feedback effects (e.g. thermal, ionisation, and chemical) that impact galaxy formation and evolution, and hence impacting the photoionization production rate. Fourth, semi-numerical models of reionization are the tool used in this thesis, which will be briefly reviewed next.

1.2.1 Semi-numerical models of reionization

The advantage of using semi-numerical models (Mesinger & Furlanetto, 2007; Zahn et al, 2007; Choudhury et al., 2009; Santos et al., 2010) over radiative transfer hydrodynamic simulations is the ability to evolve the 21cm fluctuations on very large cosmological scales with extremely low computational cost. To date, these models maybe regarded as the most efficient approach to probe reionization and its redshifted 21cm fluctuations. However, these simulations have a limited resolution due to applying various set of approximations, particularly to form dark matter halos and ionized regions from the underlying density fields, such as the excursion set-formalism (Bond et al., 1991), but nevertheless they appear to be in a good

agreement with radiative transfer simulations (Majumdar et al., 2014; Zahn et al., 2011).

At early times, the density field $\delta(x)$ falls into the linear regime, which can be characterized by a random Gaussian distribution. Assuming a dark matter power spectrum $P(k)$ (e.g. Eisenstein & Hu, 1998), cells in a density box of size L are assigned values (a_k and b_k) randomly drawn from a Gaussian field with a zero mean and unit variance in the Fourier space as follows:

$$\delta(k) = \sqrt{\frac{L^3 P(k)}{2}}\,(a_k + ib_k). \tag{1.1}$$

The density field in the real space is simply found by taking the inverse Fourier transforms of the above. Using the first-order approximation of the perturbation theory, the linear velocity field, whose gradient is equivalent to the obtained density field, can be directly generated. The linear density field can then be evolved to the non-linear regime via applying the standard Zel'dovich (1970) approximations, in which the displacement vector of the density grid positions is directly proportional to the velocity field.

Dark matter halos are identified using the excursion-set formalism. In this formalism, halos can form in regions with density higher than critical overdensity $\delta_c(z) \sim 1.68/D(z)$, where $D(z)$ is the growth factor. Taking into account ellipticity in modelling the gravitational collapse (Sheth et al., 2001; Sheth & Tormen, 1999), the critical overdensity $\delta_c(z)$ becomes a function of the filter scale as follows:

$$\delta_c(M, z) = \sqrt{a}\,\delta_c(z)\left[1 + b\left(\frac{\sigma^2(M)}{a\,\sigma_c^2(z)}\right)^c\right], \tag{1.2}$$

where a, b and c are fitting parameters. The idea is to smooth the non-linear density field around a point x on the grid space, and this point becomes a center of halo with mass M if $\delta_c(M, x) > \delta_c(M, z)$ is satisfied. This method is repeated, starting with the maximum smoothing scale (comparable to the box size) down to the cell size, till all halos are generated. The positions of halos are also corrected at high-redshift, using the Zel'dovich (1970) approximations similar to the density field.

The ionization field is also identified using a similar form of the excursion-set formalism. The main difference is that the ionized regions can overlap, whereas halos are not allowed to. The excursion-set barrier (the ionization condition) for

a region to self-ionize is based on the efficiency parameter ζ. For each spherical region specified by the excursion-set formalism, a region is considered to be fully ionised if

$$f_{coll}(x, M, z) \geq \zeta^{-1}, \tag{1.3}$$

where f_{coll} is the fraction of the collapsed matter (ratio between total halo mass to total dark matter mass). In this process, regions are flagged as fully neutral or fully ionised, motivated by the fact that the ionization front is usually sharp and partial ionization might not be resolved on large cosmological scales (Mellema et al, 2006; Majumdar et al., 2014). Once the ionization field is generated, the 21cm brightness temperature can be obtained as follow:

$$\delta T_b(\nu) = 23 x_{HI} \Delta \left(\frac{\Omega_b h^2}{0.02} \right) \sqrt{\frac{1+z}{10} \frac{0.15}{\Omega_m h^2}} \left(\frac{H}{H + dv/dr} \right) mK, \tag{1.4}$$

where dv/dr is the comoving gradient of the line of sight component of the comoving velocity. This expression valid only under the assumption that the spin temperature is much higher than the CMB temperature (e.g $z < 10$).

1.3 Thesis overview

In this thesis, I aim to improve on the underlying astrophysics implemented in the semi-numerical model, SimFast21, written by Santos et al. (2010), in order to provide more accurate 21cm predictions for future radio interferometer experiments. I also plan to develop a novel parameter estimation pipeline to calibrate the improved model against several reionization observations, and to perform 21cm forecasting for future experiments. Finally, I develop a new model of Active Galactic Nuclei (AGN) in order to study the difference between AGN and Galaxy scenarios. Next, I present a summary of each chapter with main conclusions.

In Chapter 1, I have first improved the density field distribution in the vanilla SimFast21 by implementing a Cloud-in-Cells smoothing, where each cell contributes to 8 eight neighbouring cells, instead of the previously adopted Nearest Grid Point assignment. For the first time in the semi-numerical modelling, I have implemented new physically motivated recipes for treating the ionising source and sink populations in the original SimFast21. These recipes are taken from high-resolution radiative hydrodynamic simulations (Finlator et al., 2015) in order to

account for the non-linearly mass-dependence and redshift-dependence in ionising sources evolution as well as various feedback processes that are usually neglected in the semi-numerical models. This new semi-numerical model is able to reproduce simultaneously various EoR constraints with only 4% photon escape fraction, which is remarkable. I have shown that implementing these relations result in 21cm power variation by a factor of $\times$ 2-3 on small and large scales (Hassan et al., 2016). This indicates the importance of accurately treating ionising sources and sinks in simulating the 21cm signal.

In Chapter 2, I have developed a robust parameter estimation pipeline (Hassan et al., 2017), using the Markov chain Monte Carlo (MCMC) method in order to calibrate the improved models' astrophysical parameters (e.g. photon escape fraction, ionising emissivity amplitude and halo mass dependence) against several reionization constraints. I have performed a detailed 21cm forecasting for LOFAR, HERA, and SKA based on their final proposed configurations. I have found that the SFR, Planck 2016 optical depth, and ionising emissivity data somewhat constrain our free parameters, while future 21cm observations provide much tighter constraints. The SimFast21-MCMC platform developed here will be useful to a wide range of EoR forecasting science cases by providing an opportunity to incorporate new data in order to set tighter constraints on the astrophysical parameters.

In Chapter 3, I have implemented a new method to populate AGN in the improved model that is based on Giallongo et al. (2015) observed luminosity function at z=5.75, and evolved to higher redshift using a fixed Quasar Halo Occupancy Distribution. This model has been developed in order to participate in the current debate of AGN versus galaxies reionization scenarios. I have found that an AGN-only model cannot simultaneously match observations of optical depth, neutral fraction, and ionising emissivity (Hassan et al., 2018). I have also found that future 21cm observations could potentially discriminate between these two scenarios. All these results suggest that AGN are highly unlikely to dominate the photon ionising budget required for reionization.

Chapter 2

Simulating the 21-cm signal from reionisation including non-linear ionisations and inhomogeneous recombinations

Abstract

We explore the impact of incorporating physically motivated ionisation and recombination rates on the history and topology of cosmic reionisation and the resulting 21-cm power spectrum, by incorporating inputs from small-volume hydrodynamic simulations into our semi-numerical code, SimFast21, that evolves reionisation on large scales. We employ radiative hydrodynamic simulations to parameterize the ionisation rate R_{ion} and recombination rate R_{rec} as functions of halo mass, overdensity and redshift. We find that R_{ion} scales super-linearly with halo mass ($R_{\mathrm{ion}} \propto M_h^{1.41}$), in contrast to previous assumptions. Implementing these scalings into SimFast21, we tune our one free parameter, the escape fraction f_{esc}, to simultaneously reproduce recent observations of the Thomson optical depth, ionizing emissivity, and volume-averaged neutral fraction by the end of reionisation. This yields $f_{\mathrm{esc}} = 4^{+7}_{-2}\%$ averaged over our $0.375h^{-1}$Mpc cells, independent of halo mass or redshift, increasing to 6% if we also constrain to match the observed $z = 7$ star formation rate function. Introducing super-linear R_{ion} increases the duration of reionisation and boosts small-scale 21-cm power by $\times 2 - 3$ at intermediate

phases of reionisation, while inhomogeneous recombinations reduce ionised bubble sizes and suppress large-scale 21-cm power by $\times 2 - 3$. Gas clumping on sub-cell scales has a minimal effect on the 21cm power. Super-linear $R_{\rm ion}$ also significantly increases the median halo mass scale for ionising photon output to $\sim 10^{10} {\rm M}_\odot$, making the majority of reionising sources more accessible to next-generation facilities. These results highlight the importance of accurately treating ionising sources and recombinations for modeling reionisation and its 21-cm power spectrum.

2.1   Introduction

The epoch of reionisation (EoR) is the last global phase transition of the Universe, during which the birth of first luminous sources gradually ionised the intergalactic medium (IGM). Given that this epoch remains mostly unexplored, current EoR studies are devoted to answering its most basic questions: When did the EoR begin? What are the sources responsible for driving reionisation? How did the topology of reionisation evolve? When did the EoR end? Accurate answers for these questions are crucial to understand the early stages of galaxy formation and evolution.

Observations of the high-redshift quasars' Lyα absorption spectra (Becker et al., 2001; Fan et al., 2006) suggest that reionisation of the IGM completed about $z \sim 6$, though there is some evidence for variations in this (Pentericci et al., 2014; Becker et al., 2015; Chardin et al., 2015). The recent cosmic microwave background (CMB) polarization measurements by Planck (2015) reported a Thomson electron scattering optical depth out to the surface of last scattering of 0.066, lower than previous measures by WMAP (Hinshaw et al., 2013), thus reducing the need for exotic ionising sources within high redshift star-forming galaxies (Robertson et al., 2015). These observations constrain the topology, sources, and evolution of the EoR, albeit only crudely. The detailed evolution of spatially-inhomogeneous reionisation involves a complex interplay between evolving source populations, the propagation of ionising photons within a patchy IGM, and the enrichment of the first galaxies and halos that may affect the nature of the ionising sources.

A promising approach to tracking the evolution of neutral hydrogen during the EoR is via its emission in the redshifted hyperfine 21-cm line. The advantage

of using the 21-cm line is that its brightness temperature is directly proportional to neutral gas content (x_{HI}) which makes it possible to study the three-dimensional distribution of the neutral gas and the large scale structure during the EoR (Barkana & Loeb, 2001; Furlanetto et al., 2006). Hence the EoR is a key science goal for current and future low-frequency (~ 150 MHz) radio telescopes. These experiments include the Low Frequency Array (LOFAR)[1], the Murchison Widefield Array (MWA)[2], the Precision Array to Probe Epoch of Reionisation (PAPER)[3], the Hydrogen Epoch of Reionisation Array (HERA)[4] and eventually the Square Kilometer Array (SKA-Low) [5]. Owing to the relatively coarse angular resolution at these long wavelengths, interpreting these observations fully requires understanding how small-scale processes such as the production and propagation of ionising photons impact the large-scale neutral gas distribution.

To this end, numerous theoretical studies have focused on modeling the EoR process and its expected 21-cm signal. A key limiting factor is the need for vast dynamic range that remains a computational challenge. Proper cosmological simulations of the EoR must resolve the smallest proto-galaxies to track the local generation and propagation of the ionizing photons, as well as their recombinations which requires modeling the small-scale clumping of gas, from sub-kpc scales up to the sizes of the largest ionising bubbles during the late stages of the EoR, believed to be tens of Mpc (e.g. Sobacchi & Mesinger, 2014). This requires both large-volume simulations together with extremely high resolution. For instance, the forthcoming EoR surveys by SKA-Low will span a field-of-view of about 10 degrees that corresponds to a size of ~ 500 Mpc with ~ 0.5 Mpc resolution (Iliev et al., 2015), while the proto-galaxies that are thought to provide the dominant source of ionising photons likely have scale sizes below a kpc (e.g. Tilvi et al., 2013).

Early hydrodynamic simulations of the EoR applied post-processed radiative transfer to cosmologically-evolved density fields (e.g. Gnedin, 2000; Razoumov et al, 2002; Mellema et al, 2006; McQuinn et al, 2007; Thomas et al, 2009; Iliev et al., 2014; Bauer et al., 2015), which enabled the study of reionisation topology but did not self-consistently include the feedback effects of the ionisation on galaxies. More recent codes such as MARCH (Finlator et al., 2009, 2013) and TRAPHIC (Pawlik &

---

[1]http://www.lofar.org/

[2]http://www.haystack.mit.edu/ast/arrays/mwa/

[3]http://w.astro.berkeley.edu/ dbacker/eor/

[4]http://reionisation.org

[5]https://www.skatelescope.org

Schaye, 2008) have been developed to do full radiative hydrodynamics in a cosmo-logical galaxy formation code, including feedback processes constrained to match available high-z data (Finlator et al., 2011). Unfortunately, these simulations are computationally very expensive, and the requirement that the simulation resolve to below the hydrogen cooling halo mass limit of $\sim 10^8 M_\odot$ drives one to a quite small box size (see however So et al 2014; Gnedin 2014), typically $\lesssim 10$ Mpc.

A complementary approach is to use a large volume ($\gtrsim 100$ Mpc) simulations that employ physically-motivated parameterizations to determine the location and evo-lution of the source population, even though they do not resolve individual galaxy sources. These so-called semi-numerical models have low computational cost since they do not require radiative transfer and they determine the density field evolution from analytic prescriptions such as excursion set formalism (Mesinger & Furlan-etto, 2007; Zahn et al, 2007; Choudhury et al., 2009; Santos et al., 2010). A key free parameter in such codes is the ionizing efficiency per unit (halo) mass, gener-ally assumed to be constant and tuned to match key observations. Semi-numerical models have been shown to roughly reproduce the ionisation history and 21-cm power spectrum as obtained from radiative hydrodynamic simulations (Zahn et al., 2011; Majumdar et al., 2014). However, the simplicity of the source param-eterisations and the fact that they neglect recombinations means that they fail to account for all of the relevant inhomogeneous physical processes required to properly address the problem.

Sobacchi & Mesinger (2014) have recently improved their semi-numerical code by incorporating inhomogeneous recombinations using a sub-grid prescription that self-consistently tracks the evolution of ionizing sources and recombination sys-tems, as well as accounting for feedback effects. While an improvement over previous semi-numerical work, the parameterisations are obtained without self-consistently accounting for galactic feedback processes, and hence still employ a constant efficiency parameter (i.e. ionising photon rate per unit dark matter halo mass M_h) to characterise the source population. In contrast, radiative hydro-dynamic simulations tuned to match high-z galaxy properties find that the star formation rate, and hence relatedly the ionising photon rate, scales super-linearly with halo mass at these epochs, typically as $M_h^{1.3-1.4}$ (Finlator et al., 2011). Fur-thermore, the clumping factor that controls the recombination rate is set by a com-plex interplay between photon propagation as a function of environment, which is

best followed using full radiative hydrodynamic simulations (e.g. Finlator et al., 2012). Hence there remains room for improvement in semi-numerical EoR models.

In this chapter we aim to take the next step by implementing calibrated relations for the non-linearly mass-dependent ionisation efficiency and inhomogeneous recombination rates taken from high-resolution radiative hydrodynamic (RT) simulations into the semi-numerical EoR code SimFast21 (Santos et al., 2010). We use simulations from Finlator et al. (2015) that have been previously calibrated to match various observations of galaxies at high redshifts. We derive new parametrizations for the non-linear ionisation (R_{ion}) and recombination (R_{rec}) rates directly from this radiative hydrodynamic simulation as a function of halo mass and redshift, complemented by a larger-volume galaxy formation simulation without radiative transfer to help bridge the small scales in the RT simulation to the large-scale semi-numerical model. We implement these new formulae for R_{ion} and R_{rec} that track the evolution of the non-linear ionisations and inhomogeneous recombinations into SimFast21. We constrain our one free model parameter, the escape fraction, to simultaneously match observations of the Planck Thomson optical depth, the late evolution of the Lyman alpha mean opacity, and the ionising emissivity at $z \sim 5$. Finally, we make predictions for the expected 21-cm power spectrum from the EoR, and particularly investigate how our new physical parameterisations alter the predicted signal. This new version of our SimFast21 is publicly available[6].

This chapter is organized as follows: In section 2.2, we introduce the simulations used, namely SimFast21, the radiative hydrodynamic simulations, and the non-radiative larger-volume simulation. In section 2.3, we present our new parametrizations of R_{rec} and R_{ion} from hydrodynamic simulations. We present our key observables in section 2.4, explore the impact of our new parameterisations in section 2.5 and conclude in section 2.6. Throughout this work, we adopt a ΛCDM cosmology in which $\Omega_{\mathrm{M}} = 0.3$, $\Omega_{\Lambda} = 0.7$, $h \equiv H_0/(100\,\mathrm{km/s/Mpc}) = 0.7$, a primordial power spectrum index $n = 0.96$, an amplitude of the mass fluctuations scaled to $\sigma_8 = 0.8$, and $\Omega_b = 0.045$. We quote all results in comoving units, unless otherwise stated.

---

[6]https://github.com/mariogrs/Simfast21

2.2 Simulations

We describe SimFast21 (Santos et al., 2010) and, in particular, focus on how the ionized regions are identified using a fixed efficiency parameter. We then briefly describe the two complementary suites of the state-of-the-art hydrodynamic simulations, namely a high-resolution radiative hydrodynamic simulation (**6/256-RT**; Finlator et al., 2015), and a larger-volume cosmological hydrodynamic simulation without radiative transfer (**32/512**; Davé et al., 2013), which we employ to obtain new parametrizations of the non-linear ionisation and inhomogeneous recombination rates. A summary of our simulations is shown below in Table 2.1.

2.2.1 SimFast21

SimFast21 is a semi-numerical code that predicts the redshifted 21-cm signal from cosmic reionisation. SimFast21 simulation uses a Monte-Carlo approach to evolve the density field from a Gaussian random initial state to form collapsed structures based on a spherical collapse density threshold. This prescription generally follows the algorithm described in Mesinger & Furlanetto (2007), which we briefly review here.

At very high redshift, the dark matter density field is distributed linearly onto a grid, and the linear gravitational corrections are added by applying the Zel'dovich (1970) approximation to evolve to lower redshifts. The collapsed dark matter halos are specified using the excursion-set formalism with an overdensity threshold of $\delta_c(z) \sim 1.68/D(z)$, where $D(z)$ is the linear growth factor.

Ionized regions are identified using a similar form of the excursion-set algorithm, based on the assumption of a constant efficiency parameter of ionising photon per unit halo mass, ζ. The ionisation condition for any given region is simply the amount of collapsed dark matter halo f_{coll} compared with the efficiency parameter ζ. In other words, the region is considered to be fully ionized if:

$$f_{coll} \geq \zeta^{-1}, \tag{2.1}$$

and fully neutral if not. For single cells which are not covered by ionised bubbles, we set their ionised fraction to $f_{coll}\zeta$. Using this condition, the ionisation field is generated that is the main input required to compute the predicted 21-cm signal.

ζ encapsulates a mixture of the ionisation and recombination processes such as ionising radiation escape fraction and recombinations by Lyman Limit Systems (LLS). However, it implicitly assumes that the recombinations trace the halos in the same way as the ionisations, which is unlikely to be true in detail. Nonetheless, ζ can be tuned to match observations and yield predicted 21-cm power spectra.

In §2.3.3 we will describe our improvements to this scheme. In particular, we aim to improve the following aspects from the previous version of SimFast21:

- No explicit modeling of recombinations. Recombinations are only implicitly modeled via the constant efficiency parameter, which does not account for inhomogeneities in the density field and the local clumping factor.

- The use of a constant efficiency parameter. We will show that this is not an optimal description of the ionisation rate as a function of halo mass.

- Regions identified as fully ionised are set to have a neutral fraction of zero. More realistically, they should have a small neutral fraction appropriate for an optically-thin portion of the Universe in ionisation equilibrium.

- The density field spatial distribution. The original code uses nearest grid point assignment of density field to cells, but this can result in a biased density field distribution with unexpected voids when applying the Zel'dovich (1970) approximation.

A typical run with SimFast21 will have a volume of several hundred Mpc and a cell size of several hundred kpc. Hence this method cannot resolve the galaxies that are the sources of ionising photons in the EoR, nor the clumped density field that governs recombinations. Therefore, to develop a better sub-grid model for these processes, we need to employ high-resolution hydrodynamic simulations of galaxy formation that can resolve these processes directly. Next we describe these hydrodynamic simulations.

2.2.2 6/256-RT simulation

To resolve the smallest significantly star-forming halos, we use the recent radiative transfer cosmological hydrodynamic simulation described more fully in Finlator et al. (2015). This simulation uses the Gadget-3 Smoothed Particle Hydrodynamics

(SPH) code (Springel, 2005), merged with the radiative transfer code MARCH (Finlator et al., 2009, 2012) to run a fully self-consistent radiative hydrodynamic simulation of early galaxy formation. Built on the version of GADGET developed by Oppenheimer & Davé (2008), this code incorporates well-constrained models for star formation-driven feedback processes, that do a generally good job of matching observed lower-redshift galaxy and IGM properties (Oppenheimer & Davé, 2008; Davé, Oppenheimer, & Finlator, 2011; Davé, Finlator, & Oppenheimer, 2011; Davé et al., 2013).

The particular run we use, which we will call **6/256-RT**, employs a small volume of $6h^{-1}$Mpc and evolves 2×256^3 particles. The mass of each gas particle is $2.3 \times 10^5 \mathrm{M}_\odot$ whereas the dark matter particle is about $5.6\times$ more massive. We therefore can resolve halos down to hydrogen cooling limit at $10^8 \mathrm{M}_\odot$ with 65 (dark matter+gas) particles, and galaxies down to stellar masses of $7.4 \times 10^6 \mathrm{M}_\odot$ with 32 gas particles. The equivalent Plummer gravitational softening length employed is 469 pc (comoving), corresponding to around 50 physical pc at the epoch of interest. It is crucial that our simulation resolves halos down to the hydrogen cooling limit, and therefore should be resolving essentially all the ionising photon output during the EoR under the assumption that halos below the hydrogen cooling limit do not contribute substantially to the photon budget, as is now generally believed (e.g. Wise & Cen, 2009).

This simulation also includes a subgrid Monte Carlo model for kinetic galactic outflows, following the "ezw" prescription described in Davé et al. (2013). The two free parameters are the mass loading factor η and wind speed v_w, which vary with galaxy velocity dispersion σ that is calculated using an on-the-fly friends-of-friends galaxy identification code. The ezw prescription employs momentum-driven wind scalings ($v_w \propto \sigma$ and $\eta \propto \sigma^{-1}$) in sizable galaxies ($\sigma > 75\,\mathrm{kms}^{-1}$), and energy driven scalings ($\eta \propto \sigma^{-2}$) in dwarf galaxies. To mock up outflows blowing channels through the interstellar medium (ISM), hydrodynamic forces are turned off until either the particle reaches 10% of SF critical density or a time of $1.95 \times 10^{10}/(v_\mathrm{w}(\mathrm{kms}^{-1}))$ yr has passed. These scalings result in many predictions for galaxy and IGM properties that agree reasonably well with observations (Somerville et al., 2015). This version of GADGET also includes a model for chemical enrichment following Type II and Type Ia supernovae and stellar evolution, as well as primordial and metal cooling. The star formation model follows the multi-phase model in Springel & Hernquist (2003b), with a density threshold

of $n_{\rm H} = 0.13$ cm^{-3}. A Chabrier (2003) initial mass function (IMF) is assumed throughout. Radiative cooling follows the prescription in Katz et al. (1996) to include the primordial cooling, and Sutherland & Dopita (1993) collisional ionisation equilibrium tables to account for cooling from metal lines.

The radiative transfer is done during the simulation run on a grid of 32^3 voxels, and its evolution is tracked using a moment-based method, together with a long characteristics code periodically employed to calculate the Eddington tensor in each cell in order to close the moment hierarchy (Finlator et al., 2011). The non-equilibrium ionisation state of the gas is followed by interpolating the ionisation field to the location of each gas particle. Sixteen separate frequency groups are followed, evenly spaced between $1 - 10$ Ryd.

While the code is high resolution by cosmological standards, it lacks sufficient resolution to directly predict the escape of ionising photons from star-forming regions. Hence there is still an assumption required for the escape fraction of ionising photons, $f_{\rm esc}$. In this run, a mass- and redshift-dependent $f_{\rm esc}$ is employed, which results in $f_{\rm esc} = 0.8$ in halos with mass $M_{\rm h} < 10^8 M_\odot$, dropping with both mass and time to around 5% at $z = 5$ in more massive halos; the full formula is in equation 1 of Finlator et al. (2015).

Finlator et al. (2015) showed that this simulation, with its $f_{\rm esc}$ as assumed, can simultaneously match two key EoR observations, namely the optical depth to Thomson scattering from the Wilkinson Microwave Anisotropy Probe (WMAP; Hinshaw et al., 2013) polarization-temperature cross-correlation, and the volume-averaged neutral fraction at $z \sim 6$ (Fan et al., 2006) measured from the Lyα forest. Hence it is a plausible model for the evolution of the ionising background during the EoR.

As an important aside, we point out an inconsistency in this chapter regarding our assumed $f_{\rm esc}$: We will use this RT simulation's output to provide a description for the ionising photon rate that we will implement into SimFast21, but then we will re-tune $f_{\rm esc}$ in our semi-numerical runs to a substantially different value than what was assumed in the RT simulation. Ideally, we would re-run our RT simulation with the new $f_{\rm esc}$, and iterate until convergence. Beyond the prohibitive computational cost to do so, there is a more fundamental reason why this is not feasible: The volume of our RT simulation is too small to fully capture even the moderately massive halos that (as we show later) contribute significantly to the

ionising photon budget particularly during the latter stages of the EoR. Therefore, the $f_{\rm esc}$ used in the RT simulation is tuned to high values at early stages of the EoR to compensate for those missing halos. However, the critical input from RT simulation is the slope of the star formation rate – halo mass (SFR$-M_h$) relation (SFR $M_h^{1.3-1.4}$), which is sensitive to feedback from stellar energy and the UVB at low masses. Hence it is appropriate to boost the $f_{\rm esc}$ in the RT simulation in order to model a realistic UVB evolution, as this in turn yields a more realistic SFR(M_h, z) prediction. Although the $f_{\rm esc}$ assumed in the RT simulation is not self-consistent, the fact that it reproduces key EoR observables including the UV luminosity function means that it likely represents a plausible evolution for the ionising photon output and neutral gas density field over the scales that are modeled. Hence while at present there is no practical way to avoid this inconsistency, it nonetheless provides an appropriate characterisation of the parameters we need for our large-scale modeling.

2.2.3 32/512 simulation

While the RT simulation described above accurately follows the interplay between photoionisation and galaxy formation, it lacks the volume to produce sufficiently large halos that are an important contributor to reionisation. Since we want to evolve large volumes with SimFast21, we would like to have an "intermediate" sized simulation that effectively bridges the gap, and allows the computation of ionisation and recombination rates in more massive halos. For this purpose, we will use a larger-volume cosmological hydrodynamic simulation that does not include radiative transfer. As discussed in Finlator et al. (2012), radiative transfer effects are only important in "photo-sensitive" halos with $M_h \lesssim 10^{9.3} M_\odot$, and hence we will only utilize this simulation for halos larger than this.

The simulation we employ has been fully described in Davé et al. (2013); here we review the basic details. This simulation uses the Gadget-2 N-body+SPH code (Springel, 2005) to model a cubic volume of $32 h^{-1}$Mpc on a side and 512^3 particles of dark matter and gas each; we refer to this as our **32/512** run. Each gas particle has a mass of about $4.5 \times 10^6 M_\odot$, allowing us to resolve galaxies down to stellar masses of around $M_{*,\rm lim} = 1.4 \times 10^8 M_\odot$, and halo masses of around $10^9 M_\odot$.

Most of the physics is identical to the RT run, including the radiative cooling, star formation following Springel & Hernquist (2003), the chemical evolution model,

and the "ezw" prescription for galactic outflows. One difference is that, unlike in the RT run, ionisation equilibrium is assumed throughout, taking a spatially-uniform ionising background as given by Haardt & Madau (2001). Also, this simulation includes a model to quench star formation in massive galaxies, but this does not come into play at the early epochs that we consider here.

The overall strategy is to parameterise the ionisation and recombination rates taken from the **6/256-RT** and **32/512** runs, and insert those parameterisations into SimFast21. Next we describe how this is done.

2.3 Parameterizing ionisations and recombinations

We aim to obtain new parameterizations of $R_{\rm ion}$ and $R_{\rm rec}$ that capture environmental and feedback effects directly from the **32/512** and **6/256-RT** simulations, in order to implement them into SimFast21. To begin, we must determine the ionisation and recombination rates of our simulated gas particles.

2.3.1 Ionisation Rate, $R_{\rm ion}$

To determine the ionisation rate of each gas particle, we take directly from the **6/256-RT** and **32/512** simulations output the star formation rate (SFR) and metallicity (Z). We then compute the ionisation rate using Equation (2) in Finlator et al. (2011), which is derived from Schaerer (2003) models. Given an ionisation photon output rate for each particle, we then sum this over all the star-forming gas particles within a given halo to determine $R_{\rm ion}$ for that halo.

In Figure 2.1, we show $R_{\rm ion}$ as a function of halo mass for halos at z = 6, 7, 8 (top to bottom panels). To increase dynamic range, we combine the **6/256-RT** (green dots) and **32/512** (blue dots) simulations, thereby covering dark matter halo masses of $M_h \sim 10^{8-11.5}$ $M_\odot$. Importantly, the values of $R_{\rm ion}$ among the two simulations is quite similar in the overlap region of $M_h \sim 10^{9.3-10} M_\odot$, with only a very slight tendency for the smaller volume to have higher $R_{\rm ion}$. At low halo masses ($M_h \lesssim 10^8 M_\odot$) we see a turn-down in $R_{\rm ion}$ owing to photo-suppression of galaxy formation (Finlator et al., 2011). At high masses, $R_{\rm ion}$ follows a power law
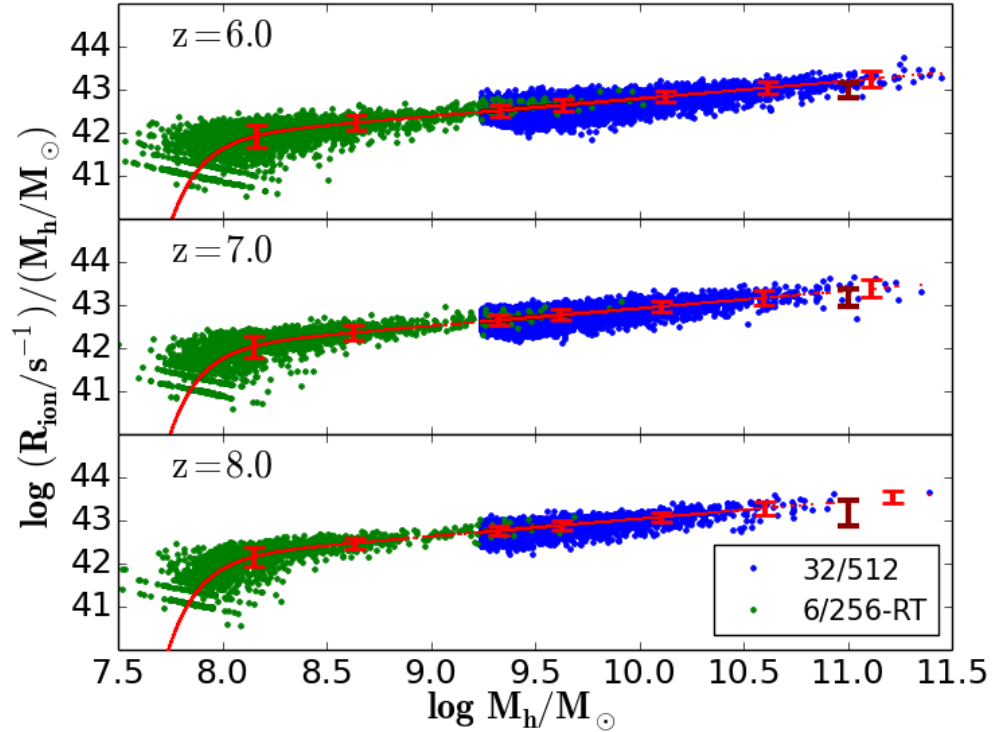
FIGURE 2.1: Ionization rate $R_{\rm ion}$ computed from **6/256-RT** (blue dots) and **32/512** (green) simulations. The overlap between **6/256-RT** and **32/512** simulations occurs in the halo mass range of $10^{9.3-10}$ $M_\odot$, and the two simulations yields similar results there. The red dots are computed using our fitting function, Equation (2.2). The red vertical error bars represent σ values for $\log M_{\rm h}$ bin size of 0.5. The scatter is fairly small, so is unlikely to systematically impact the 21-power spectrum. The dark red vertical error bars at 10^{11} $M_\odot$ are computed using SFR measurements from Behroozi et al. (2013). Our fitting function nicely reproduces the ionisation rate $R_{\rm ion}$ computed from our hydrodynamic simulations and only higher by a factor of $\times 1.5$ than Behroozi et al. (2013) observations.

that is approximately $R_{\rm ion} \propto M_h^{1.4}$, consistent with what the dependence on SFR with M_h found in similar simulations by Finlator et al. (2011).

The red vertical error bars show the 1σ scatter in $R_{\rm ion}$ in $\log M_{\rm h}$ bins of 0.5. At $M_{\rm h} = 10^{10} M_\odot$, $\sigma \sim 0.12$ independent of redshift. Note that when implementing $R_{\rm ion}$ into SIMFAST21, we will average over many halos in each cell which will reduce the scatter further, therefore the scatter is unlikely to systematically impact the 21-power spectrum. Qualitatively, introducing scatter in $R_{\rm ion}$ would introduce larger HII bubbles in diffuse regions and smaller ones in overdense ones, blurring the effect of the $R_{\rm ion}$ dependence on M_h and suppressing large-scale fluctuations. These effects are likely to be small given the small scatter, which only increases substantially at the lowest masses that (we will show later) are not driving reionisation. The key goal of the current work is to improve on previous work by

allowing R_{ion} to vary with halo mass in a physically-motivated way rather than assuming a constant value. We therefore defer a detailed investigation into the impact of scatter to future work.

To check if these simulated values for R_{ion} are reasonable, we compare to the SFR inferred from observations using abundance matching by Behroozi et al. (2013), shown as the dark red vertical error bars at 10^{11} M$_\odot$ (this is the lowest halo mass at which they computed the SFR). To convert from SFR to R_{ion}, we invert the process described above, assuming a metallicity corresponding to the mean metallicity of star-forming gas at that epoch. The agreement is within the quoted uncertainty by Behroozi et al. (2013), but in detail we see that our hydrodynamic simulations (**6/256-RT, 32/512**) produce an R_{ion} that is higher by a factor $\times 1.5$ compared to that inferred by Behroozi et al. (2013). We will return to this point in §2.4.1.

To implement R_{ion} into SimFast21, we construct a fitting function for $R_{ion}(M_h, z)$ whose mass dependence is analogous to a Schechter function, namely a power-law on one end and an exponential cutoff on the other, and whose redshift dependence is as a power law in the scale factor[7] , namely:

$$\frac{R_{ion}}{M_h} = A(1 + z)^D (M_h/B)^C \exp\left(-(B/M_h)^{3.0}\right). \tag{2.2}$$

We perform a minimization to determine the best-fit parameters to be $A = 1.08 \times 10^{40}$ M$_\odot^{-1}$s^{-1}, $B = 9.51 \times 10^7$ M$_\odot$, $C = 0.41$ and $D = 2.28$. Note that equation (2.2) shows that R_{ion} scales as $M_h^{1.41}$, which is consistent with the SFR$-$M$_h$ relation that previously found by Finlator et al. (2011).

We note that at low redshifts (e.g. today), the high-mass end of $R_{ion}(M_h)$ would likely have a sharp turn-down owing to quenching of star formation in $M_h \gtrsim 10^{12} M_\odot$ halos (e.g. Gabor et al., 2012). We do not produce such large halos by z = 6 in these hydro simulations, although it is possible that our SimFast21 volume will be sufficiently large to yield halos above this mass. Nonetheless, there are suggestions that the quenching mass scale is higher at high redshifts (e.g. Dekel et al., 2009; Gabor et al., 2014). For instance, the best-fit parameterisation of the equilibrium galaxy formation model in Mitra et al. (2015) suggests that at $z = 6$, the quenching mass scale is close to $M_h \sim 10^{15} M_\odot$, which is larger than any halo

---

[7]This is also taken from Francisco et al. (2014), where a similar formula used to parameterize the DLA cross-section; see their eq. (4.4).

existing during the EoR. Hence we ignore the possibility of a high-mass turn-down in $R_{\rm ion}$ for now.

2.3.2 Recombination Rate, $R_{\rm rec}$

Since the recombination rate $R_{\rm rec}$ depends on the density field and its clumping, we choose to parameterise $R_{\rm rec}$ per unit volume in terms of the local scaled density $\Delta \equiv \rho/\bar{\rho}$, where ρ is the matter density and $\bar{\rho}$ is the cosmic mean at that redshift. Then in SIMFAST21, we can apply this recombination rate to individual cells where we can compute the scaled density. Also, because we want to characterise the inhomogeneous recombination rate during the EoR, we can only use the full radiative hydrodynamic simulation for this, namely **6/256-RT**, and we do not employ the **32/512** run here. Unfortunately, this limits our dynamic range and requires a larger extrapolation to cover the range of overdensities that are achieved in our large SIMFAST21 volume, which is an unavoidable limitation given computational capabilities.

Since the clumping and hence $R_{\rm rec}$ is sensitive to scale (e.g. Finlator et al., 2013), we must choose a particular scale over which to compute Δ and hence $R_{\rm rec}$. Here we choose to subdivide our $6h^{-1}$Mpc simulation into 16 cells per side, which yields a cell size of 0.535 Mpc (comoving). This then necessarily fixes the cell size that we will use for our SIMFAST21 runs to a value that enables us to feasibly simulate sufficiently large volumes for computing the 21-cm power spectrum on the scales of relevance for current and upcoming observations. We smooth the mass of each gas particle onto these cells using a 5th-order B-spline kernel with 128 neighbours as utilised in the 6/256-RT simulation (Finlator et al., 2015).

Within each so-defined cell in the **6/256-RT** simulation, we compute the volume-averaged recombination rate density, $R_{\rm rec}/V$, as follows:

$$R_{\rm rec}/V = \alpha_{\rm a} < n_{\rm HII}\, n_{\rm e} >_{\rm V} /x_{\rm i}\,, \tag{2.3}$$

where $n_{\rm HII}$ is the ionized hydrogen number density, $n_{\rm e}$ is the free electrons number density, $x_{\rm i}$ is the cell's ionised volume fraction, and $\alpha_a = 4.2 \times 10^{13}{\rm cm}^3\,{\rm s}^{-1}$, that corresponds to a temperature of $10^4\,{\rm K}$. We consider case-A recombination following the recent paper by Kaurov & Gnedin (2014), where it has been shown that case-A recombination photons mimic the scenario of those photons redshifted
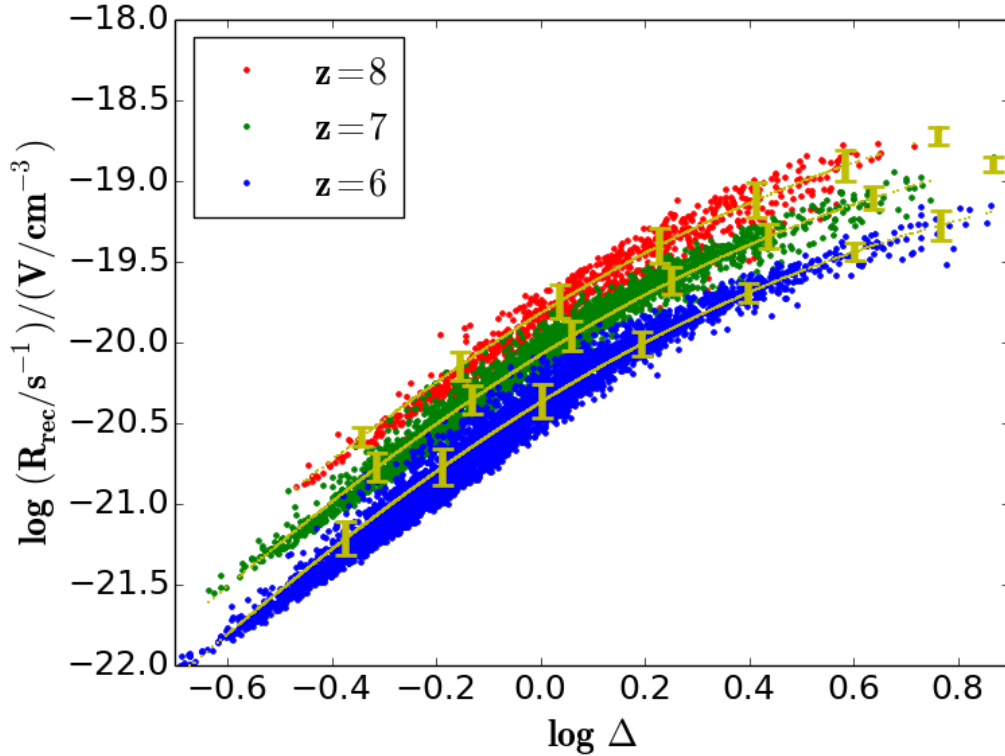
FIGURE 2.2: Recombination rate density R_{rec}/V computed from **6/256-RT** simulation at $z = 6$ (blue-dots), $z = 7$ (green-dots) and $z = 8$ (red-dots). Yellow dots show our fitting function, Equation (2.4). Vertical error bars represent 1σ values for $\log \Delta$ bin size of 0.2. The scatter is fairly small, so is unlikely to systematically impact the 21-power spectrum. It is quite clear that our fitting function fairly reproduces the recombination rate R_{rec} that is computed from our hydrodynamic simulations.

out of resonance, and therefore can no longer be ionising photons. We compute equation (2.3) only in cells above a specific ionisation threshold $x_i > 0.95$. This is because in our model, SimFast21 assumes that ionisations must overcome recombinations in fully ionized medium, once the ionisation condition is statisfied (eq. 2.5). Therefore, we want to make sure the recombinations rates computed from **6/256-RT** correspond to similarly ionised regions. Then we divide by x_i in equation (2.3) to correct for the residual neutral fraction.

Figure 2.2 shows the recombination rates per unit volume as a function of Δ at $z = 6, 7, 8$. The yellow vertical error bars represent the 1σ scatter in bins of $\log \Delta = 0.2$. At the mean density ($\Delta = 0$), the scatter is $\sigma \sim 0.1$, and is similar for different redshifts and Δ. We do not expect that this small scatter will have a significant impact on the derived 21-cm power spectrum. In general, $R_{rec} \propto \Delta^2$ as expected since recombination is a two-body process, though there is a slight

flattening at high-Δ. Recombination rates are also higher at higher z, since the Universe is denser.

We now determine a fitting function for the recombination rate density, $\mathrm{R_{rec}}/\mathrm{V}$. We construct a fitting function $\mathrm{R_{rec}}/\mathrm{V}(\Delta, z)$ as follows:

$$\frac{\mathrm{R_{rec}}}{\mathrm{V}} = \mathrm{A}(1+\mathrm{z})^{\mathrm{D}} \left[\frac{(\Delta/\mathrm{B})^{\mathrm{C}}}{1+(\Delta/\mathrm{B})^{\mathrm{C}}} \right]^4, \tag{2.4}$$

and we determine the best-fit values to be $\mathrm{A} = 9.85 \times 10^{-24}\mathrm{cm}^{-3}\mathrm{s}^{-1}$, $\mathrm{B} = 1.76$, $\mathrm{C} = 0.82$, $\mathrm{D} = 5.07$. Note that the redshift dependence is slightly weaker than the expected $(1+\mathrm{z})^6$ owing to the evolution of the clumping factor (Finlator et al., 2013). Although these fitting values are only applicable for the cell size that we have chosen, namely $0.375h^{-1}\mathrm{Mpc}$, we find that re-binning the hydrodynamical simulation using cells that are half as wide leads to an R_{rec} that is indistinguishable from our current fit. Furthermore, re-running our reionization simulations with smaller cells but otherwise the same parameters leads to essentially indistinguishable results. As will be seen later, the **Full** model, which uses the R_{rec} parameterization, and the **NoSubClump** model, which uses rather the local densities to compute recombinations, do produce similar ionization maps and 21cm power spectra. This shows that the clumping factor has a minimal impact on cosmological scales, even if R_{rec} is sensitive to cell size. Hence our results are not sensitive to this choice of cell size.

Equation (2.4) thus effectively accounts for the local clumping factor from the **6/256-RT** simulation, that we can implement into a SimFast21 simulation where such clumping cannot be resolved. We can thus compute the recombination rate R_{rec} in SimFast21 by multiplying the recombination rate density $\mathrm{R_{rec}}/\mathrm{V}$ by the SimFast21 cell volume.

2.3.3   Modifying SimFast21 to use R_{rec} and R_{ion}

To apply the fitting formulae for R_{rec} and R_{ion} in SimFast21, we first smooth the generated density field. The density field moves relative to the fixed SimFast21 grid cells as a consequence of applying the Zel'dovich (1970) approximation. We must then smooth the density field onto the grid cells during the evolution. Here we implement cloud-in-cell (CIC) smoothing, where each cell contributes to 8

Simulation	Size (h^{-1}Mpc)	No of Cells	Resolution (h^{-1}Mpc)
SIMFAST21	210	560^3	0.375
6/256-RT	6	16^3	0.375
32/512	32	-	-

TABLE 2.1: shows a summary of our simulations. We use **6/256-RT** simulation to computing both $R_{\rm rec}$ and $R_{\rm ion}$. We consider the **32/512** simulation only to computing $R_{\rm ion}$, and hence we don't divide the simulation box into cells.

neighbouring cells. We then apply the $R_{\rm rec}$ fitting formula (eq. 2.4) to the CIC-smoothed density field to generate our recombinations rate boxes. For $R_{\rm ion}$, we compute the CIC smoothing directly on the ionisation field that is generated using the halo catalogs via Equation (2.2).

Given $R_{\rm ion}$ and $R_{\rm rec}$ computed on the SIMFAST21 grid, we can now use this information to develop a new criterion for whether a particular region is neutral or ionised. To do so, we simply compare the local ionisation rate with recombination rate, and assign the bubble cells to be ionised if:

$$f_{\rm esc} R_{\rm ion} \geq R_{\rm rec} \, , \tag{2.5}$$

where $f_{\rm esc}$ is our assumed escape fraction. This replaces our previous criterion based on the efficiency parameter ζ (eq. 2.1).

We note that this criterion assumes that, once a particular region satisfies this criterion, it is quickly able to ionise the vast majority of its neutral gas. This is an approximation, but one expects that the increasing rate of ionising photon production in the early Universe together with the dropping cosmic density will in general yield a fast transition to being fully reionised. Indeed, such a quick transition is typically seen for entire simulation volumes (e.g. Gnedin, 2000, and we will later show this for our models as well), and it is physically reasonable to expect such rapid reionisation will also occur locally. To rigorously assess its validity we would need to do a full radiative transfer simulation, which we leave for future work.

In the original SIMFAST21, an ionised cell was set to $x_{\rm HII} = 1$. In reality, even a fully-reionised patch of the Universe has some small residual neutral fraction $f_{\rm resid}$, which depends on the global ionising background and overdensity (Hui & Gnedin, 1997). Hence when our ionisation criterion (eq. 2.5) is satisfied, we set the ionisation fraction to $x_{\rm HII} = 1 - f_{\rm resid}$, otherwise we leave it as $x_{\rm HII} = 0$.

We calculate f_resid as follows. First, we obtain the H I photoionisation rate Γ_HI, which corresponds to the flux of ionising photons, from Haardt & Madau (2012). Then, we compute the neutral fraction based on ionisation equilibrium following Popping et al. (2009), which results in

$$f_\mathrm{resid} = \frac{2C + 1 - \sqrt{(2C+1)^2 - 4C^2}}{2C} \, , \qquad (2.6)$$

with

$$C = \frac{n\beta(T)}{\Gamma_\mathrm{HI}} \, , \qquad (2.7)$$

and where n is the hydrogen number density, T is the gas temperature, and the recombination rate coefficient $\beta(T)$ function (Verner & Ferland, 1996) is given by

$$\beta(T) = a\Big[\sqrt{T/T_0}(1 + \sqrt{T/T_0})^{1-b}(1 + \sqrt{T/T_1})^{1+b}\Big]^{-1}. \qquad (2.8)$$

For neutral hydrogen, the best-fit parameters are $a = 7.982 \times 10^{-11}$ cm^{3}s^{-1}, $b = 0.7480$, $T_0 = 3.148$ K, and $T_1 = 7.036 \times 10^5$ K. We assume a temperature of $T = 10^4$ K at all times, since f_resid is only important at the end of reionisation where the universe becomes optically thin.

At the tail end of reionisation, this results in a non-zero x_HI, unlike in the original code. We note that this is not a direct prediction of this simulation, since it scales with the Γ_HI that we are taking from Haardt & Madau (2012) rather than predicting directly from the model. In the future we plan to do this more self-consistently, but since this has no effect for predicting the 21-cm power spectrum at epochs where reionisation is far from complete, for the present purposes our current prescription is sufficient.

To summarize, we have modifed SimFast21 to employ the criterion specified in Equation (2.5) in order to determine whether a given region is ionised. This requires computing the local ionisation photon rate R_ion (eq. 2.2) and local recombination rate R_rec (eq. 2.4) in each cell, as well as assuming an escape fraction f_esc that we constrain in the next section. Ionised cells are set to have a residual neutral fraction (eq. 2.6). Finally, the density field for computing R_rec and ionisation fields are smoothed using a CIC approach. This completes the SimFast21 modifications that we outlined in §2.2.1, and we will investigate how these changes impact the evolution of reionisation and the 21-cm power spectrum in §2.5.

2.4   Results for Observables

2.4.1   Constraints on the photon escape fraction f_{esc}

Our key free parameter is the escape fraction f_{esc} of ionising photons from galaxies. f_{esc} is essentially set by the amount of recombinations in the ISM that destroy ionising photons, along with dust extinction (Kaurov & Gnedin, 2015). Past large-scale models of the EoR typically constrain f_{esc} using observations, particularly the Thomson optical depth τ from the CMB measurements and Lyα observations (Fan et al., 2006). Up until recently, most of these models required high f_{esc} values to match the observations. As an example, the **6/256-RT** simulation requires an f_{esc} that reaches close to unity at high redshifts and small halo masses. However, the new τ values from Planck (2015) have eased such constraints, so for instance the semi-analytic model of Mitra et al. (2015) finds that they can match observations with $f_{esc} \lesssim 20\%$ throughout the EoR.

An alternative approach to constraining f_{esc} is to use extremely high-resolution hydrodynamic simulations to directly predict the escape of ionising photons from the ISM of primeval galaxies. Early simulations by Gnedin et al. (2008) predicted $f_{esc} \sim 1 - 3\%$. First galaxy simulations by Wise et al. (2014) predicted that f_{esc} drops from 50% to 5% over halo masses from $10^7 - 10^{8.5} M_\odot$. Ma et al. (2015) used cosmological zoom simulations of more sizable halos to estimate $f_{esc} \sim 0.001 - 0.02$ with an average $f_{esc} < 5\%$, with no strong dependance on galaxy mass or redshift. Overall, it appears that direct predictions of f_{esc} tend to favor modest values of the order of a few to ten percent in hydrogen cooling halos. While such f_{esc} values were difficult to reconcile with previous measurements of τ, Robertson et al. (2015) noted that the new Planck (2015) τ alleviates these tensions.

Here we tune our f_{esc} to match a suite of EoR observations. In particular, we will constrain to observations of the Thomson optical depth (τ) to the surface of last scattering from Planck (2015), ionizing emissivity density measurements by Becker & Bolton (2013), and the volume-averaged neutral fraction by Becker et al. (2015); Fan et al. (2006). The measure of τ primarily constrains the epoch of onset of reionisation, while the latter two observations primarily constrain the ionising photon budget at the end of the EoR or shortly after. Hence matching all three data sets simultaneously is a significant challenge for models (e.g. see

Finlator et al., 2011, 2015; Kuhlen & Faucher-Giguére, 2012; Mitra et al., 2011, 2012, 2013).

We begin by assuming a constant f_{esc} independent of halo mass or redshift. It is important to note that for our SimFast21 runs, this can be regarded as the mean escape fraction from all ionising sources within $0.375h^{-1}$Mpc cells which will typically contain a large number of star forming galaxies; we cannot constrain how f_{esc} varies for individual galaxies within each cell. Finlator et al. (2015) found that, to match the previous WMAP optical depth while still finishing reionisation by $z \sim 6$ required having a strongly mass- and redshift-dependent f_{esc}. However, the larger SimFast21 volume and the more recent Planck τ measurement alters such requirements.

We perform a SimFast21 run in a 300 Mpc (comoving) volume with 560^3 cells, using our modified version including the R_{ion} and R_{rec}. We then vary the f_{esc} value in order to match $\tau = 0.066$ from Planck. We are able to match this with $f_{esc} = 0.04$. For comparison, changing $f_{esc} = 0.11$ results in a predicted $\tau = 0.083$ which is the 1σ upper limit from *Planck,* while $f_{esc} = 0.02$ results in a predicted $\tau = 0.054$ which is their 1σ lower limit. Hence from this data alone, we constrain $f_{esc} = 4^{+7}_{-2}\%$. It worthwhile to mention that this is not a direct constraint on f_{esc} and ideally one may estimate the f_{esc} using a Bayesian inference or Markov chain Monte Carlo (MCMC) techniques to explore the parameters spaces more efficiently. We present our MCMC analysis in §3.5

We now examine the predicted ionising emissivity, which is the average rate of ionizing photons emission per unit volume, as measured from the Lyα forest at redshifts just after reionisation. To compute this, we extend our SimFast21 simulation to lower-z, and we sum the total ionising photon rate R_{ion} in all cells at a given redshift and divide by the simulation volume.

Figure 2.3 shows the predicted values from our simulations as the red, green, and blue dots for $f_{esc} = 0.11, 0.04, 0.02$, respectively. The observational range from Becker & Bolton (2013) is shown as the cyan region. It is clear that 4% provides a good fit to the observations, particularly at $z \approx 5$ where our simulations are most valid. We note that this low value of our $f_{esc} = 0.04$ has been previously found using a semi-analytic model by Kulkarni et al. (2013). Coincidentally, the f_{esc} values to match the upper and lower limits of Planck are comparable to that required to match the upper and lower limits of the ionising emissivity measures,
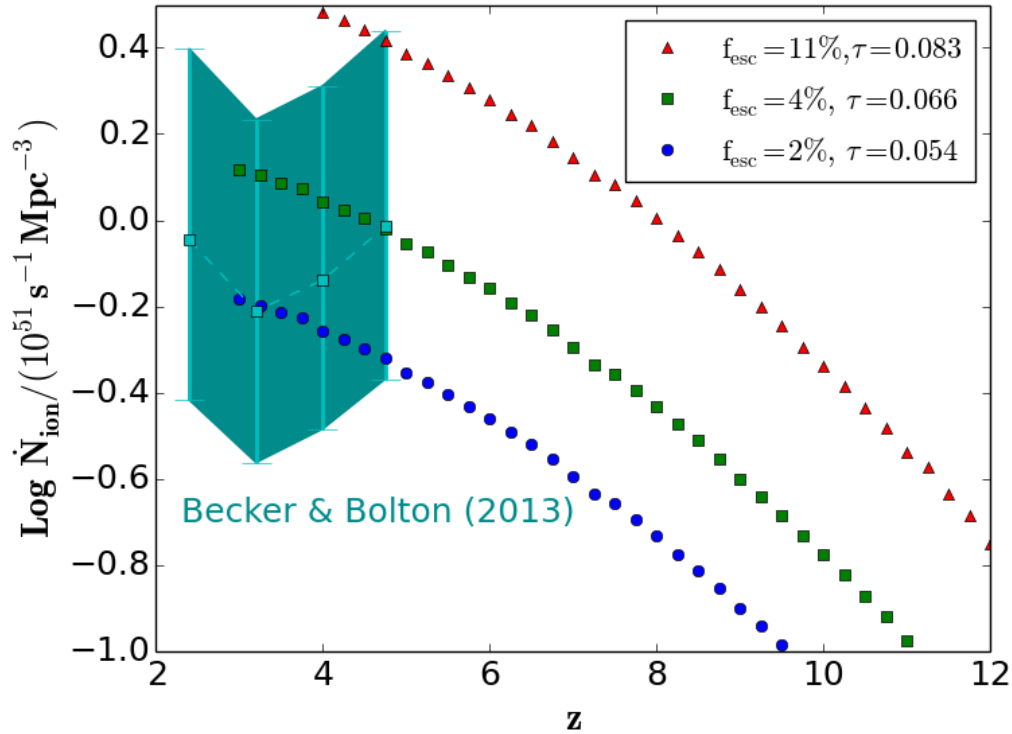
FIGURE 2.3: The predicted evolution of the ionizing emissivity density from our fiducial model using the R_{ion} parametrization, Equation(2.2). The blue circles, green squares and red triangles represent the ionizing emissivity density of the **Full** model using $f_{\mathrm{esc}} = 2\%$, 4%, and 11% respectively. The darkcyan shaded area comes from Becker & Bolton (2013). It is clearly shown that the three chosen values of f_{esc} matches the actual, upper and lower limits of the ionizing emissivity by Becker & Bolton (2013) as well as the corresponding recent bounds on the reionisation optical depth τ by Planck (2015).

showing that these data sets currently provide comparable constraints on f_{esc} for our simulations.

As a final test, we examine the evolution of the cosmic volume-weighted neutral fraction, as can be probed observationally using the opacity of the Lyα forest (e.g. Fan et al., 2006). This is shown in Figure 2.4. Focus for now on the solid blue line labeled "**Full**", which is the model we are considering here with $f_{\mathrm{esc}} = 0.04$. In this simulation, the Universe reionises at $z \sim 7$. This may be slightly higher than that inferred from observations by Fan et al. (2006), but there is some uncertainty on this owing to the large sightline-to-sightline variation in the mean Lyα opacity (Becker et al., 2015). Hence we find that a 4% escape fraction is also broadly consistent with observations of the completion of reionisation.

For a more pictorial view, the evolution of the neutral fraction in our fiducial simulation with $f_{\mathrm{esc}} = 0.04$ is depicted in Figure 2.5. This shows a one-cell-thick
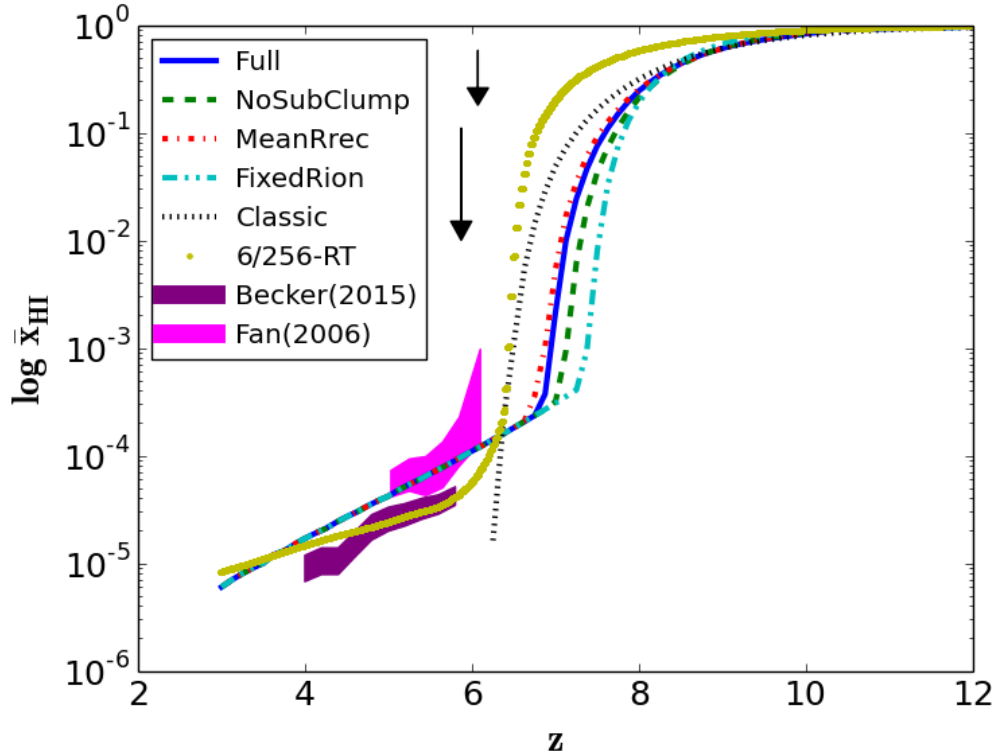
FIGURE 2.4: The volume-weighted average neutral fraction, $\bar{x}_{\mathrm{HI}}$, of our models compared to 6/256-RT (Finlator et al., 2015) and observations. Solid blue represents our fiducial model, **Full**. The **NoSubClump** (Dashed, Green), **MeanRrec** (Dash-dotted, Red), **FixedRion** (Dash-dot dotted, Cyan), **Classic** (Dotted, Black) and **6/256-RT** (Dots, Yellow) are also shown. The shaded magenta and purple show Fan et al. (2006) and Becker et al. (2015) measurements respectively. Vertical arrows represents the recent upper limit constraints by McGreer et al. (2015) at z=6 using Lyα and Lyβ forests. It is quite clear that adding the residual neutral f_{resid} (eq. (2.6)) to our fiducial simulations is crucial to match the observation, as opposed to the **Classic** model.

$(0.375 h^{-1}\mathrm{Mpc})$ map of the neutral fraction x_{HI} (Figure 2.5) constructed by splicing together the outputs at different redshifts into a continuous series. Reionisation begins at z $\sim$ 17 and the Universe is reionised by $z \sim 7$. In our model, the EoR is an extended process since the neutral fraction x_{HI} drops slightly from 0.99 to 0.92 as $z \sim 17 \rightarrow 11$. It is seen that the ionised gas forms bubbles of increasing size, corresponding to a classic inside-out topology where the densest regions are ionised first[8]. While illustrative, for actually computing the 21-cm power spectrum we will not use the light cone in Figure 2.5 but rather individual snapshots at various redshifts, since it has been shown by La Plante et al. (2014) that the

---

[8]We note that SIMFAST21 essentially assumes such a topology, since it calculates the ionisation state within bubbles, and assumes that all the gas within a bubble is fully ionised; it is not possible to get neutral patches within such bubbles that would correspond to outside-in reionisation.
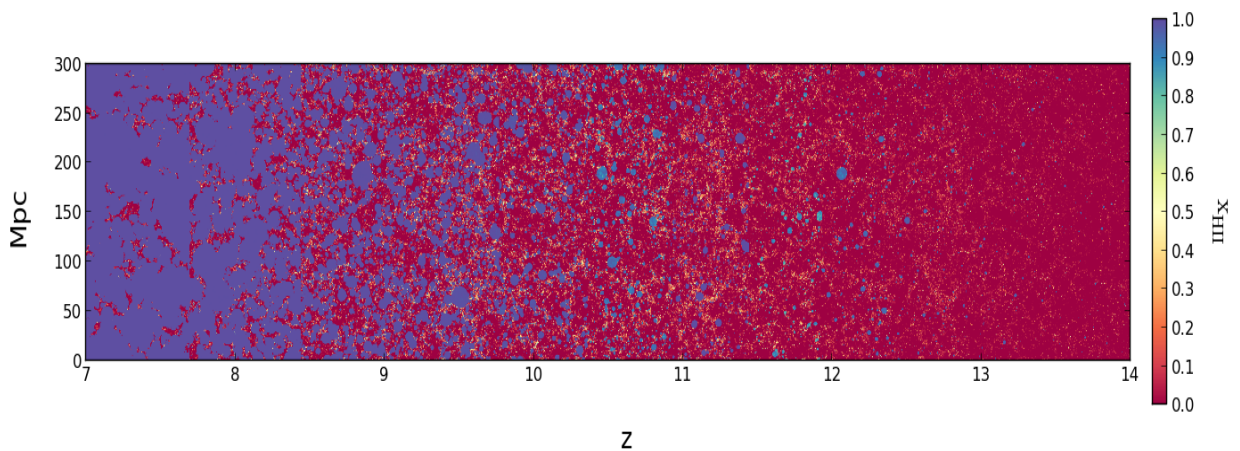
FIGURE 2.5: Evolving map of the neutral fraction in our 300 Mpc, 560^3 cell SIM-FAST21 simulation with a 4% escape fraction.

light cone effect are small for our box size. The goal of the redshifted 21-cm EoR observations is to constrain this bubble size distribution and its evolution through measurements of the power spectrum, thereby providing constraints on the topology and sources of reionisation.

As noted earlier in Figure 2.1, it appears that the global ionisation rate, and by proxy the star formation rate, at a given halo mass in our hydrodynamical simulations may be high by a factor of $1.5 \times$ compared to observations. To investigate this in more detail, we show in Figure 2.6 the star formation rate function from our SIMFAST21 using R_{ion} (blue, dotted-line), compared to observations by Smit et al. (2012) at $z = 7$. Indeed, we see that our simulated SFRs are generally higher by this factor across all galaxies.

Given that this discrepancy is mostly invariant with star formation rate, for the purposes of EoR modeling it can be directly translated into a correction factor on the escape fraction. In other words, if we corrected our R_{ion} values down by a factor of 1.5 (normalized R_{ion}) to account for the mismatch in SFRs (green solied line in Figure 2.6), we could raise our f_{esc} values by a factor of 1.5 and obtain the exact same results for the 21 cm power spectrum (see Figure 2.13); there is no impact on the predicted power spectrum of 21-cm fluctuations for a model whose f_{esc} is tuned to match observations of the history of reionization.

Hence if we take the observations of Smit et al. (2012) at face value, we require an escape fraction of $6^{+10.5}_{-3}\%$ to match the various EoR observations described above. This would alleviate some of the discrepancy between our value and that inferred
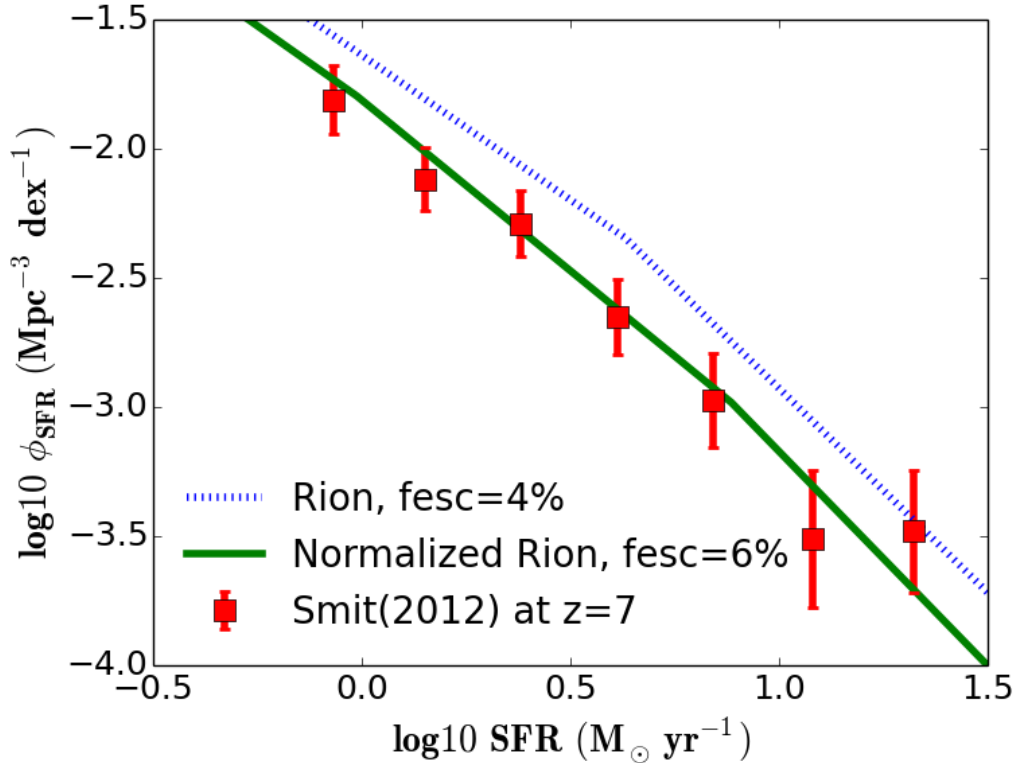
FIGURE 2.6: Comparison of the SFR functions from our SimFast21 using R_{ion} (blue, dotted-line) with the stepwise SFR functions of Smit et al. (2012) which were derived from the dust-corrected UV Luminosity functions. The SFR at a given halo mass from SimFast21, using R_{ion} from hydrodynamic simulations (**6/256-RT, 32/512**), is higher by a factor of $\times 1.5$ than implied by observations. The green sloid line shows the SRF function from SimFast21 using the normalized R_{ion} that matches Smit et al. (2012).

by Robertson et al. (2015), who argued for $f_{\text{esc}} = 20\%$ from observations. At the same time, it is not in conflict with direct observational constraints on f_{esc}, which tend to prefer values of less than 10%.

To summarize, our simulation with the new version of SimFast21 yields the somewhat remarkable result that a constant escape fraction of 4%, independent of mass or redshift, is sufficient to match observational constraints on both the onset and end of reionisation. This value may be increased to 6% when we fine-tune our model to match observed star formation rate measurements of Smit et al. (2012) using the normalized R_{ion}. Robertson et al. (2015) also argued for a relatively modest escape fraction ($f_{\text{esc}} = 20\%$) based on the new Planck τ, which is somewhat higher than our preferred value. In contrast, previous works such as Finlator et al. (2015) have argued for a substantially varying, and generally much higher, f_{esc}. Even if we constrain to the WMAP $\tau = 0.078$, we still require an

escape fraction of only $\approx 20\%$, still much lower than Finlator et al. (2015); hence it is not only just the new value of τ that is driving our lower f_{esc}. Additionally, the key aspect is the large volume of the SimFast21 simulation that includes more massive halos relative to small-volume, full-RT simulations. We will show in §2.5.4 that, in our new SimFast21 model, these moderate-mass halos are an important contributor to the photon budget, because the ionising photon rate scales super-linearly with halo mass (eq. 2.2). This highlights the importance of running large-volume simulations, tuned to available observations, to properly characterise the escape fractions that are required to complete reionisation.

2.4.2 The 21 cm power spectrum

Using our well-constrained SimFast21 simulation for the evolution of the ionisation field, we now make predictions for our key observable, namely the redshifted 21-cm power spectrum.

Under the assumption that the spin temperature is much higher than the CMB temperature, we compute the 21-cm brightness temperature as follows:

$$\delta T_b(\nu) = 23 \mathrm{x_{HI}} \Delta \left(\frac{\Omega_b h^2}{0.02} \right) \sqrt{\frac{1+z}{10} \frac{0.15}{\Omega_m h^2}} \left(\frac{H}{H + dv/dr} \right) \mathrm{mK}, \qquad (2.9)$$

where dv/dr is the comoving gradient of the line of sight component of the co-moving velocity. Using Equation (3.6), we define the 21-cm power spectrum as follows: $\Delta^2_{21} \equiv \mathrm{k}^3/(2\pi^2\,\mathrm{V}) < |\delta \mathrm{T_b(k)}|^2_{\mathrm{k}} >$.

Figure 2.7 shows the 21cm power spectrum at z=7.25, 7.5, 7.75, 8, 9, 10, 12 from our 300 Mpc, 560^3-cell SimFast21 simulation. The evolution in Figure 2.7 qualitatively follows the pattern described in Lidz et al. (2008): At early times (z=12), the 21cm power spectrum traces the density power spectrum, because virtually all of the gas is neutral. During the interval $z = 12 \rightarrow 9$, the tendency for reionisation to begin in the largest overdensities offsets the tendency for such overdensities to host high concentrations of neutral gas. As soon as the most overdense regions are ionized, the density field of *neutral* hydrogen is overall much more homogeneous than prior to reionisation, suppressing large-scale power in 21cm fluctuations. At later epochs, the ionised regions become larger, leading to more large-scale power. In essence, this behavior is reflective of inside-out reionisation where the inhomogeneities are first prominent on smaller scales and
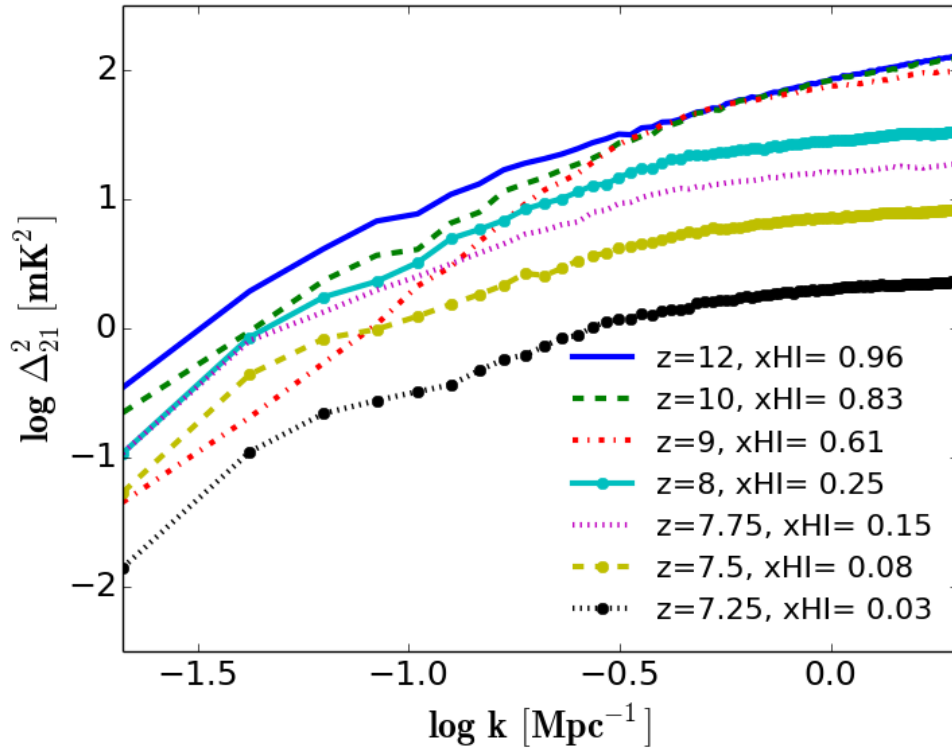
FIGURE 2.7: 21-cm power spectrum predicted at z=7.25, 7.5, 7.75, 8, 9, 10, 12 from our fiducial SIMFAST21 run. At early times (z=12), the 21-cm power spectrum traces the density field power spectrum. During $z = 12 \rightarrow 9$, the presence of more ionised hydrogen in large over-dense regions than under-dense regions suppresses the 21-cm power spectrum. At the intermediate phases, the rapid growth of ionised bubbles boosts the 21-cm power spectrum. At later epochs, when the EoR is nearly complete, the 21-cm power spectrum drops rapidly.

then move to larger scales. However, there is a difference in amplitude (~ 1 order magnitude) between our power spectra and those of Lidz et al. (2008), which might be due to differences in the density field, particularly at the intermediate and final stages of reionization.

As emphasized by Sobacchi & Mesinger (2014), a spatially-inhomogeneous recombination rate suppresses fluctuations on scales larger than ~ 0.1 Mpc^{-1} (this effect is also visible in Figure 1 of Lidz et al. (2008), although they did not emphasise it). The major advance in our work with respect to Lidz et al. (2008) and Sobacchi & Mesinger (2014) and others is a demonstration that including a superlinear dependence of ionising efficiency on halo mass amplifies large-scale fluctuations, partially restoring the flatness of the 21cm power spectrum; we will return to this point in our discussion of Figure 2.13.

Figure 2.7 represents our predictions for the evolution of the 21-cm power spectrum from the EoR. In the next chapter, we will examine the detectability of Δ_{21}^2 for ongoing and upcoming 21-cm EoR experiments. For this work, we focus on studying how Δ_{21}^2 is impacted by the physical modeling variations that we have implemented into SIMFAST21.

2.4.3 Numerical convergence

Our chosen simulation volume is generally limited by our computational capabilities, together with the requirement that our cell size match the chosen cell size over which we have computed our recombination rate in the **16/256-RT** simulation. Here we check whether our results are robust to our choice of volume by running simulations with smaller volumes (keeping the cell size fixed). This will also allow us to empirically determine the largest robustly predicted scale in our simulation for a given box size.

Figure 2.8 shows the 21-cm power spectrum $\Delta_{21cm}(k)$ calculated from boxes with length 150 Mpc (green, dashed) and 75 Mpc (red, dot-solid), along with our fiducial 300 Mpc box (blue solid). These show $\Delta_{21cm}(k)$ over scales from twice the cell size up to the full box size. The corresponding physical scale $2\pi/k$ is shown along the top axis. Three panels show $z = 9.5, 8.75, 8$ which correspond to global neutral fractions of roughly three-quarters, one-half, and one-quarter, respectively. Generally, the numerical convergence with box size is very good, particularly during the early phases of reionisation. At $z = 8$, some deviations are seen at the large scales (small k), which start at about one-quarter of the box size or larger, but they are typically less than a factor of 2 in the power. We conclude that our simulations can robustly predict the 21-cm power spectrum over the range of scales from a few times the cell size up to one-quarter of the box size, over the redshift range where there is a significant global neutral fraction and hence 21-cm signal.
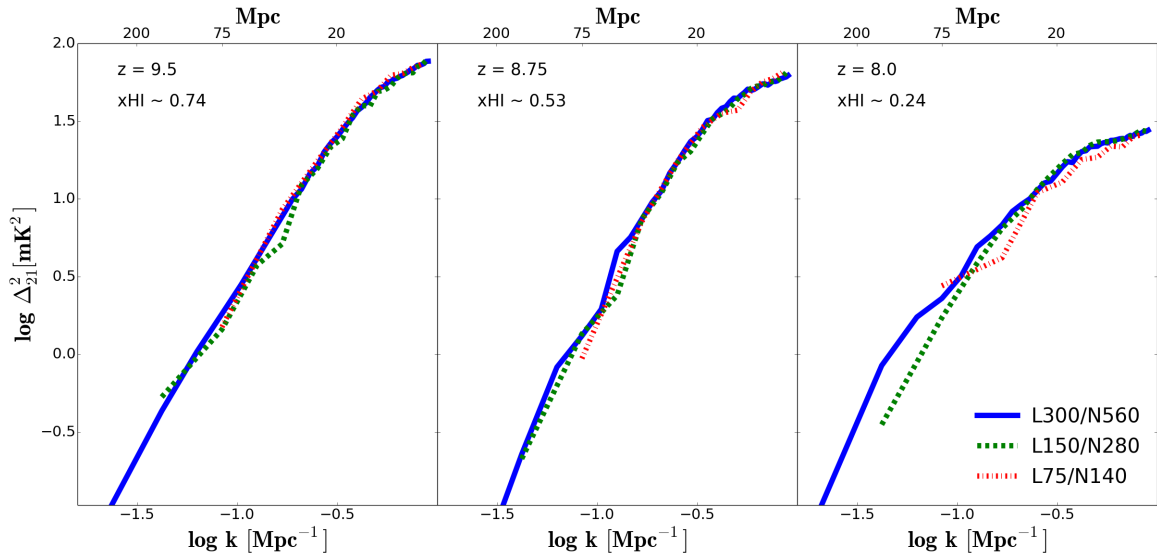
FIGURE 2.8: Volume convergence of the 21-cm power spectrum for SimFast21 runs with a box size of 300 Mpc (blue, solid), 150 Mpc (green, dashed), and 75 Mpc (red, dashed-dotted). The convergence at all redshifts is excellent up to about one-quarter of the box size.

2.5 Impact of varying ionisations and recombination assumptions

Our main improvement from the previous version of SimFast21 is a more physically-motivated characterisation for the ionising source population and small-scale recombinations. Here we quantitatively investigate the impact of these new parameterizations for $R_{\rm ion}$ and $R_{\rm rec}$ on the reionisation history and morphology, in comparison with previous assumptions. We do so by essentially reverting our new code back towards the original code one piece of physics at a time, so that we can isolate the impact of each new physical component.

To do this, we run five simulations with a box size L= 300 Mpc and N= 560^3 on a side using the same density field and halo catalogs (i.e. the same cosmology), only with different astrophysical assumptions for $R_{\rm ion}$ and $R_{\rm rec}$. Because this changes the evolution of the ionisation field, in order to make the comparison more uniform, we re-tune the photon escape fraction $f_{\rm esc}$, or in the case of the original SimFast21 the efficiency parameter ζ, in order to achieve the Planck $\tau = 0.066 \pm 0.016$. By doing so, we can compare these models at the same redshift and neutral fraction more meaningfully.

The five simulations are as follows:

- **Full:** This is our fiducial model in which we use our new parameterizations R_{ion} and R_{rec} in Equation (2.5) to identify the ionised regions, assuming $f_{\text{esc}} = 4\%$.

- **NoSubClump:** Similar to **Full**, but using inhomogeneous recombinations computed from local cell's densities $(=\alpha_a n_{\text{H}}^2)$ with no contribution from sub-grid clumping, we re-tune to obtain $f_{\text{esc}} = 2.5\%$.

- **MeanRrec:** Similar to **Full**, but using a spatially-homogeneous recombination rate computed from the mean hydrogen cosmological density at each z; $f_{\text{esc}} = 1.5\%$.

- **FixedRion:** Similar to **Full**, only using Fixed Rion per halo mass $= 9 \times 10^{49} \text{sec}^{-1}$ which corresponds to the value for $M_{\text{h}} = 10^8 M_\odot$ and assuming $f_{\text{esc}} = 100\%$.

- **Classic:** This run with the original SimFast21 using Equation(2.1) to identify the ionised regions with $\zeta = 11$.

Our **Full** model is what we have used to make the predictions presented so far. The **NoSubClump** and **MeanRrec** simulations do not use the R_{rec} taken from our **16/256-RT** box, but rather compute recombinations locally on a cell-by-cell basis, and globally using the cosmic mean density, respectively. Variations among these three runs can thus be used to isolate the scale at which recombinations are important. The **FixedRion** simulation is analogous to using a constant efficiency parameter, but still uses our **Full** recombination model; hence comparing to the **Full** model can be used to assess the importance of employing a halo mass-dependent ionisation rate. The **Classic** case is the original SimFast21 code, which uses a constant efficiency parameter and no explicit recombinations.

We now focus on the variations among these models for the key observables that we have described before, and provide a physical interpretation for the differences that we see.

2.5.1   Global neutral fraction history

Figure 2.4 shows the volume-weighted neutral fraction ($\bar{x}_{\text{HI}}$) evolution produced by our five models, as labeled. We also show this evolution taken directly from the

6/256-RT simulation as the yellow dots. Observations by Fan et al. (2006) and Becker et al. (2015), with 1σ range, are indicated by the shaded regions. Vertical arrows represents the recent "model-independent" upper limits by McGreer et al. (2015) at $z = 6$ using the Lyα and Lyβ forests.

At high-z, the onset of reionisation is similar for all models, primarily because we have tuned them to match the *Planck* τ value which is most directly a constraint on the onset of reionisation. Comparing our **Full** simulation first to the **6/256-RT** simulation, we note that while the shape of $\bar{x}_{HI}(z)$ is similar, reionisation occurs earlier by $\Delta z \sim 0.5$. As mentioned before, this owes to the small dynamic range of **6/256-RT** that fails to capture: (i) the very earliest stages driven by the rarest over densities corresponding to the longest-wavelength fluctuations. (ii) the larger halos that are important particularly during the later stages of the EoR.

Comparing the **Full** to **Classic** runs, it is seen that the **Classic** run reionises the Universe later, more like $z \sim 6.5$. Since this model has no explicit model for recombinations, the early ionisations are very effective, which reduces the amount of ionisations needed at early times in order to reproduce the *Planck* τ value. This results in less ionising photons overall, which delays reionisation. The strength of this effect is best quantified by comparing to the **FixedRion** run, which like the **Classic** case has a constant ionising photon efficiency per unit halo mass. Comparing these we can see that ignoring recombinations can shift the end of the EoR by $\Delta z \sim 1$.

The impact of recombinations is seen by comparing the **Full**, **NoSubClump**, and **MeanRrec** models. The differences in the ionisation history are relatively minor, with **NoSubClump** producing slightly earlier reionisation. In this comparison, **Full** and **MeanRrec** produce very similar global reionisation histories, but we will later see they differ significantly in terms of topology.

Overall, changing the nature of the ionisation sources has a larger impact, at fixed τ, than varying the recombination methodology. Nonetheless, constraining to match τ results in models having an end of reionisation all within $\Delta z \sim 1$ of each other. Hence the global evolution of the neutral fraction is relatively insensitive to our modifications to SimFast21, with the largest difference being relative to a model with no recombinations (**Classic**) or a small-volume hydrodynamic simulation that does not yield large galaxies (**6/256-RT**).

2.5.2   Ionizations Maps

We now explore how the topology of reionisation varies amongst our five different physical models. This is relevant to the 21-cm power spectrum since it focuses on topological features such as the distribution of ionised bubble sizes that directly reflects in the power spectrum. Furthermore, forthcoming observations with the SKA can in principle directly map the neutral gas distribution. To get a flavour for the sorts of topology variations introduced by varying our input physics, we begin by examining maps of the ionisation field evolution.

Figure 2.9 shows maps of the ionisation field for the five models across different phases of the EoR at $z = 9.5, 8.75, 8.0$ (top to bottom). Overall, the Universe becomes more ionised at later epochs, and the global neutral fractions are generally similar at the same z. Nonetheless, there are clear differences in the topology of the ionised regions amongst the various models. The **Full** and **NoSubClump** models display quite similar morphologies across all EoR phases as seen in their ionisations maps (first two columns). This implies that including the sub-grid clumping effects through $R_{\rm rec}$ does not strongly affect the EoR topology, and suggests that computing recombinations using only the local cell's densities (as in **NoSubClump**) is sufficient to properly model the EoR. This is tantamount to saying that the local clumping factor within each cell is close to unity, and the main variations in the clumping factor occur on scales larger than our cell size; indeed, we have checked that this is the case within the **6/256-RT** run. While this suggests that including $R_{\rm rec}$ was perhaps superfluous, this outcome was not obvious from the outset. This perhaps conflicts with the conclusions of Raičević & Theuns (2011); their Figure 2 suggests that the local clumping fluctuations are quite important. We then expect that the **Full** and **NoSubClump** models will accordingly produce the same ionisation and 21-cm power spectra.

The **MeanRrec** ionisation maps show relatively larger ionised bubbles (third column) than in our fiducial model. Hence ignoring the density fluctuations and clumping on large scales and assuming recombinations based on the cosmic mean density is a poor approximation. This occurs because the **MeanRrec** model has fewer recombinations, because the recombinations primarily occur in the dense regions, and the recombination rate scales roughly as the square of the density. Therefore, the ionising photons can propagate farther and create larger bubbles.
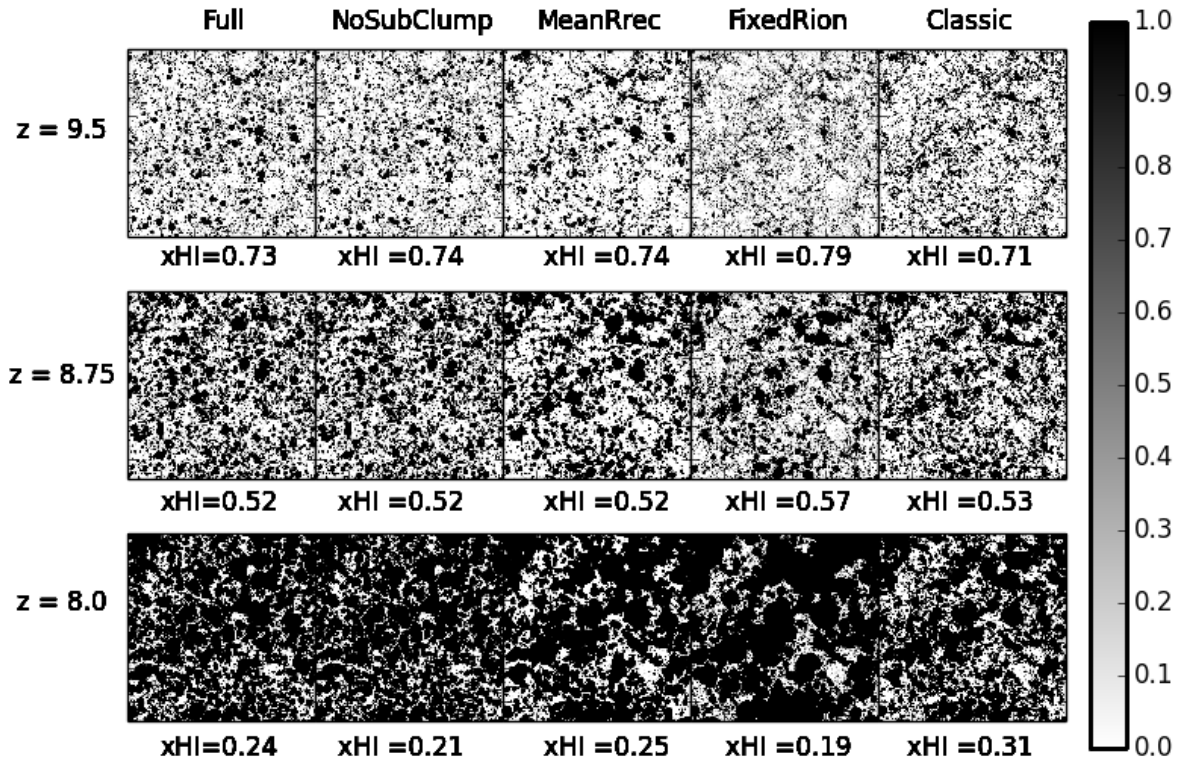
FIGURE 2.9: The ionisation maps of the five models at z=9.5 (top-row), z=8.75 (middle-row) and z=8.0 (bottom-row). White regions are neutral whereas black regions are ionized. It is clear that the **Full** and **NoSubClump** models display similar morphologies across all EoR phases, suggesting that the local sub-clumping effects (≤ 0.5Mpc) have no significant contribution to the EoR on large scales (≥ 100Mpc). The **FixedRion**, **MeanRrec** and **Classic** models display similar morphologies only with different bubble sizes due to the variation in the physical assumptions.

At early stages of the EoR (at z=9.5), the **FixedRion** model (fourth column) produces smaller ionised bubbles than other models. This occurs because of the interplay of recombinations and the ionising source locations. Given that our reionisation topology is generally inside-out (dense regions ionising first), this means that the dense regions with the largest halos live in regions that are most rapidly recombining. In the **Full** model, the increasing strength of ionising photon output with halo mass helps to offset these rapid recombinations, and power ionising fronts out of the dense regions. However, in the **FixedRion** model the large halos have lower ionising output, and hence the resultant bubbles grow less before stalling. Conversely, in low-density regions with smaller halos, **FixedRion** will produce larger bubbles. Hence overall, the bubble size distribution is more uniform

in this case, which will be evident in the power spectra we consider below.

It is interesting to note that the **MeanRrec** and **FixedRion** models share similar morphologies at the intermediate phase of the EoR ($z = 8.75$), which implies that inhomogeneous R_{rec} has roughly a similar level of an effect as including mass-dependent ionisation. Given that we have constrained all models to match the *Planck* optical depth, a "crossover" at $x_{\text{HI}} \sim 0.5$ is perhaps not surprising.

Finally, the **Classic** (fifth column) displays a morphology that is between **FixedRion** and **MeanRrec** morphologies. Its form of ionisation is most similar to **FixedRion**, but it includes recombinations implicitly through the constrained efficiency parameter ζ (eq. 2.1) as a direct suppression of the number of ionising photons output in each cell. Effectively, this cell-based suppression ends up being stronger than the recombinations in **MeanRrec** and weaker than that in **FixedRion**, which sets the **Classic** morphology between those of **MeanRrec** and **FixedRion**

These results show that assumptions regarding the ionisation and recombination rates in large-scale models can have a significant effect on the topology of reionisation and its evolution.

2.5.3 Ionized mass fraction as a function of density

We now quantify the topology shown in the maps in the previous section. The approach we use here is to consider the ionised mass fraction as a function of local overdensity, to better understand how our physical assumptions are impacting the ionisation state of the gas in various environments.

Figure 2.10 shows the mass-weighted global ionised fraction $\bar{x}_{\text{m}}$ as a function of density Δ_{bin} of our five models at three different redshifts $z = 9.5, 8.75, 8.0$ (left to right), when the neutral fraction is approximately $0.75, 0.5$, and 0.25, with some variations between the models (the values quoted on the figure are the average x_{HI} of all models at each z).

In all models and at all times, the over-dense regions ($\log \Delta_{\text{bin}} > 0.0$), where the halos and hence the photon sources are more numerous, are more ionised while low-density regions such as voids ($\log \Delta_{\text{bin}} < 0.0$) take longer to become ionised. This is due to the gradual progress of the ionisations fronts through the surrounding regions regions into low density regions (Iliev et al., 2006), and the relatively low
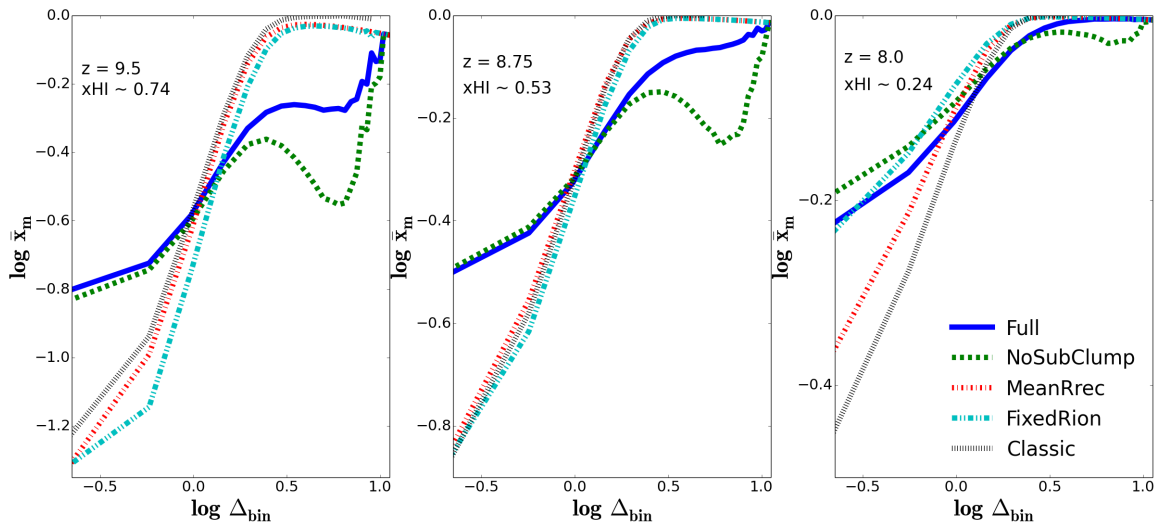
FIGURE 2.10: The mass-weighted ionized fraction $\log \bar{x}_m$ evolution of the five models for given overdensity bin $\log \Delta_{\text{bin}}$. LEFT: Early EoR phase, MIDDLE: Intermediate EoR phase and Right: Final EoR phase. The over-dense regions ionize first while the under-dense regions take longer to become ionised, which shows that the EoR proceeds in an inside-out fashion.

clumping factor (Finlator et al., 2013) and recombination rate particularly in the late EoR, which results in these high-density regions remaining ionised. Hence in all these runs, as we saw in the **Full** case earlier (Figure 2.5), reionisation proceeds in an inside-out fashion.

We first compare **Full** (solid blue) with **NoSubClump** (dashed green). In the moderate and low-density regions, these models are essentially identical, except at late times when the ionised fraction in **NoSubClump** is slightly higher (likely an artifact of tuning to the same τ value). Sub-cell gas clumping thus only has an effect in relatively more overdense regions, which physically makes sense since such clumping occurs on small scales. The impact of sub-cell clumping is maximized at overdensities $\Delta_{\text{bin}} \sim 5 - 10$, whereas in the most dense regions the ionisations overwhelm recombinations regardless of the clumping. However, the trend is opposite to one might naively expect: The **NoSubClump** model actually has a lower ionisation fraction, indicating more recombinations, than the **Full** model. This happens because the **NoSubClump** model computes the reionisation rate assuming a fully ionised cell at the cell's density, but the R_{rec} fitting formula used in **Full** includes the effect that dense regions have more neutral gas, and hence the recombination rate is lowered compared to the fully ionised case.

Comparing **MeanRrec** to **Full**, we see much more dramatic differences than compared to **NoSubClump**. As we have seen from the maps earlier, assuming recombinations only at the mean cosmic density produces quite a different topology. The ionised fraction is significantly higher in the high-density regions, and lower in the low-density regions, with a crossover around the mean density ($\Delta = 1$). Since recombinations scale as the square of the density, dense regions have lower recombination rates in **MeanRec** leading to more ionised gas, and conversely low-density regions have higher recombination rates leading to less ionised gas.

The **MeanRrec**, **FixedRion** and **Classic** have roughly the comparable behaviour of $\bar{x}_m$ during the early phases of the EoR. This also was clear in their topologies (Figure 2.9). Once these models are constrained to have matching τ values which governs their early EoR evolution, using a mean density recombination rate with inhomogeneous sources turns out to be roughly equivalent in topology to using a fixed ionising output per unit mass and inhomogeneous recombinations. The **Classic** model falls in between these two extremes, with fixed ionising efficiency and the recombinations implicitly tied to the ionisations. At lower redshifts, the three models start to diverge at low densities, as the higher recombination rates at $\log \Delta < 0$ in the **MeanRec** model lead to lower ionised fractions than in the **FixedRion** model. The **Classic** model is still lower, since the recombinations are tied to ionisations which are very low in the low-density regime. Interestingly, in this regime the **FixedRion** model becomes similar to the **Full** case.

Overall, our results show that including both inhomogeneous recombinations and ionisations is important to produce the correct topology evolution of the EoR. While neglecting sub-cell recombinations has little impact, assuming either recombinations that are based on the mean density or tied to the ionisation rate results in dramatically different ionised gas topologies. Likewise, using a fixed ionising photon output per unit halo mass results in a substantially different topology during the neutral-dominated phase of the EoR, though it becomes more similar to the fiducial case at later stages.

2.5.4   Ionizing photon output versus halo masses

An interesting quantity for observing the EoR is the mass scale of galaxies providing the bulk of the ionising photons. This is important for future observational
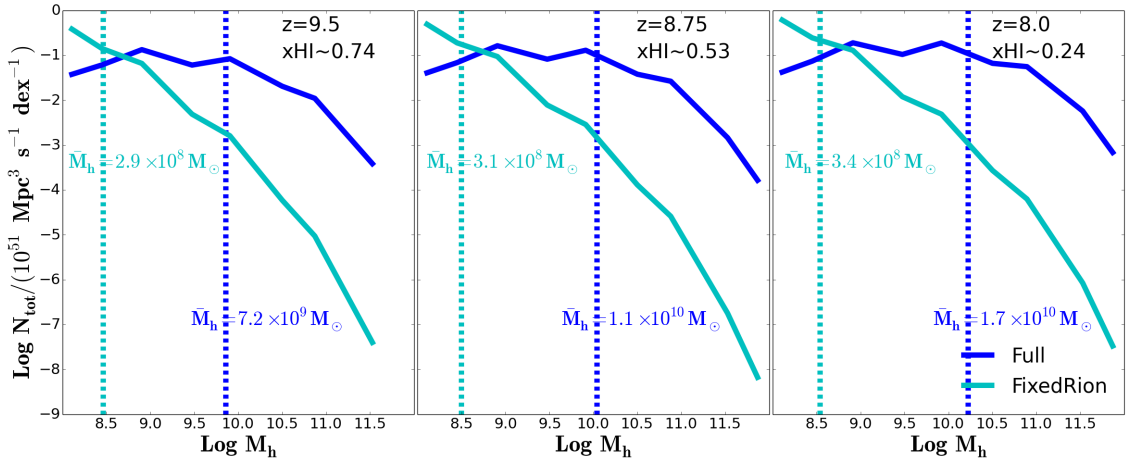
FIGURE 2.11: Total ionizing emissivity (N_{tot}) of our fiducial model (blue, solid) and the **FixedRion** (cyan, solid) for halo mass bin size of 0.5. Vertical dashed lines represent the ionisation-weighted halo mass ($\bar{M}_h$) of the **Full** (blue) and **FixedRion** (cyan) models. It is evident that the dominant halo mass during EoR is much larger in our fiducial model than in the **FixedRion** model by about 1-2 order of magnitude.

programs with for instance the *James Webb Space Telescope*, which aims to directly detect these galaxies. Given that we track the ionising output of halos, we can straightforwardly determine the ionising photon distribution as a function of halo mass, and assess the impact of our new input physics on this. We consider only on our fiducial (**Full**) and **FixedRion** models, to compare the total amount of emitted ionising photons per halo mass in each model at fixed τ, since we are not concerned with recombinations here. Figure 2.11 shows histograms of the total ionising emissivity N_{tot} for halo mass bins of the **Full** (blue) and **FixedRion** (cyan) at $z = 9.5, 8.75, 8$ (from left to right). The **FixedRion** model, with an assumed constant escape fraction and constant ionising output per unit halo mass, results in a steeply declining ionising emissivity with M_h that mimics the steep halo mass function. In contrast, the **Full** model has greater ionising output per M_h for more massive halos, shifting the distribution towards higher halo mass.

The vertical dashed lines (blue:**Full**, cyan:**FixedRion**) in Figure 2.11 represent the ionisation-weighted halo mass $\bar{M}_h$ of all halos at the corresponding redshifts (z=9.5,8.75,8.0). $\bar{M}_h$ thus represents the halo mass limit above (or below) which 50% of the total ionizing photons is being emitted. We see that the $\bar{M}_h$ is $\sim 10^{10} M_\odot$ in our fiducial model whereas it is $\sim 10^{8.5} M_\odot$ in **FixedRion**, with only a mild dependence on redshift.

Hence a model assuming a fixed ionising output per unit halo mass would predict

that reionisation is dominated by extremely small galaxies near the hydrogen cooling limit, while a more realistic model for ionising photon output suggests that moderate-mass halos are responsible for reionisation. The latter scenario bodes well for future direct observations of galaxies driving reionisation, since galaxies in $\sim 10^{10} M_\odot$ halos are likely to be detectable with *Webb*.

2.5.5   Ionizations and 21-cm power spectra

We now examine how these physical variations impact the ionisation and 21-cm power spectra. The 21-cm power spectrum is the key observable that will be obtained in the forthcoming 21-cm EoR observations. We compute the ionisation power spectrum as $\Delta_{xx}^2 \equiv k^3/|(2\pi^2\,V) < |x_{HII}|^2 > /x_{HI}^2$, analogous to the 21-cm power spectrum that was introduced in §2.4.2.

In Figure 2.12 and 2.13, we compare the ionization fields and 21-cm power spectra of our fiducial model (**Full**) to other models at different phases of the EoR, respectively. We begin by comparing the 21-cm power spectra from our fiducial model (**Full**) using the actual R_{ion} (blue, solid), that requires $f_{esc} = 4\%$ to match the observations excluding SFR function measurements, with the renormalized R_{ion} (orange, solid) that requires $f_{esc} = 6\%$ to match the SFR functions measurements. We see, as expected, that the 21-cm power spectra with and without the renormalization to R_{ion} are identical, which confirms that the normalization of R_{ion} can be directly compensated by tuning our free parameter f_{esc} to higher or lower values as implied by observations.

As with the topology, the **Full** and **NoSubClump** models produce approximately similar power spectra of the ionisation fields and 21-cm signal through all EoR phases. The differences in topology at moderate overdensities are sufficiently rare to not impact the overall power spectrum appreciably. This confirms that the sub-clumping effects have little significance to the EoR 21-cm observables.

To further test the effects of sub-grid clumping, we also ran the **NoSubClump** model with the same $f_{esc} = 4\%$ that is used in the **Full** model, without matching to the same τ. We confirmed that the **NoSubClump** model produces mostly identical results at the same neutral fraction for this slightly different f_{esc}. This confirms our finding, that the sub-clumping has no significant contribution to the EoR process, is robust and independent of the way we used to do this comparison
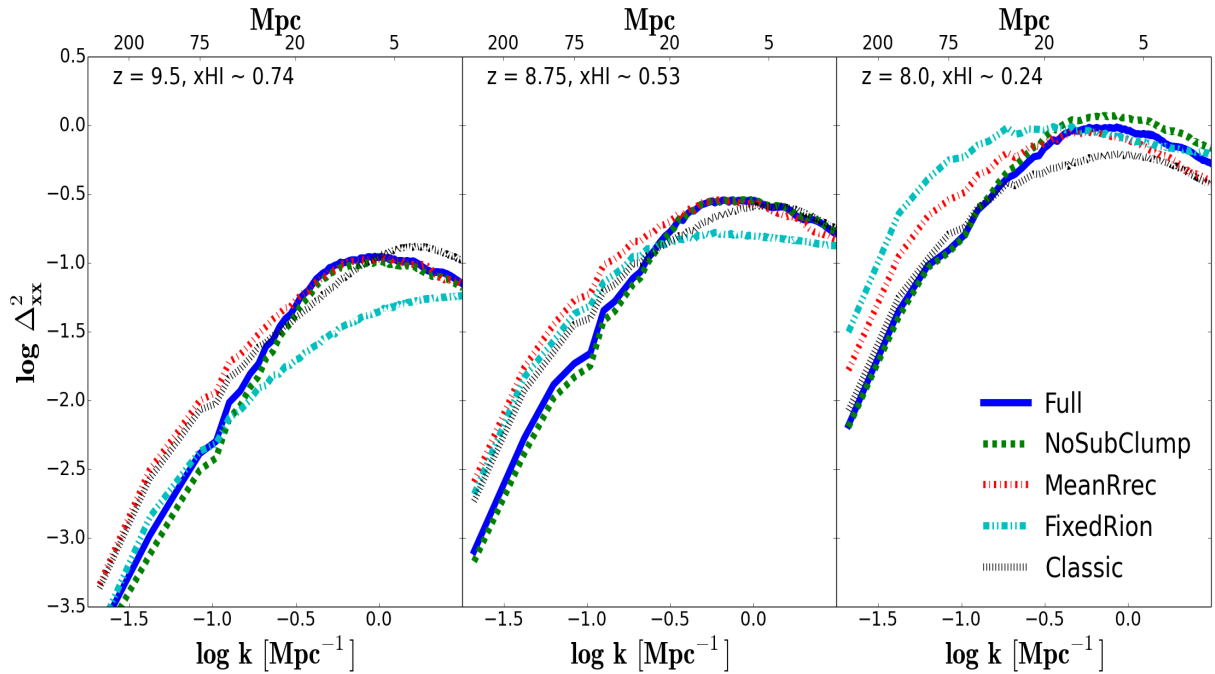
FIGURE 2.12: The power spectra of the ionisation fields of the five models at different stages during the EoR. Variations in physical assumptions can result in $\times 2 - 3$ variations in the ionisation power spectrum such as: $R_{\rm rec}$ suppresses the large-scale power spectrum while $R_{\rm ion}$ boosts the small-scale power spectrum.

with the **Full** model. As we have seen in studying the overall topology, the **Full** and **NoSubClump** models are very similar, while the **MeanRrec**, **FixedRion**, and **Classic** cases show similar evolutionary trends. Not fully accounting for both non-linear ionisations and inhomogeneous recombinations tends to raise the ionisation field power spectrum on large scales relative to smaller scales, which results in a lower 21-cm power spectrum by a factor of a few. Hence, for instance, compared to the old version of SimFast21 during the early stages of the EoR, our new code predicts almost $4\times$ as much power on large scales, and twice as much on small scales.

The shape of the power spectra continue to be different at later stages, at which time the **Full** model ends up with less large scale power but more small-scale power, as visually evident from the ionisation maps in Figure 2.9. The physical reasons were discussed in §2.5.2, but basically arise because properly accounting for recombinations tends to slow the ionisation fronts when compared to **MeanRrec**, while the **FixedRion** produces relatively more photons in low-density regions from low-mass halos which causes more large-scale bubbles. The **MeanRrec**, **FixedRion**, and **Classic** runs themselves show different evolutionary trends, with
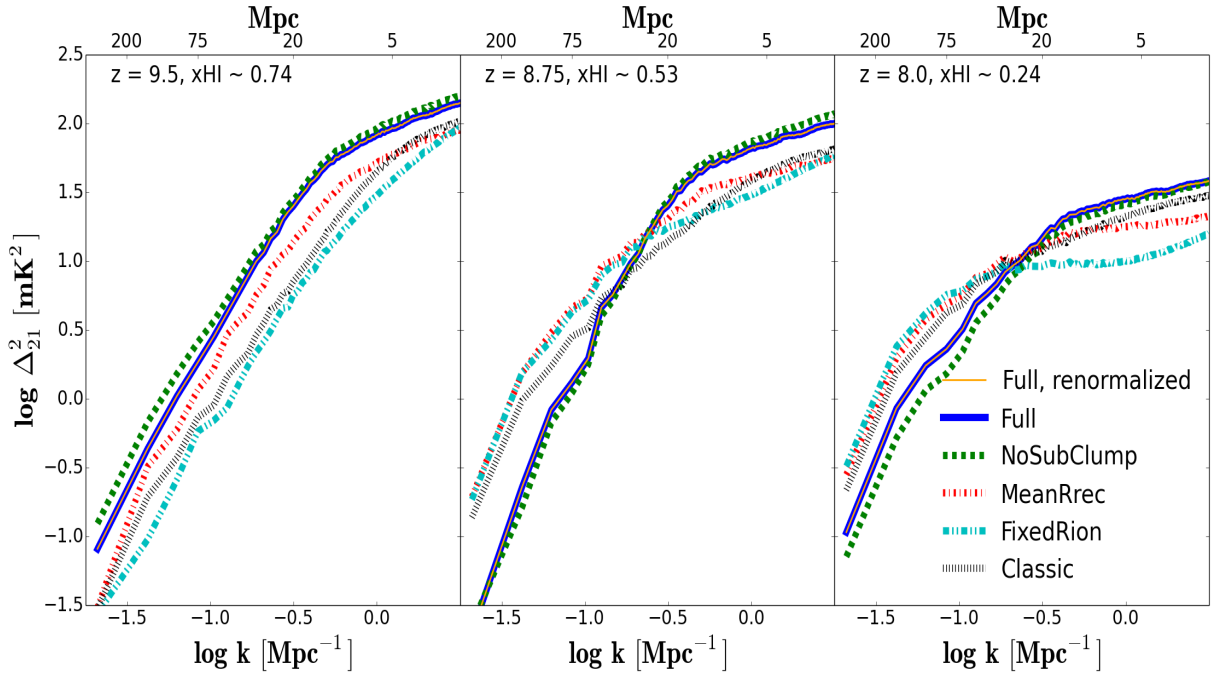
FIGURE 2.13: The power spectra of the 21-cm signal of the five models at different stages during the EoR. Variations in physical assumptions can result in $\times 2 - 3$ variations in the 21-cm power spectrum such as: $R_{\rm rec}$ suppresses the large-scale power spectrum while $R_{\rm ion}$ boosts the small-scale power spectrum.

FixedRion increasing its ionisation and 21-cm power spectra faster than the other two.

A comparison of the **MeanRrec** and **Classic** models in Figure 2.13 illustrates the significance of including a realistic treatment for the dependence of ionising efficiency on halo mass. Both models effectively adopt a spatially-homogeneous recombination rate and are explicitly tuned to reproduce τ. However, the **MeanRrec** (like the **Full** model) adopts the ionising efficiency in Figure 2.1 and Equation (2.2), which concentrates ionisations in overdense regions. Consequently, the **MeanRrec** model predicts more large-scale power at all times than the **Classic** model. This effect counteracts the suppression of large-scale power owing to spatially-inhomogeneous recombinations (Sobacchi & Mesinger, 2014). Note that the adopted dependence in Equation (2.2) is not arbitrary – it is taken from high-resolution hydrodynamic simulations that have been shown to be consistent with a range of observations of galaxies, absorbers, and reionisation (Finlator et al., 2015). Our results indicate that it is an important factor to consider when predicting the 21-cm power spectrum.

Finally, we compare the predicted 21-cm power spectrum from our new version
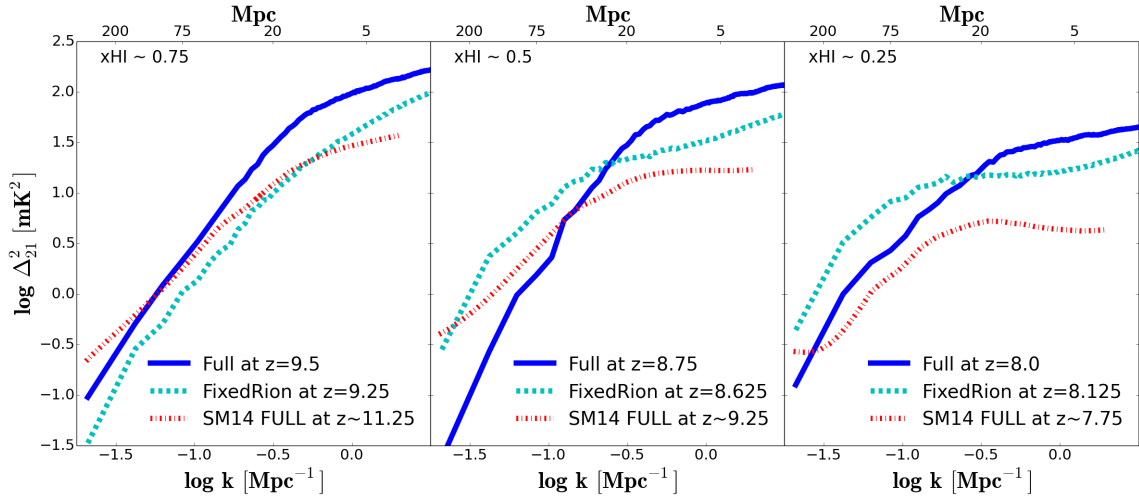
FIGURE 2.14: Comparison of the predicted 21-cm power spectrum between our **Full** (blue, solid) and **FixedRion** (dashed, cyan) models with the **FULL** model (dash-dotted, red) of SM14 (Sobacchi & Mesinger, 2014) at different neutral fraction. It is evident that the shape of the 21-cm power spectrum predicted from **FixedRion** model is similar to that of SM14 **FULL** model at all epochs, since both models share similar physical assumptions. Our **Full** model produces more power on small scales due to introducing non-linearly mass-dependent ionisations via R_{ion}.

of SimFast21 with those predictions from another semi-numerical simulation (Sobacchi & Mesinger, 2014, their **FULL** model) in Figure 2.14. SM14 **FULL** simulation accounts for inhomogeneous recombinations but uses only homogeneous ionisations via a constant efficiency parameter (ζ, similar to our **Classic** model). Thus, the SM14 model shares similar physical assumptions to our **FixedRion** model. From Figure 2.14, it is clear to see that the shape of the 21-cm power spectrum predicted from **FixedRion** model is qualitatively similar to that of the SM14 model at all epochs, but there is a tendency for the **FixedRion** model to produce somewhat more power as the EoR proceeds; this is possibly related to different density field contribution from different z. However, it is quite clear that our **Full** model predicts more power on small scales than models with homogeneous ionisations owing to non-linear ionisations.

To summarize, our new prescription for tracking non-linear ionisations and inhomogeneous recombinations results in predictions that differ significantly from models that do not include these effects, in particular yielding less power on scales of $\gtrsim 10$ Mpc, but more power on smaller scales. Consistent with Sobacchi & Mesinger (2014), we find that introducing inhomogeneous recombinations suppresses the power spectra of the ionisation field and 21-cm signal on large scales. We also find that introducing non-linear ionisations (via R_{ion}) boosts the small

scale power spectra of the ionisation fields and the 21-cm signal. These results highlight the importance of carefully considering the details of ionising sources and recombinations in making accurate predictions for future 21 cm EoR studies.

2.6   Conclusion

We have predicted the 21-cm power spectrum during the epoch of reionisation from a new and improved version of our semi-numerical code SIMFAST21. This new version has been modified to incorporate halo mass-dependent ionisation rates ($R_{\rm ion}$) and density-dependent recombination rates ($R_{\rm rec}$) rates as a function of redshift. We parameterise $R_{\rm ion}$ and $R_{\rm rec}$ from small-volume, high-resolution radiative hydrodynamic simulation (**6/256-RT**, Finlator et al. 2015) and a larger cosmological hydrodynamic simulation (**32/512**, Davé et al. 2013), that incoporate galaxy formation physics that has been well-constrained to match a wide range of observations down to lower redshifts. We have implemented these scalings into SIMFAST21 to identify the ionised regions, as opposed to using a uniform ionising efficiency parameter per halo mass (ζ) and no explicit recombinations as in the old version of SIMFAST21. Using this, we have studied the evolution of the neutral fraction and 21-cm power spectrum during reionisation.

Our main key findings are as follows:

- The mass-dependent ionisation rate $R_{\rm ion}$ scales super-linearly with halo mass as $M_h^{1.41}$, which is consistent with the SFR-M_h relation that previously found by Finlator et al. (2011). The recombination rate $R_{\rm rec}$ scale roughly as the density squared, though with deviations at high overdensities. Both display fairly tight relations that can be well-captured by analytic fitting formulae (eq. 2.2 and eq. 2.4).

- We tune our one free parameter, the ionising photon escape fraction, to be $f_{\rm esc} = 4^{+7}_{-2}\%$, in order to simultaneously match three key EoR observables: (i) The optical depth to Thomson scattering from Planck (2015); (ii) the ionising emissivity measured at $z \sim 5$ from Becker & Bolton (2013); (iii) the neutral fraction near end of reionisation from Fan et al. (2006); Becker et al. (2015); McGreer et al. (2015). This low $f_{\rm esc}$, independent of halo mass and redshift, highlights the importance of running large-volume simulations

to properly characterise the escape fraction $f_{\rm esc}$ and hence the ionising photon budget to complete reionisation. Note that this $f_{\rm esc}$ represents the escape fraction averaged over all halos within a $0.375h^{-1}$Mpc (comoving) cells, rather than $f_{\rm esc}$ from individual galaxies. To further concurrently match the SFR function measurements by Smit et al. (2012), a renormalization of $R_{\rm ion}$ by a factor of 1.5 is required, which then implies an escape fraction of 6%. This renormalization of $R_{\rm ion}$ and $f_{\rm esc}$ has no impact on the 21-cm power spectrum or other observables, since the total photon output remains the same.

- During the early EoR, the 21-cm power spectrum drops on large scales while staying constant on small scales, as small ionisation bubbles counteract the overall drop in cosmic H I density. At later stages, the bubbles grow larger and the power on large scales recovers. After the global neutral fraction drops below $\sim 10\%$ (at $z \sim 7.5$ in our simulation), the 21-cm power spectrum drops rapidly.

- Reionisation occurs earlier in our SimFast21 run than in the 6/256-RT simulation by $\Delta z \sim 0.5$, due to the small dynamic range of 6/256-RT that fails to capture the very earliest stages driven by the rarest overdensities, as well as large halos that are important during the later stages of the EoR. These results are well-converged with respect to simulation volume up to scales $\sim 1/4$ of the box size.

- Introducing non-linearly mass-dependent ionisations ($R_{\rm ion}$): (i) increases the duration of reionisation; (ii) boosts the 21-cm power at all scales by $\times 2 - 3$ during the early EoR; (iii) boosts the small-scale 21-cm power by $\times 2 - 3$ while lowering the large scale ($\gtrsim 5h^{-1}$Mpc) power during the late EoR. Qualitatively similar trends hold true for the ionisation field power spectra (**Full** versus **FixedRion**).

- Including spatially homogeneous recombinations using a globally-averaged recombination rate results in significantly more power on large scales and less power on small scales, since ionisation bubbles are able to grow to larger scales (**Full** versus **MeanRrec**).

- Including clumping effects on scales below our cell size ($0.375h^{-1}$Mpc) does not significantly affect the overall EoR topology or 21-cm power spectrum

(**Full** versus **NoSubClump**), though it does result in a lower ionisation fraction at moderate overdensities ($\Delta \sim 5 - 10$).

- In agreement with Sobacchi & Mesinger (2014), we find that inhomogeneous recombinations ($R_{\rm rec}$) matter a great deal (**Full** or **NoSubClump** versus **MeanRec**) in suppressing the large-scale power spectrum, but accounting further for the detailed dependence of recombination rate on density at scales smaller than our cell size changes results minimally, and only at fairly high overdensities (**Full** versus **NoSubClump**).

- Compared to the previous version of SimFast21 (**Classic**), our new version produces more small-scale 21-cm power and less large-scale power. It is generally most similar to a model that assumes a globally-averaged recombination rate (**MeanRrec**) or assumes a constant ionising output per unit halo mass (**FixedRion**).

- The power spectrum from the model of Sobacchi & Mesinger (2014) that account for recombinations but retain a fixed ionising output per unit halo mass is qualitatively similar to our **FixedRion** case, albeit with generally a lower amplitude.

- Our **Full** model shows a significantly higher median halo mass for ionizing photon output of $\sim 10^{10} M_\odot$, as opposed to $\sim 10^{8.5} M_\odot$ in the case of a constant ionising efficiency. This suggests that the majority of galaxies responsible for reionisation may be detectable with *Webb*; we leave a more detailed examination of this for future work.

- Incorporating the non-linear mass-dependent ionisation causes reionisation to complete at a later epoch by $\Delta z \sim 1$; this is a larger impact than that obtained by varying the recombination methodology.

Taken together, our results suggest that the details of how one models ionisation and recombinations can impact the strength and shape of the 21-cm power spectrum up to a factor of $\sim \times 3$. This is smaller than current observational uncertainties which are dominated by systematics, but might be significant for upcoming facilities such as HERA and SKA-Low. This work represents a step forward in accurately modeling the physical processes occuring during reionisation on large scales. In the next chapter we will use these models to make more

detailed predictions for the observability of the 21-cm power spectrum at various observationally-accessible epochs and scales.

We note that we have not considered any potential exotic sources of reionising photons. For instance, a recent paper by Madau & Haardt (2015) argues for quasars contributing significantly more than previously thought, indeed perhaps driving reionisation. Such a population of accreting black holes would provide an additional source of ionising photons that would once again vary how reionisation proceeds. Likewise, our radiation-hydrodynamic simulation did not properly track the contribution of mini-halos (i.e. those below the H cooling limit) to the ionising photon budget during reionisation, but there are no observational constraints that limit this. Our SimFast21-based modeling framework provides a way to explore these variations and their impact on observables such as the 21-cm power spectrum, in order to facilitate more optimal scientific interpretation of forthcoming 21-cm and other EoR observations.

Chapter 3

Epoch of Reionisation 21cm Forecasting From MCMC-Constrained Semi-Numerical Models

Abstract

The recent low value of Planck (2016) integrated optical depth to Thomson scattering suggests that the reionisation occurred fairly suddenly, disfavoring extended reionisation scenarios. This will have a significant impact on the 21cm power spectrum. Using a semi-numerical framework, we improve our model from the previous chapter to include time-integrated ionisation and recombination effects, and find that this leads to more sudden reionisation. It also yields larger H II bubbles which lead to an order of magnitude more 21cm power on large scales, while suppressing the small scale ionisation power. Local fluctuations in the neutral hydrogen density play the dominant role in boosting the 21cm power spectrum on large scales, while recombinations are subdominant. We use a Monte Carlo Markov Chain approach to constrain our model to observations of the star formation rate functions at $z = 6, 7, 8$ from Bouwens et al. (2015), the Planck (2016) optical depth measurements, and the Becker & Bolton (2013) ionising emissivity data at $z \sim 5$. We then use this constrained model to perform 21cm forecasting for LOFAR, HERA, and SKA in order to determine how well such data can characterise the sources

driving reionisation. We find that the 21cm power spectrum alone can somewhat constrain the halo mass dependence of ionising sources, the photon escape fraction and ionising amplitude, but combining the 21cm data with other current observations enables us to separately constrain all these parameters. Our framework illustrates how 21cm data can play a key role in understanding the sources and topology of reionisation as observations improve.

3.1 Introduction

The redshifted 21cm neutral hydrogen line from the Epoch of Reionisation (EoR) provides numerous astrophysical and cosmological information about the formation and evolution of the first stars and galaxies (Barkana & Loeb, 2001). Many ongoing and forthcoming experiments such as the Low Frequency Array (LOFAR)[1], the Hydrogen Epoch of Reionisation Array (HERA)[2], and the Square Kilometre Array (SKA-Low)[3], are devoted to observing the diffuse neutral hydrogen gas that traces the cosmic web at redshifts beyond 7. While current experiments only yield upper limits to the measurements of the 21cm power spectrum, these future experiments are likely to provide a detection in the near future. It is thus important to develop robust and comprehensive theoretical models that can utilise such information, along with observations from other wavelengths and facilities, in order to optimally constrain the physical processes driving reionisation.

The recent low value of Planck (2016) integrated optical depth to Thomson scattering suggests that the EoR may have occurred more suddenly, and at much later times, than what was previously believed (Hinshaw et al., 2013). The low value of $\tau = 0.058 \pm 0.012$ prefers EoR models with late onset and shorter duration. This, in turn, is expected to have a significant impact on the expected 21cm signal and its evolution. Proper modeling of the sources and sinks of ionising photons during the EoR is required to accurately model the H II bubbles and study their sizes and distributions. Doing so will enable us to connect the observed 21cm power spectrum with the physical properties of the sources and sinks of ionising photons during the EoR.

---

[1]http://www.lofar.org/
[2]http://reionization.org
[3]https://www.skatelescope.org

There are several major challenges to modeling the EoR and its redshifted 21cm signal, driven by the requirements for accurately modeling the power spectrum of H I on large scales. These requirements include: (i) large volumes (~ 500 Mpc) in order to capture the large scale H I fluctuations that will be detected in upcoming 21cm observations; (ii) high resolution that is sufficient to resolve the ionising sources and self-shielding systems on sub-kpc scales (Iliev et al., 2015); and (iii) accurate tracking of the ionising radiation and other feedback processes from the sub-kpc up to Mpc scales. For these reasons, self-consistently simulating the EoR represents an immense computational challenge that no current model has been able to fully meet.

Nonetheless, great progress has been made in simulating the EoR on both small and large scales. Hydrodynamic simulations that self-consistently incorporate radiative transfer (Gnedin 2000, 2014; Pawlik & Schaye 2008; Finlator et al. 2009, 2013; Katz et al. 2016) have sufficient resolution to model the sources of reionisation direction, and to propagate the emitted radiation through the intergalactic medium (IGM) with minimal physical assumptions. However, owing to computational limitations they are currently restricted to volumes smaller than ~ 20 Mpc in order to resolve all atomically-cooling halos. An alternative approach is to post-process simulated density fields with radiative transfer (Razoumov et al 2002; Mellema et al 2006; McQuinn et al 2007; Thomas et al 2009; Iliev et al. 2014; Bauer et al. 2015), which allows access to larger volumes but does not self-consistently account for thermal, ionisation, and chemical feedback effects on galaxy formation. Semi-analytical EoR models (Mitra et al., 2011, 2013) are very successful in studying and constraining the globally averaged astrophysical quantities and parameters during EoR (Mitra et al., 2015) based on current observations, but lack the dynamic range to study 21cm fluctuations. Finally, on the very largest scales, semi-numerical models (Mesinger & Furlanetto 2007; Zahn et al 2007; Choudhury et al. 2009; Santos et al. 2010) based on quasi-linear density evolution with coarse modeling of the source population are able to access volumes sufficient to make 21cm predictions relevant to upcoming observations, but must employ simple parameterised approximations for the source and sink populations. Nonetheless, such semi-numerical models, with appropriate tuning, can reproduce similar reionisaion histories as obtained by full radiative transfer simulations (Zahn et al. 2011; Majumdar et al. 2014).

Semi-numerical models are most ideally suited for studying the large-scale ($\gtrsim 1$ Mpc)

21cm power spectrum that will be measured with upcoming radio facilities, but they make many simplifying assumptions. In particular, they must assume parameterisations for the relationship between halo mass and ionising luminosity, and the relationship between the large-scale density field and the recombination rate that emerges from small-scale clumping. Also, current semi-numerical codes treat a single cell as either fully neutral or fully ionised, hence they must choose some condition to assign that cell as ionised. This third condition is an algorithmic choice, but the first two connect to physics, as they provide an opportunity to constrain astrophysical quantities associated with EoR sources and sinks based on 21cm and other EoR observations.

In the previous chapter, we focused on improving the physical parameterisations of the source and sink populations in the semi-numerical model SimFast21 by employing parameterised results from high-resolution radiative hydrodynamic simulations. This enabled greater physical realism of parameterised source and sink populations compared to previous approaches that had used a linear relationship between halo mass and luminosity, and did not include recombinations. To do this, we obtained parametrizations for the ionisation rate $R_{\rm ion}$ and recombination rate $R_{\rm rec}$ as functions of halo mass, overdensity, and redshift, extracted from high resolution radiative transfer hydrodynamic simulation (Finlator et al., 2015) (hearafter 6/256-RT) and larger-volume hydrodynamic simulation (Davé et al., 2013) (hereafter 32/512). We then implemented these parametrizations into SimFast21, and identified ionised regions where the ionisation rate exceeded the recombination rate. This more realistic modeling replaces the canonical efficiency parameter ζ approach in previous semi-numerical EoR modeling. In particular, we found that the $R_{\rm ion}$ scales super-linearly with halo mass ($R_{\rm ion} \propto M_h^{1.4}$) in contrast to the typically assumed linear relationship between the efficiency parameter ζ and halo mass. We showed that using these new parametrizations ($R_{\rm ion}$ and $R_{\rm rec}$) allows us to simultaneously match various EoR key observables with a relatively low escape fraction, independent of halo mass and redshift. We also found that the $R_{\rm ion}$ boosts the small scale 21cm power spectrum while $R_{\rm rec}$ suppresses the 21cm power on large scales during cosmic reionisations.

These parametrizations thus improved upon the first two major uncertainties in semi-numerical models, namely the ionisation and recombinations. However, this work still assumed an ionisation condition based on the *instantaneous* balance

between ionisations and recombinations – in other words, if there were instantaneously more ionisations than recombinations, that volume of space was considered fully ionised. However, this is not physically fully accurate, because the excess ionising photons in such regions still must ionise the neutral hydrogen atoms in that region. The instantaneous criterion thus does not account for partial ionisation of a given cell, thus it underestimates the total number of photons required. In the limiting case where reionisation proceeds quickly, this may not be a bad approximation, but ideally we aim to relax this instantaneous assumption. In essence, it is likely that our ionisations were too efficient, which can affect the topology and duration of the EoR along with our constraints on f_{esc}.

In this chapter, we improve upon our previous ionisation condition by tracking the actual number of neutral hydrogen atoms, ionising photons, and recombinations. This leads to a time dependent ionisation condition that is analogous to the well-known ionisation balance equation. With this, it turns out that reionisation occurs more suddenly, as preferred by the recent Planck (2016) constraints, but requires a higher escape fraction. We compare this to our previous Instantaneous EoR model in terms of their H II bubble sizes, EoR history, and 21cm power spectra.

Ideally, we would like to use the 21cm power spectra and other observations to provide constraints on the nature of the source population, in particular its relationship to the halo population. In the previous chapter, we manually constrained the relationship between ionising emissivity and halo mass versus observations, since we only had one free parameter, namely the escape fraction of ionising photons. This was because we had fixed the characteristics of the source population based on our radiative hydrodynamic simulations. Here we would like to relax this assumption, and determine how well we can constrain the source population characteristics directly from observations. To do this, we consider a generalised model with three free parameters: the escape photon fraction f_{esc}, the ionising emissivity amplitude A_{ion} (R_{ion} amplitude), and the ionising emissivity-halo mass power-law index C_{ion}. We note that C_{ion} can represent the power-law mass dependence of either the amplitude A_{ion} or the escape fraction f_{esc}; in our current approach, these two quantities are degenerate. To constrain these parameters, we perform a Bayesian Monte Carlo Markov Chain (MCMC) search against current EoR observations. We then forecast how these constraints will be improved by upcoming 21cm observations from LOFAR, HERA, and SKA-Low. By considering all such observations, we determine how well we can constrain the EoR source

population as characterised by our three free parameters.

This chapter is organized as follows: In section 4.2, we introduce our previous Instantaneous EoR model and our new Time-integrated model. We study and compare these models' impact on various EoR observables including the 21cm power spectrum in section 3.3. In section 3.4, we create several EoR models to study their effects on the 21cm power spectrum. In section 3.5, we calibrate the Time-integrated model to various EoR observations. We perform the 21cm forecasting in section 3.6 and draw our concluding remarks in section 3.7.

Throughout this work, we adopt a ΛCDM cosmology in which $\Omega_{\mathrm{M}} = 0.3$, $\Omega_{\Lambda} = 0.7$, $h \equiv H_0/(100\,\mathrm{km/s/Mpc}) = 0.7$, a primordial power spectrum index $n = 0.96$, an amplitude of the mass fluctuations scaled to $\sigma_8 = 0.8$, and $\Omega_b = 0.045$. We quote all results in comoving units, unless otherwise stated.

3.2 Simulations

We use a semi-numerical code SimFast21 (Santos et al. 2010), which we briefly review here. SimFast21 simulation begins by generating the density field from a Gaussian distribution using a Monte-Carlo approach. The generated density field will then be dynamically evolved from linear to non-linear regime by applying the Zel'dovich (1970) approximation. The dark matter halos are generated using the well-known excursion-set formalism. In the standard SimFast21, the ionised regions are identified using the excursion-set formalism based on a constant efficiency parameter ζ. In the original SimFast21 code, the ionisation condition compares the amount of collapsed dark matter halo f_{coll} to the efficiency parameter ζ – any region will be flagged as ionised if:

$$f_{coll} \geq \zeta^{-1}. \tag{3.1}$$

The efficiency parameter ζ is a model free parameter which can be tuned to match some observations. This condition generates the ionisation field, which may be used along with the density field to obtain the 21cm brightness temperature.

We now describe our two extensions to SimFast21. The first was presented in the previous chapter, which we review next, and incorporates the ionisation and recombination rate parameterisations taken from hydrodynamic simulations, but

utilises an instantaneous ionisation condition. We then describe our further extension here in order to improve the ionisation condition by tracking the neutral fraction in a time-integrated manner. We will call this the "Instantaneous ionisation" and "Time-integrated ionisation" models.

3.2.1 Instantaneous ionisation model

As described in the previous chapter, here we replace the efficiency parameter ζ with direct parameterisations of the ionisation rate R_{ion} and recombination rate R_{rec} as functions of halo mass M_h, overdensity Δ, and redshift z, taken from our 6/256-RT and 32/512 simulations. Our best-fit non-linear ionisation rate R_{ion} parametrization takes the following form:

$$\frac{R_{\mathrm{ion}}}{M_h} = A_{\mathrm{ion}} \, (1+z)^{D_{\mathrm{ion}}} \, (M_h/B_{\mathrm{ion}})^{C_{\mathrm{ion}}} \, \exp\left(-(B_{\mathrm{ion}}/M_h)^{3.0}\right), \qquad (3.2)$$

where $A_{\mathrm{ion}} = 1.08 \times 10^{40} \, \mathrm{M_\odot^{-1} s^{-1}}$, $B_{\mathrm{ion}} = 9.51 \times 10^7 \, \mathrm{M_\odot}$, $C_{\mathrm{ion}} = 0.41$ and $D_{\mathrm{ion}} = 2.28$. Meanwhile, we parameterise the recombination rate as:

$$\frac{R_{\mathrm{rec}}}{V} = A_{\mathrm{rec}}(1+z)^{D_{\mathrm{rec}}} \left[\frac{(\Delta/B_{\mathrm{rec}})^{C_{\mathrm{rec}}}}{1+(\Delta/B_{\mathrm{rec}})^{C_{\mathrm{rec}}}}\right]^4, \qquad (3.3)$$

where $A_{\mathrm{rec}} = 9.85 \times 10^{-24} \mathrm{cm^{-3} s^{-1}}$, $B_{\mathrm{rec}} = 1.76$, $C_{\mathrm{rec}} = 0.82$, $D_{\mathrm{rec}} = 5.07$.

Our ionisation condition is taken to be

$$f_{\mathrm{esc}} R_{\mathrm{ion,V}} \geq R_{\mathrm{rec,V}}, \qquad (3.4)$$

where

$$R_{\mathrm{ion,V}} = \int_{dn} \int_V \frac{dn}{dM_h} R_{\mathrm{ion}}(M_h, z) \, dM_h \, dV,$$

and

$$R_{\mathrm{rec,V}} = \int_V R_{\mathrm{rec}}(\Delta, z) \, dV.$$

In above expressions, the f_{esc} is the photon escape fraction, V is the spherical region volume specified by the excursion set-formalism, and n is the number density of halos. With these volume integrals, the $R_{\mathrm{ion,V}}$ represents the total ionisation rate from all sources and $R_{\mathrm{rec,V}}$ is the maximum recombination rate in that volume V.

Cells in a given volume V satisfying this criterion (equation 3.4) are considered fully ionised, otherwise they are fully neutral.

Using this model, it has been shown in the previous chapter that one can match simultaneously several EoR key observables, such as Planck (2015) optical depth, Becker & Bolton (2013) ionising emissivity and Fan et al. (2006) filling factor measurement, by only a constant $f_{esc} = 4-6\%$ independent of halo mass or redshift.

3.2.2 Time-integrated ionisation model

The model introduced in the previous chapter (our Instantaneous EoR model) has several drawbacks. First, the ionisation condition, equation (3.4), is an instantaneous criterion which compares the escaped ionisation rate $f_{esc}R_{ion}$ with the recombination rate R_{rec}, instead of comparing the actual numbers of ionising photons to that of recombinations. Second, the ionisation condition, equation (3.4), assumes maximum recombination rate R_{rec} from all cells/regions as if they were fully ionised.

To improve on these, we modify the ionisation condition to account for the evolving neutral hydrogen fraction, which allows us to account for the existing number of hydrogen atoms in each region as well as to compute the recombination based on the current ionised fraction. Hence we now employ a time dependent integral ionisation condition:

$$f_{esc}R_{ion,V} \ dt \geq \mathbb{R}_{rec,V} \ dt + N_{HI,V} \, , \tag{3.5}$$

where

$$\mathbb{R}_{rec,V} = \int_V x_{HII} \, R_{rec}(\Delta, z) \, dV \, ,$$

and

$$N_{HI,V} = \int_V (1 - x_{HII}) \, N_H \, dV.$$

The x_{HII} and N_H here are the ionisation fraction and the total number of hydrogen in cells respectively. The dt represents the time duration between successive snapshots. We apply this new condition (equation 3.5) as follows: for each cell, we first compute the integrand of the LHS ($f_{esc}R_{ion}dt$) and RHS ($x_{HII}R_{rec}dt + (1-x_{HII})NH$). We then apply the excursion set formalism to perform the spherical volume integral. Once again, the ionisation fraction is set to 1 (fully ionised) for cells in

volumes that satisfy the ionisation condition (equation 3.5), otherwise they remain fully neutral with zero ionisation fraction.

The left hand side (LHS) of our new ionisation condition (equation 3.5) represents the actual number of escaped ionising photons being emitted in dt. The first term of the right hand side (RHS) of this condition is the actual number of recombinations occurring during dt in regions with an ionisation fraction of x_{HII}. This term then tracks the exact number of recombinations even from partially ionised regions with $0 < x_{HII} < 1$. This recombination term has no effect at early times of EoR when the universe is completely neutral, but becomes the dominant sink for ionising photons at late stages of the EoR (Sobacchi & Mesinger, 2014).

The second term of the RHS of equation (3.5) denotes the total number of neutral hydrogen in the simulation box. At early EoR stages, the escaped ionising photons (LHS) fights only with the neutral hydrogen term $(1 - x_{HII})N_H$. As the EoR proceeds, the neutral hydrogen term becomes less significant, and the recombinations start to play the leading role in forestalling reionisation. Hence this provides a more physically motivated ionisation condition, in a similar form to the standard ionisation balance equation.

The condition is clearly time-dependent, unlike the Instantaneous ionisation model for which the ionisation condition could be evaluated independently at each time-step. Thus our new scheme can be sensitive to the choice of the time-step dt used to perform the integration. For instance, a larger $dt(dz)$ will result in more ionising photons and also more recombinations. This then leads to a wrong evolving ionisation balance. We have conducted convergence tests to determine that $dz = 0.125$ provides a numerically-converged answer. Our new method thus requires higher computational cost to evolve the ionisation state forward in time. We will explore possible variations of the ionisation condition from equation (3.5) in §3.4, to study their impact on the 21cm power spectrum.

It turns out, as we will show, that the instantaneous ionisation condition results in more extended reionisation history, while our new time-integrated condition yields more sudden reionisation. Next, we will investigate their differences in terms of the EoR history, topology, and the 21cm power spectrum.

3.3   Impact on EoR observables

We use the Full model from the previous chapter as our fiducial "Instantaneous" reionisation model. This model uses equation (3.4) to identify the ionised regions with $f_{\mathrm{esc}} = 4\%$ in a large volume box of $L = 300$ Mpc and a number of cells $N = 560^3$. This model yields a maximum halo mass of $3.56 \times 10^{12} M_\odot$ and a minimum halo mass of $1.28 \times 10^8 M_\odot$ at z=6. We have shown that this model matches various observations of the EoR including the Planck (2015) optical depth $\tau = 0.066$. Using the same density field boxes and halo catalogues, we run our new Time-integrated reionisation model with parameters calibrated against various EoR key observations (see section 3.5), including the new Planck (2016) optical depth. The two models are tuned to different τ_e values, but we do our 21cm comparison at a given neutral fraction since it has been shown that the 21cm power spectrum shape is more sensitive to the neutral fraction (e.g. see Zahn et al 2007; Mesinger & Furlanetto 2007). We also verify this later by comparing the Instantaneous model power spectra at different redshifts for a fixed neutral fraction in figure 3.5 in §3.3.3. We thus begin by comparing the Instantaneous and Time-integrated models' differences in terms of their global neutral fraction history.

3.3.1   EoR ionisation history

Figure 3.1 shows the global reionisation history produced by our two fiducial models, Instantaneous and Time-integrated, compared to the neutral fraction constraints obtained by Bouwens et al. (2015) via a compilation from various observables. We immediately see that the green line showing the new time-integrated ionisation condition shows a more sudden transition from fully ionised to fully neutral. Meanwhile, the blue line from our old instantaneous condition results in a more extended reionisation epoch. Nonetheless, in both cases, reionisation occurs in our two models within observational constraints (light-red shaded areas). It is perhaps worth noting that, unlike a few years ago when the canonical redshift for the end of reionisation was regarded as $z \sim 6$, current constraints from both observations and models favors the end of reionisation to occur at $z \sim 7$ or perhaps a bit higher, as the recent Planck (2016) measurements of the optical depth infer.
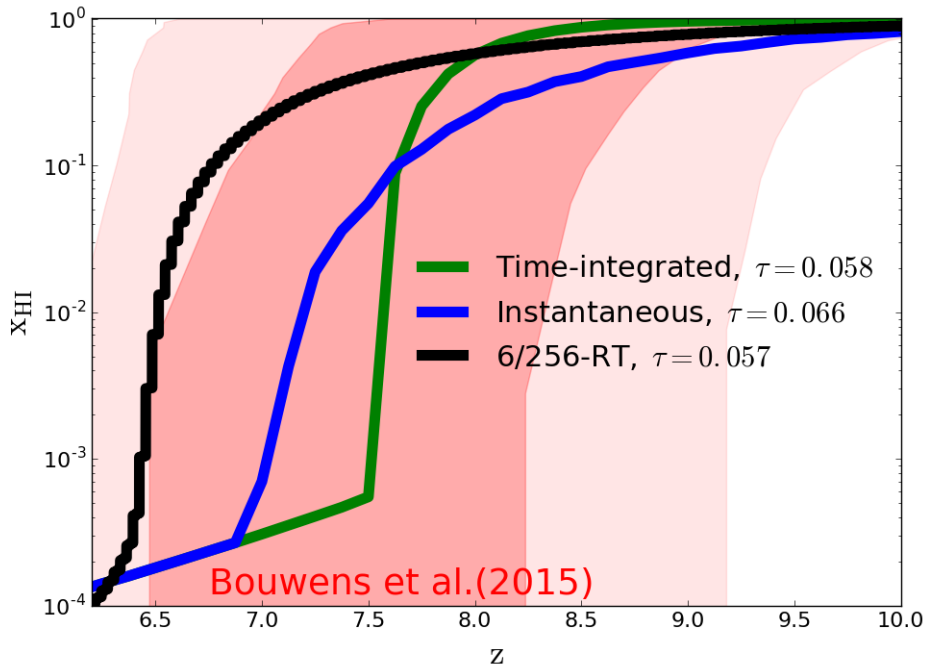
FIGURE 3.1: The volume-weighted average neutral fraction evolution as a function of redshift. The Time-integrated EoR model ($\tau = 0.058$), the Instantaneous EoR model developed in the previous chapter ($\tau = 0.066$), and the 6/256-RT simulation ($\tau = 0.057$) are represented by the green, blue, black lines, respectively. The shaded areas are several quasars and ly-α constraints as compiled by Bouwens et al. (2015). Its quite clear that all models are consistent with the observational constraints by Bouwens et al. (2015). Differences between models are explained in the text.

This plot already shows that accounting for the neutral gas through comparing the number of neutral atoms and ionising photons (equation 3.5) versus comparing instantaneous rates (equation 3.4) has a significant impact on the reionisation history. The Time-integrated model is qualitatively more compatible with the picture that has been suggested by recent Planck (2016) constraints that favours sudden EoR scenarios. We emphasize the fact that if we tune the Time-integrated model optical depth to match the Instantaneous model optical depth ($\tau = 0.066$, Planck 2015), the Time-integrated model will require higher f_{esc} and shift reionisation towards higher redshifts, but nevertheless the reionisation history shape will remain sudden as shown later in figure 3.9. We will come back to this point later in §3.5.2.2. However, when using the same parameters, the reionisation in the time-integrated model is delayed by $\Delta z \sim 0.8$ as compared with that in the instantaneous model.

From figure 3.1, we also see that both models Instantaneous and Time-integrated
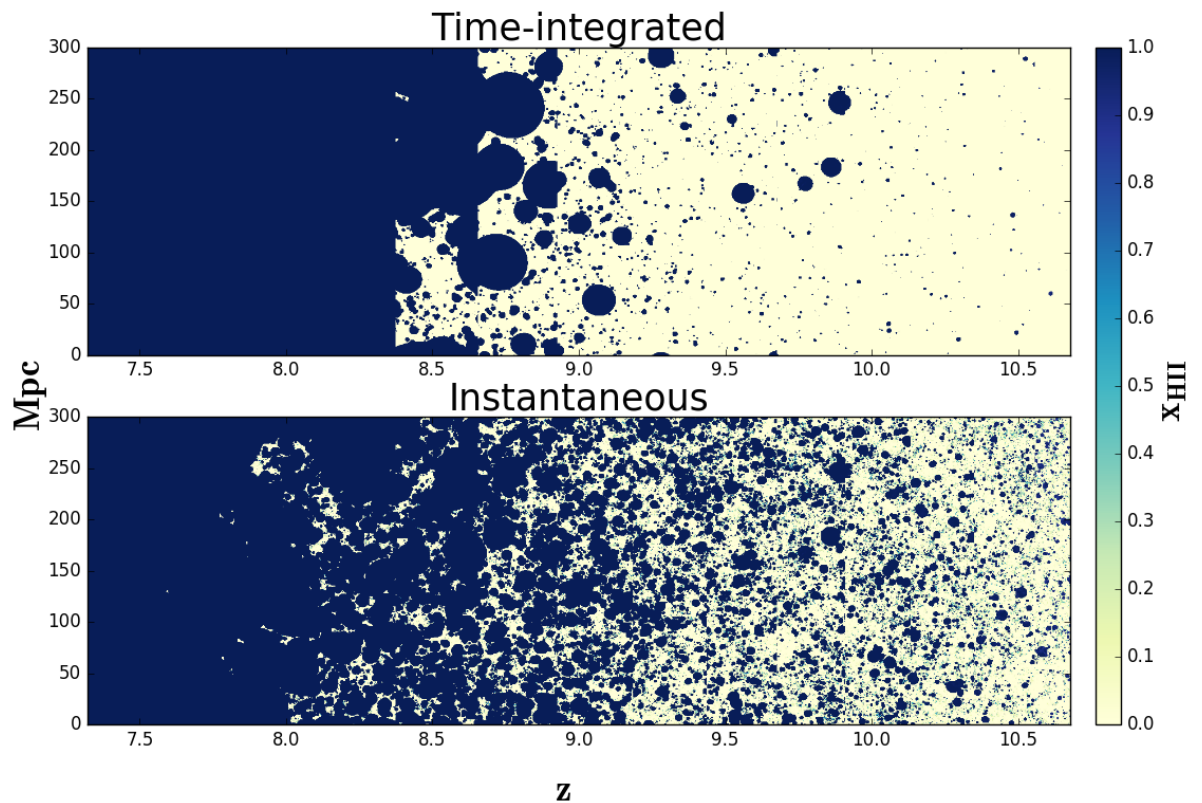
FIGURE 3.2: Evolving maps of the neutral fraction from the Instantaneous and Time-integrated models. Time-integrated EoR model produces large HII bubbles and reionises the universe very rapidly, indicating a sudden EoR scenario. Instantaneous EoR model yields small HII bubbles and reionises the universe very late, leading to an extended EoR scenario.

reionise the universe earlier than the 6/256-RT simulation. As discussed before in the previous chapter, the small box size (6 h^{-1} Mpc) of 6/256-RT does not capture the large scale fluctuations that give rise to the most massive halos that provide a significant fraction of reionising photons. Hence at a fixed optical depth, it is expected that the 6/256-RT might reionise the universe much later than the Time-integrated model due to the box size limitations.

An informative way to examine these models is by viewing light cones, as shown in Figure 3.2. These have been constructed by projecting the ionisation state within the simulation volume along a specific line-of-sight, evolving with redshift. One ideally might rotate, flip and shift the 21cm boxes along the light-of sight in creating these light cones, which might reduce the sharp disconnected boundaries. However, we ignore to apply these operations since our box is very large and the aim is simply to show the difference in reionization evolution (extended vs sudden). These operations are more important when constructing a single integrated map

such as in studies of the kinematic Sunyaev-Zel'dovich (KSZ) effect (e.g. Gnedin & Jaffe , 2001). Figure 3.2 confirms that our previous model (the **Full** model from the previous chapter) produces a more extended EoR scenario that corresponds to an early onset and a very late end with a duration of $\Delta z \sim 10$ [4]. Unlike the Instantaneous model, figure 3.2 also shows that our new model (equation 3.5) yields a sudden reionisation scenario where the EoR starts very late (once $x_{HI} <$ 1.0) and ends (when x_{HI} drops below 10^{-3}) very quickly within a duration of $\Delta z \sim$ 4. More strikingly, it also shows that the Time-integrated EoR model produces larger ionised bubbles while the Instantaneous model yields many ionised bubbles of smaller sizes. This can further be quantified by studying their differences in terms of the ionisation field power spectra.

3.3.2   EoR topology

It is useful to compare the models at a specific neutral fraction, since this best illustrates the difference in topology. Figure 3.3 compares our Instantaneous and Time-integrated models in terms of their ionisation maps when the EoR is half-way through, i.e. with a globally-averaged $x_{HI} \sim 0.5$. These ionisation maps show the spatial distribution of the large and small ionised bubbles (black regions) over 300 Mpc scales. However, the excursion set-formalism with its binary structure (fully ionised or fully neutral), along with the large cell size of ~ 0.5 Mpc, prevents these models' maps to display the self-shielded regions in the ionised mediums as seen in figures 3.3 and 3.2. The presence of these self-shielded regions does not affect the 21cm power spectrum but rather lower the ionisation fraction at intermediate densities ($\Delta = 5-10$) as previously shown (see figure 2.10 in the previous chapter). We also have shown previously that including the sub-clumping effect on scales below our cell size (~ 0.5 Mpc) have a minimal effect on the expected signal (see comparison between **Full** and **NoSubClump** models in the previous chapter). From Figure 3.3, we see that the Instantaneous model produces many small H ii bubbles more uniformly distributed across the ionisation map. This shows that the EoR in the Instantaneous model proceeds from small scales, and the ionising photons are able to reionise locally everywhere. This is because the instantaneous ionisation rate can easily exceed the recombination rate (see equation (3.4)) on small scales when neglecting the local neutral hydrogen content.

---

[4]This duration might be clearly seen if these light-cones are displayed from $z = 20 - 6$, but nevertheless it is clear that EoR has started early and slowly in the Instantaneous model.
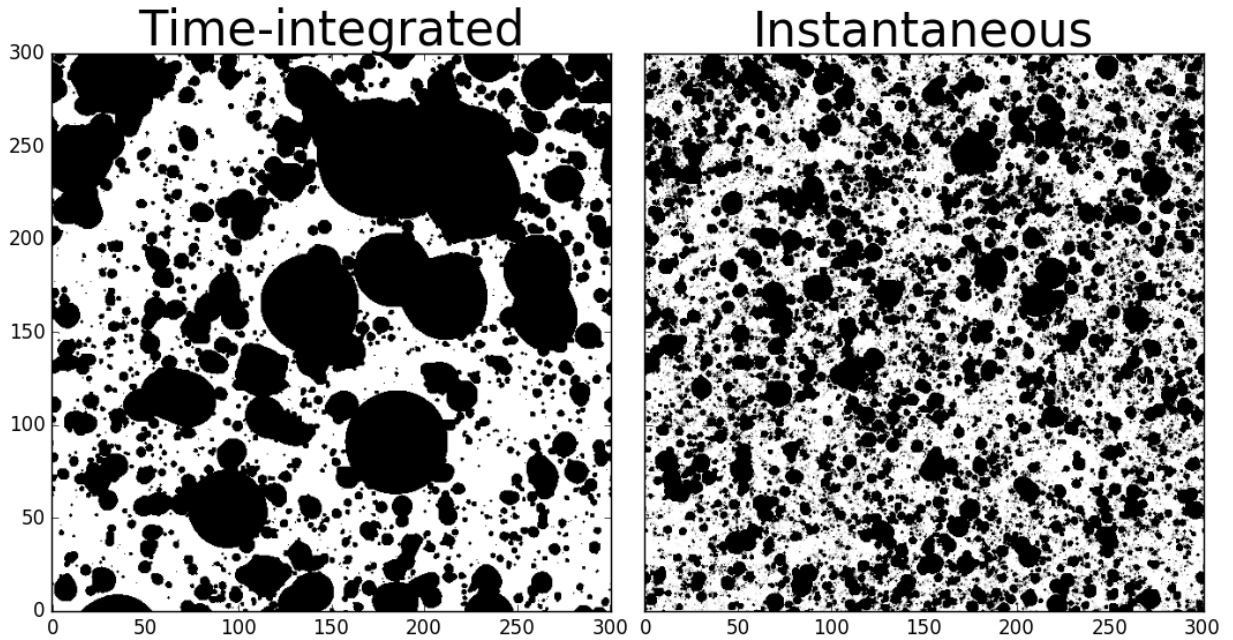
FIGURE 3.3: Slice of the ionistion box of a size $300 \times 300 \times 0.535\,\mathrm{Mpc}^3$ from the Instantaneous and Time-integrated models and at $\mathrm{x_{HI}} \sim 0.5$. White and black represent neutral and ionised regions respectively. The self-shielded regions in ionised mediums are absent due to the binary structure of the excursion set formalism (assigning 1 to ionised and 0 to neutral cells in regions that satisfy the ionised condition) along with the large cell size of ~ 0.5 Mpc.

In contrast, the Time-integrated model ionisation map shows very large H II bubbles. This may be explained by interpreting the Time-integrated model ionisation condition (equation 3.5). As noted earlier, at high redshifts when the universe is neutral ($\mathrm{x_{HII}} \sim 0$), the recombination term can be neglected. In this case, the Time-integrated model only compares the escaped ionising photons with the total number of neutral hydrogen atoms. This condition dominates until the region becomes partially ionised. At that point, recombinations will start to occur because of the nonzero ionisation fraction $\mathrm{x_{HII}}$, but still this region is now less neutral, which will allow more rapid ionisation. However, different forms of ionisation condition yield very different HI fluctuations (see §3.4). In general, the sources and sinks are occurring within the regions that are densest and thus contain the most number of neutral hydrogen atoms. The high density causes the ionising photons to be ineffective at ionising local regions, until such time as significant ionisations happen, which then rapidly ionise the surrounding regions.

Figure 3.4 shows the ionisation field power spectra of our fiducial models at different stages of reionisation when the universe is 25%, 50% and 75% reionised. These neutral fractions correspond to z=8.0,8.75,9.5 and z= 7.75,8.0,8.25 as obtained by
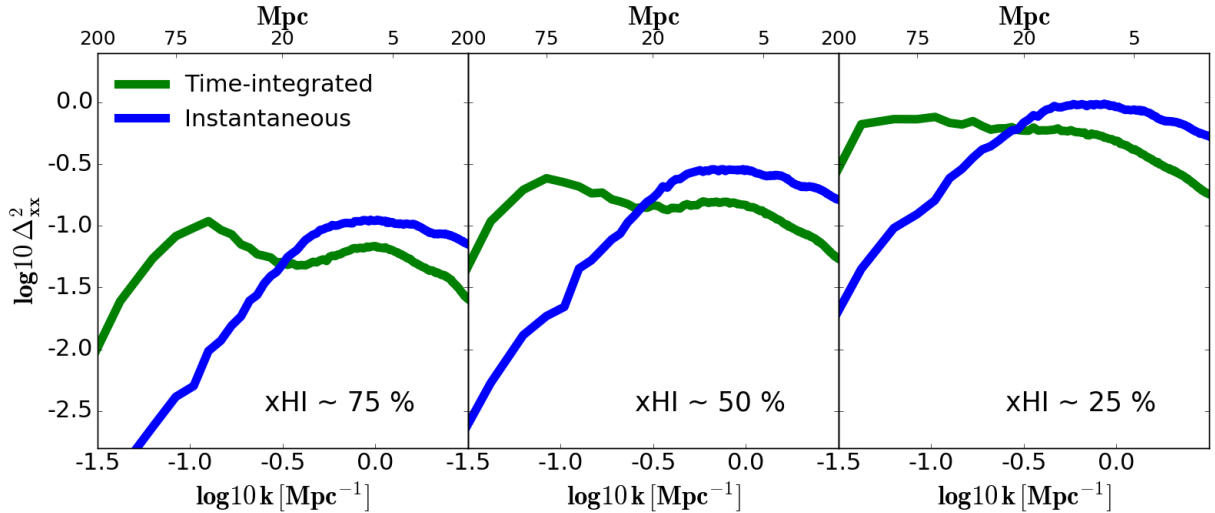
FIGURE 3.4: Ionization field power spectrum comparison between the Instantaneous (blue) and Time-integrated (green) models at different stages of reionisation ($x_{HI} \sim$ 25%, 50%, 75%.)

the Instantaneous and Time-integrated models respectively. This is computed as follows: $\Delta^2_{xx} \equiv k^3/|(2\pi^2 \, V) < |x_{HII}|^2 > /x^2_{HI}$.

The Time-integrated model produces more power on large scales by 1-1.2 order of magnitude and less power on small scales by a factor of 2-3, at fixed ionisation fraction, as compared to the Instantaneous model. This is consistent with the qualitative impression from the ionisation maps in Figure 3.3. We further see that the large scale ionisation power spectrum, obtained by the Time-integrated EoR model, peaks at $\sim$ 75Mpc which corresponds to the characteristic size of the H II bubbles as seen in the H II maps in figure 3.3.

The difference particularly on large scales is substantial, which shows the importance of accounting for the existing neutral hydrogen content in the ionisation condition (i.e. the second term of equation (3.5)). Since the fluctuations in the ionisation field drive the 21cm brightness temperature, we expect to see similar differences in the 21cm power spectra, which we examine next.

3.3.3 The 21cm power spectrum

Using the ionisation fields of these models, we now compute our EoR key observable which is the 21cm power spectrum. Assuming that the spin temperature is much higher than the CMB temperature, the 21cm brightness temperature takes

the following form:

$$\delta T_b(\nu) = 23 \mathrm{x}_{\mathrm{HI}} \Delta \left(\frac{\Omega_b h^2}{0.02} \right) \sqrt{\frac{1+z}{10} \frac{0.15}{\Omega_m h^2}} \left(\frac{H}{H + dv/dr} \right) \mathrm{mK}, \qquad (3.6)$$

where dv/dr is the comoving gradient of the line of sight component of the co-moving velocity. Using this equation, it is straightforward to create the 21cm brightness temperature boxes from which we compute the 21cm power spectrum as follows: $\Delta_{21}^2 \equiv \mathrm{k}^3/(2\pi^2\,\mathrm{V}) < |\delta \mathrm{T_b(k)}|_{\mathrm{k}}^2 >$.

We first verify that the 21cm power spectrum is primarily sensitive to the global ionisation fraction, while the density field evolution is secondary. Note that the 21cm fluctuations traces those of the density field only at early times when the universe is almost neutral. Here we quote results for the Instantaneous model, but we expect that this is also valid for other models such as our Time-integrated model. We tune the Instantaneous model to Planck (2016) optical depth ($\tau = 0.058$) which yields $\mathrm{x_{HI}} = 0.75, 0.54, 0.277$ at $\mathrm{z} = 8.75, 8.00, 7.25$ respectively. We then re-tune the model to the Planck (2015) optical depth ($\tau = 0.066$) (similar to our previous **Full** model from previous chapter) to obtain $\mathrm{x_{HI}} = 0.73, 0.53, 0.25$ at $\mathrm{z} = 9.5, 8.75, 8.0$ respectively. We now compare their difference in the 21 power spectrum at these different redshifts for a fixed neutral fraction in figure 3.5. Comparing the solid blue line with black dashed line, we find the the Instantaneous model produces the exact 21cm power spectrum at a fixed neutral fraction, irrespective of the density field evolution at different redshifts. Hence we will compare different models at similar neutral fractions, not similar redshifts.

Figure 3.5 shows the 21cm power spectrum of the Instantaneous and Time-integrated models at neutral fractions of 25%, 50% and 75%. Mimicking the ionisation field power spectrum, the Time-integrated model produces more power on large scales by 1-1.2 order of magnitude at fixed ionisation fraction, as to that of the Instantaneous model. Likewise, the Time-integrated model also produces slightly more power on small scales by a factor of 1.2-1.5 as compared with the Instantaneous EoR model. This difference is less than when comparing the ionisation field power spectra, which comes from the contribution of the density field to the 21cm power spectrum – small regions with high local density (high recombinations) remain neutral, and hence they do not contribute much to the small-scale fluctuations in 21cm power.
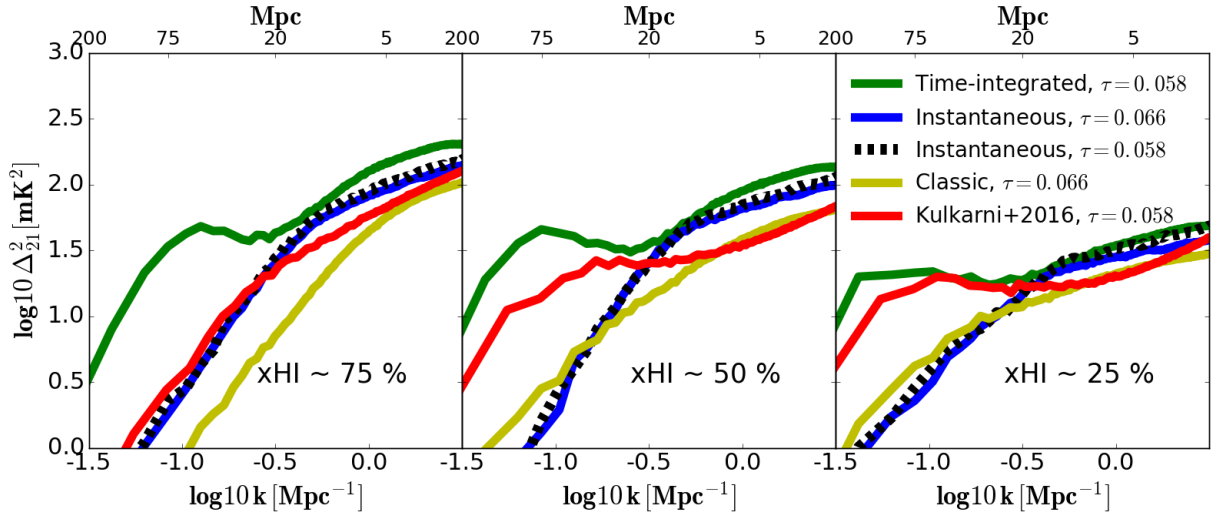
FIGURE 3.5: The 21cm power spectrum comparison between the Instantaneous (blue) and Time-integrated (green) models at different stages of reionisation ($x_{HI} \sim$ 25%, 50%, 75%). We compare our 21cm power spectra with the Very Late model (red) by similar semi-numerical method Kulkarni et al. (2016) that is calibrated to match Lyα and CMB data. Although our Time-integrated and Kulkarni et al. (2016) models correspond to different redshifts, but nevertheless the shape of the 21cm spectrum is similar, particularly at the intermediate and late stages of reionisations. We also show our **Classic** EoR model (yellow) introduced previously in chapter 2 which adopts the standard efficiency parameter approach similar to Kulkarni et al. (2016) model. Our Classic and Kulkarni et al. (2016) models produce similar power on small scales. The Instantaneous model, whether it is tuned to Planck (2016) τ (black dashed) or Planck (2015) τ (solid blue), always produces the exact 21cm power spectrum at fixed neutral fractions, regardless of the density field contribution from different redshifts. Models are tuned to the two recent *Planck* optical depth values as quoted in the legend.

We also compare our 21cm power spectra to a similar semi-numerical model by Kulkarni et al. (2016) that has been calibrated with Lyα and CMB data. The semi-numerical models by Kulkarni et al. (2016) adopts the standard efficiency parameter (ζ) approach similar to our **Classic** EoR model (yellow in fig 3.5) from that has previously been introduced in chapter 2. We choose to compare with the Very Late model in Kulkarni et al. (2016) (red in fig 3.5) that is tuned to match the Planck (2016) optical depth, consistent with the optical depth produced by our Time-integrated model. The ionisation histories of Kulkarni et al. (2016) and our Time-integrated model are very different even though they obtain $\sim 50\%$ neutral fraction at the same redshift. For instance, our Time-integrated model produces $x_{HI} = 0.77, 0.57, 0.25$ at z=8.25, 8.0, 7.75 whereas Kulkarni et al. (2016) model finds $x_{HI} = 0.84, 0.59, 0.42$ at z=10.0, 8.0, 7.0. Regardless of this difference in these models' reionisation histories, their 21cm power spectra are generally similar. We find that both models produce a similar shape of the 21cm power spectrum particularly

during the intermediate and final stages of reionisation. The minor difference in their amplitudes is due to using our R_{ion}-R_{rec} versus the standard ζ approach. This can be clearly seen when comparing our **Classic** EoR model with Kulkarni et al. (2016) model in figure 3.5. We see both models produce the same power on small scales while their difference on large scales might be from the difference in the density field and neutral fractions (although the density field has a minimal effect; see comparison between the Instantaneous model at different τ values). This confirms our previous findings that using the non-linear ionisation power, via our R_{ion}-R_{rec} approach, boosts the 21cm power spectrum as compared to models adopting the standard efficiency parameter method (**Classic** and Kulkarni et al. (2016) models).

This shows that our Time-integrated model, that is calibrated to match various EoR key observables, produces similar 21cm power spectrum as obtained by other semi-numerical models that have been calibrated to match Lyα and CMB data. The future 21cm observations might be able to discriminate between these models' power spectra.

In summary, we have compared the Instantaneous and Time-integrated models in terms of their EoR history, topology, and their 21cm power spectra. We have found that the Time-integrated model produces large HI bubbles while the Instantaneous model produces more small HI bubbles. The Time-integrated model yields a large scale 21cm/Ionization power spectrum that is higher by 1 order of magnitude as compared with the Instantaneous model. We have seen that the ionisation condition (equation 3.5) results in large H$\,$II bubbles which boost the amount of power on large scales. The comparison presented here aims to summarize the differences found between our new (Time-integrated) and previous (Instantaneous) models. However, previous works by Zahn et al. (2011) and Majumdar et al. (2014) have shown that semi-numerical simulations agree with radiative transfer simulations in terms of their ionization fields and 21cm power spectra. We leave for future work whether this new model matches radiative transfer simulations.

3.4 Model assumption effects on the 21cm power spectrum

The large differences in the 21cm power spectrum (figure 3.5) between the Instantaneous and Time-integrated models show that the 21cm power spectrum is highly sensitive to the physical assumptions used. There are two main differences between these models: First, the ionisation condition now accounts for the number of hydrogen atoms, and second, the recombination is now done accounting for partial ionisation. We believe our new model is more physically-motivated and realistic, but we would like to understand exactly how these changes individually impact the 21cm power spectra.

We therefore consider the various possible combinations between $R_{\rm rec}$ and $N_{\rm H}$ to create several models with different ionisation condition. We also consider models neglecting recombination altogether to analyse the impact of recombinations as we did previously in chapter 2, only with our new Time-integrated model.

More specifically, we keep the LHS of equation (3.5) ($R_{\rm ion}$ term) same and vary the integrand of RHS integrals, namely $\mathbb{R}_{\rm rec,V}$ and $N_{\rm HI,V}$, to create the following models:

- Full-NH-Full-Rrec (**FNH-FRrec**): $R_{\rm rec} + N_{\rm H}$.

- Full-NH-Partial-Rrec (**FNH-PRrec**): $x_{\rm HII}\, R_{\rm rec} + N_{\rm H}$.

- Full-NH-No-Rrec (**FNH-NRrec**): $N_{\rm H}$.

- Partial-NH-Full-Rrec (**PNH-FRrec**): $R_{\rm rec} + (1 - x_{\rm HII})\, N_{\rm H}$.

- Partial-NH-Partial-Rrec (**PNH-PRrec**): $x_{\rm HII}\, R_{\rm rec} + (1 - x_{\rm HII})\, N_{\rm H}$.

- Partial-NH-No-Rrec (**PNH-NRrec**): $(1 - x_{\rm HII})\, N_{\rm H}$.

- No-NH-Full-Rrec (**NNH-FRrec**): $R_{\rm rec}$.

- No-NH-Partial-Rrec (**NNH-PRrec**): $x_{\rm HII}\, R_{\rm rec}$.

The Time-integrated model is represented here by ionisation condition of **PNH-PRrec** whereas the Instantaneous model uses that of **NNH-FRrec**. The others are variants on these as summarized in Table 4.1. To illustrate the differences

Model Class	Recombination	Neutral Hydrogen
Full-NH-Full-Rrec (FNH-FRrec)	R_{rec}	N_H
Full-NH-Partial-Rrec (FNH-PRrec)	$x_{HII} R_{rec}$	N_H
Full-NH-No-Rrec (FNH-NRrec)	0	N_H
Partial-NH-Full-Rrec (PNH-FRrec)	R_{rec}	$(1 - x_{HII}) N_H$
Partial-NH-Partial-Rrec (PNH-PRrec)	$x_{HII} R_{rec}$	$(1 - x_{HII}) N_H$
Partial-NH-No-Rrec (PNH-NRrec)	0	$(1 - x_{HII}) N_H$
No-NH-Full-Rrec (NNH-FRrec)	R_{rec}	0
No-NH-Partial-Rrec (NNH-PRrec)	$x_{HII} R_{rec}$	0

TABLE 3.1: Summary of models considered in section 3.4 for the 21cm power spectrum comparison in figure 3.6 from different physical assumptions and treatment to the integrands of RHS integrals in the time-integrated ionisation condition, equation (3.5).

in the 21cm power spectrum, we use the same density field and halo catalogues generated within a simulation run of a box size 75 Mpc and $N = 140^3$. We have shown previously (Figure 2.8 in chapter 2) that the numerical volume convergence of our simulated 21cm power spectrum is excellent at all redshifts down to a box size of 75 Mpc, hence, we expect the same 21cm power spectrum for larger simulation volumes. The reionisation history produced by these models vary, so as before we choose to make our 21cm power spectrum comparison at a fixed neutral fraction.

Figure 3.6 shows the 21cm power spectrum produced by different models at 50% neutral fraction as explained above. First, we see that all these variants result in virtually the same 21cm power spectrum on small scales. This reiterates our previous finding in chapter 2 that using a non-linear ionisation rate R_{ion} boosts the 21cm power spectrum by a similar amount regardless of whether one accounts for recombinations or not, and further shows that accounting for the neutral hydrogen atoms does not alter this conclusion.

More significant differences are evident at large scales for the 21cm power spectrum. Models starting with full N_H (**FNH-**) produce 21cm power spectra with the same shape and amplitude on all scales (i.e. all the blue lines overlap), and likewise for models with partial or no N_H (**PNH-** and **NNH-**). This demonstrates that recombinations are subdominant for determining the large-scale 21cm power spectrum. It is clear that the **NH** term plays a major role in boosting/suppressing the large scale 21cm power spectrum. This means that semi-numerical models must carefully account for the local number density of neutral hydrogen for a proper prediction of the expected signal.
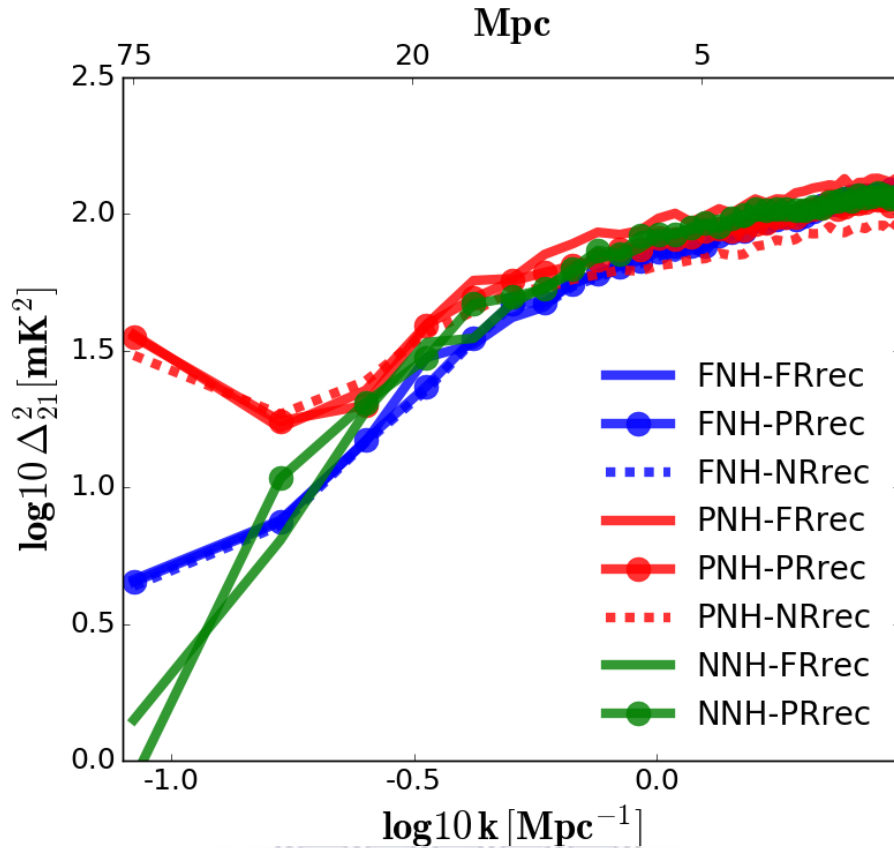
FIGURE 3.6: The 21cm power spectrum comparison for different physical assumptions at $x_{HI} \sim 50\%$. Different colors represent different ways to treat the local fluctuations in the neutral hydrogen density while different line styles corresponds to different recombinations terms, as explained by the legend and text. It is evident that the recombinations are subdominant in determining the large scale 21cm power spectrum. It is also shown models (red), that track the neutral fraction from partially ionised regions, yield a very high 21cm power spectrum on large scales.

From figure 3.6, we see the clear trend that models that do not account for the existing neutral hydrogen atoms (**NNH-** models such as the Instantaneous model) have lower 21cm power spectrum on large scales. Furthermore, models that use the total number of hydrogen atoms (**FNH-** models) at each time-step regardless of the ionisation fraction show 21cm power spectra that are slightly higher on large scales as compared to **NNH-** models. This is due to the presence of weak HI fluctuations by following only the density field ($\mathbf{N_{HI} \sim \Delta}$). However, models, that use the ionisation history of cells to track the neutral hydrogen atoms from partially ionised regions (**PNH-** models such as the Time-integrated model), show a very high 21cm power spectrum on large scales as opposed to the **NNH-** and **FNH-** models. This comes from the fact that the the **PNH-** models account for strong HI fluctuations by following the density field ($\mathbf{N_{HI} \sim \Delta}$) and ionisation field ($\mathbf{N_{HI} \sim x_{HII}}$) both. This shows that, at given neutral fraction, the large

scale 21cm power spectrum is highly influenced by the way in which we account for the fluctuations in the local neutral hydrogen density.

In the next section, we will discuss the calibration of the Time-integrated model against various EoR key observables and test how well the ongoing/upcoming 21cm observations will further constraints our free parameters.

3.5   Model calibration

We now focus on our favoured Time-integrated reionisation model, which includes all our new physics implementations. Previously, the parametrization of $R_{\rm ion}$ (equation 3.2) was obtained from our small-volume high-resolution radiative transfer hydrodynamic simulation (6/256-RT). However, the small volume of this simulation makes it subject to uncertainties since, as we saw in Figure 3.1, the ionisation history of this simulation is significantly delayed by its small volume. Here, we adopt a more general form for $R_{\rm ion}$, and determine whether existing EoR measurements can calibrate our source model, and thereby provide constraints on the nature of reionising sources.

To this end, we here consider a more generalized model with the following three free parameters:

- $f_{\rm esc}$ is the volume-averaged photon escape fraction.

- $A_{\rm ion}$ is the ionising emissivity amplitude, which scales the amount of ionising emissivity ($R_{\rm ion}$) equally across the halo mass range at a given redshift.

- $C_{\rm ion}$ is ionising emissivity-halo mass power dependence, which quantifies the $R_{\rm ion}$-M_h slope.

We will constrain these three parameters against various EoR observations and compare with the values found from fitting to the 6/256-RT simulation, using a Bayesian MCMC approach. We choose these parameters to explore since they are most closely related to the emission characteristics of the source population. We ignore $B_{\rm ion}$ which is related to how photoionisation suppresses low-mass galaxy growth, and $D_{\rm ion}$ because it is not physically obvious why ionisation rate of a given halo should have a strong redshift dependence. While it would be better to simply

let all these parameters vary, even doing an MCMC over this 3-D space is already computationally challenging since it requires doing full runs for each sampling, and increasing the dimensionality quickly makes the computational requirements intractable.

Recall that the Time-integrated model identifies the ionised regions using a time dependent ionisation condition (equation 3.5), that tracks the exact recombinations and neutral hydrogen atoms by following the reionisation history. The reionisation history, in this model, is numerically well converged for $\Delta z \leq 0.125$. With these requirements, the model becomes more computationally expensive to run, but nevertheless, is feasible for independent large volume runs. However, sampling the full MCMC space requires at least $\sim 10^6$ simulation realizations, which becomes infeasible. Hence we precompute a grid of models spanning the full prior space, and then do a trilinear interpolation to obtain the observables for any given parameter combination. This sacrifices some accuracy but makes the computation feasible.

We note that Greig & Mesinger (2015) developed an analysis pipeline, 21CMMC, that directly links their semi-numerical model 21CMFAST (Mesinger et al., 2011) to a Bayesian routine COSMOHAMMAR (Akeret et al., 2013) to constraining their free parameters. However, their ionisation condition did not include recombinations through the time integral method which they developed in Sobacchi & Mesinger (2014), and instead used a standard efficiency parameter (ζ) approach. Along with lower resolution of ~ 2 Mpc, these simplifications enabled them to run their semi-numerical model fully within an MCMC scheme.

3.5.1 Parameter estimations pipeline

We choose a cell size of 0.375 h^{-1} Mpc and a box size $L = 75$ Mpc, giving $N = 140$ cells per side. We precompute a grid of $25 \times 25 \times 25$ runs outputting the predicted observables for our models, uniformly sampling our selected prior range for our parameters of $(f_{\text{esc}}, \log 10(A_{\text{ion}}), C_{\text{ion}}) = [(0,1),(37,44),(-1,2)]$. This gives a total of 15,625 simulation independent realizations, which we interpolate inside the MCMC search process.

We have tested our parameter constraints using two different Bayesian inference tools MULTINEST (Feroz et al. , 2009) and EMCEE (Foreman-Mackey et al., 2013).

We have found the same parameter estimates using these two different codes, and hence, our presented parameters estimation here appears to be robust to variations in the algorithm used.

We here present the results obtained by using the EMCEE python package. We use 100 random walkers initialised around the maximum likelihood. For each walker, we sample 10,000 chains from the likelihood after 500 initial burn-in chains to achieve convergence. This makes a total of 1,000,000 samples which is sufficient to explore the whole parameter space.

3.5.2 EoR key observables constraints

We constrain our three free parameters to the following observations:

1. The dust-corrected star formation rate density integrated down to $M_{AB} = -17$ by Bouwens et al. (2015) at the following redshifts:

   - $z \sim 6$: log10(SFR) $[M_\odot \ Mpc^{-3} \ yr^{-1}]$ = -1.55 $\pm$ 0.06.
   - $z \sim 7$: log10(SFR) $[M_\odot \ Mpc^{-3} \ yr^{-1}]$ = -1.69 $\pm$ 0.06.
   - $z \sim 8$: log10(SFR) $[M_\odot \ Mpc^{-3} \ yr^{-1}]$ = -2.08 $\pm$ 0.07.

2. The Planck (2016) integrated optical depth to Thomson scattering: $\tau = 0.058 \pm 0.012$.

3. The Becker & Bolton (2013) ionising emissivity density measurements from Lyα data at $z = 4.75$: $\dot{N}_{ion}$ $[10^{51}$ photons s^{-1} Mpc$^{-3}]$ $= -0.014^{+0.454}_{-0.355}$.

We will first examine how our free parameters are constrained individually by each observation, and then we will examine the combined constraints.

3.5.2.1 The Bouwens et al. (2015) SFR constraints

Unlike other semi-numerical models that rely on the efficiency parameter ζ, our model allows a direct comparison to the SFR measurements by using a parameterisation for R_{ion} that is directly relatable to SFR. For a consistent comparison with Bouwens et al. (2015) measurements, we convert the R_{ion} back to SFR using Equation (2) in Finlator et al. (2011) that is based on Schaerer (2003) models, and
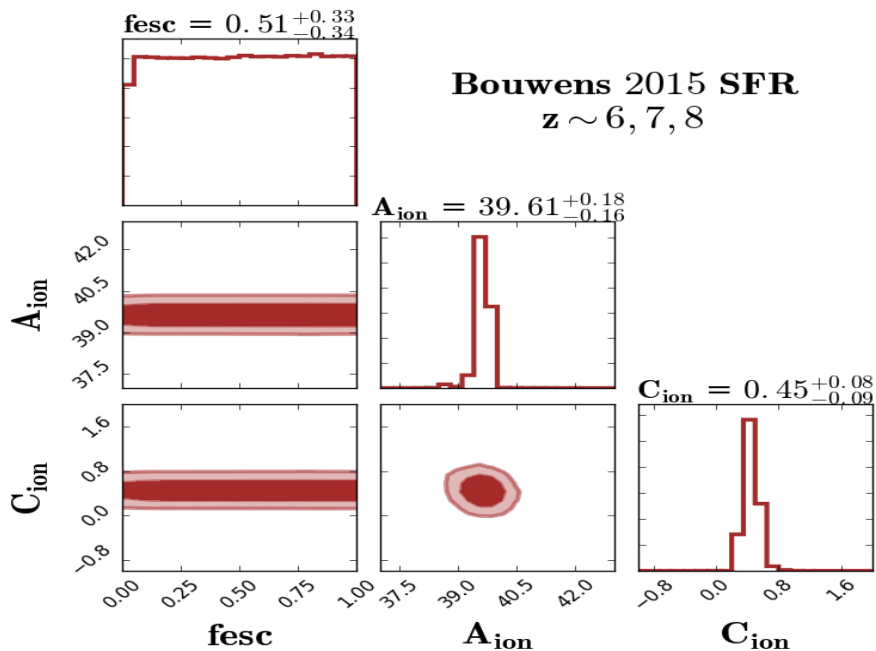
FIGURE 3.7: Bouwens et al. (2015) SFR observations, at z=6,7,8 combined together, constraints on our model parameters. Values on top of the 1-D PDFs diagonal represent the best fit parameters with 1-σ (14th and 84th percentiles). Dark and light shaded regions correspond to 1-σ and 2-σ levels respectively. The Bouwens et al. (2015) SFR observations provide tight constraints on the $A_{\rm ion}$ and $C_{\rm ion}$ in the selected prior range. As expected, the SFR measurements don't constrain the $f_{\rm esc}$.

add up all SFR from halos brighter than $M_{\rm AB} = -17$ at $z = 6, 7, 8$. To compute the corresponding $M_{\rm AB}$, we use the linear relation provided in Kennicutt (1998) which converts the SFR to luminosity L_ν over the wavelength range 1500-2800 Å.

Figure 3.7 shows the posterior distribution of our parameters as constrained solely by Bouwens et al. (2015) integrated SFR observations at z=6,7,8 (taken together). This provides somewhat tigher constraints than fitting to a single redshift of SFR measurement, although constraining to a single redshift yields similar results, which indicates that the weak redshift evolution in the SFR measurements is adequately reproduced by our model for $R_{\rm ion}$.

The Bouwens et al. (2015) SFR observations provides tight constraints on the $A_{\rm ion}$ and $C_{\rm ion}$ as seen in figure 3.7. while poorly constraining $f_{\rm esc}$. The latter is expected because the $f_{\rm esc}$ is set by the recombinations in the ISM while the SFR depends on the halo mass and redshift.

The value of $C_{\rm ion} = 0.45$ agrees within the 1-σ level with what was previously found from fitting our hydrodynamical simulations, which yielded $C_{\rm ion} = 0.41$ as

quoted in the previous chapter. This means that our large volume semi-numerical model is compatible with the same slope of the R_{ion}-M_h relation predicted by the small volume 6/256-RT simulation to match the Bouwens et al. (2015) SFR observation, thereby nicely corroborating the direct simulation results.

However, the differences are more significant in the A_{ion} posterior distribution. We see that the A_{ion} best-fit value of $10^{40.03}$ predicted by 6/256-RT simulation over-estimates by $\sim 50\%$ the value of $A_{\mathrm{ion}} = 10^{39.61}$ favoured by our SIMFAST21 MCMC fit using only the Bouwens et al. (2015) SFR constraints. This represents somewhat poor concordance at only a 3-σ level. This discrepancy arises due to the small box size $(=6\mathrm{h}^{-1}\mathrm{Mpc})$ of 6/256-RT simulation that does not capture the large scale fluctuations and massive dark matter halos that contribute significantly to the reionisation photon budget. Hence, the 6/256-RT simulation requires larger A_{ion} to compensate for these limitations. This effect is also seen in figure 3.1 when comparing the reionisation histories of the 6/256-RT simulation with our large volume semi-numerical simulations which tend to reionise the universe much earlier at a fixed optical depth due to the presence of those massive halos and large scale-fluctuations.

Overall, utilising only the integrated SFR observations already gives interesting constraints on the slope and amplitude of the ionising photon output as a function of halo mass. However, there are no useful constraints on the escape fraction.

3.5.2.2 The Planck (2016) optical depth constraints

Figure 3.8 shows the parameters constrained to match solely the Planck (2016) data. This shows that the Thomson optical depth data alone provides fairly poor constraints on any of the parameters. There is a slight tendency to favour lower f_{esc} values, as also found by Greig & Mesinger (2016, see their Figure 4), but in general all values from zero to one are still allowed.

The main reason for the lack of sensitivity to f_{esc} is shown in Figure 3.9, and essentially arises from the still-large errors on τ. Figure 3.9 shows the volume-weighted global neutral fraction evolution for fixed values of A_{ion} and C_{ion}, and shows that $f_{\mathrm{esc}} = 20 \to 80\%$ gives rise to $\tau = 0.058 \to 0.071$, which is still essentially within the 1σ uncertainty on the measurement of $\tau = 0.058 \pm 0.012$.
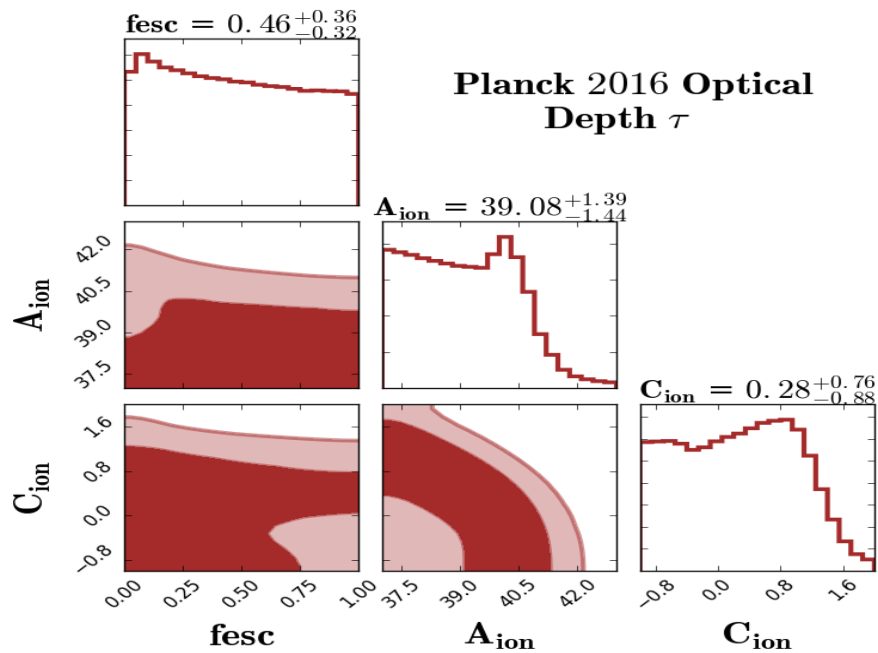
FIGURE 3.8: Planck (2016) optical depth constraints on our model parameters. Values on top of the 1-D PDFs diagonal represent the best fit parameters with 1-σ (14th and 84th percentiles). Dark and light shaded regions correspond to 1-σ and 2-σ levels respectively. The Planck (2016) τ provides poor constraints on all parameters while there is slight tendency towards lower $f_{\rm esc}$ values. The Planck (2016) τ prefers models with low $A_{\rm ion}$ and $C_{\rm ion}$ values for the chosen prior range as compared to values implied by the Bouwens et al. (2015) SFR observations.

Hence much smaller error bars on τ are required to provide better constraints on $f_{\rm esc}$.

$A_{\rm ion}$ and $C_{\rm ion}$ are also not well constrained by the Thomson optical depth data alone, though there is some tendency to favour small values of $A_{\rm ion}$ and $C_{\rm ion}$. Nonetheless, the uncertainties are large, and the values favoured from the SFR constraints alone are within the 1σ uncertainties of these predictions, as are the values found directly from the hydrodynamic simulations.

In summary, the Thomson optical depth as measured by *Planck* alone does not provide strong constraints on any of our parameters, since the optical depth might not provide more accurate constraints on the end of reionization than the Ly-α observations which directly measure the amount of neutral fraction. It is clear that reducing uncertainties and/or including other data will be required in order to meaningfully constrain the sources driving reionisation.
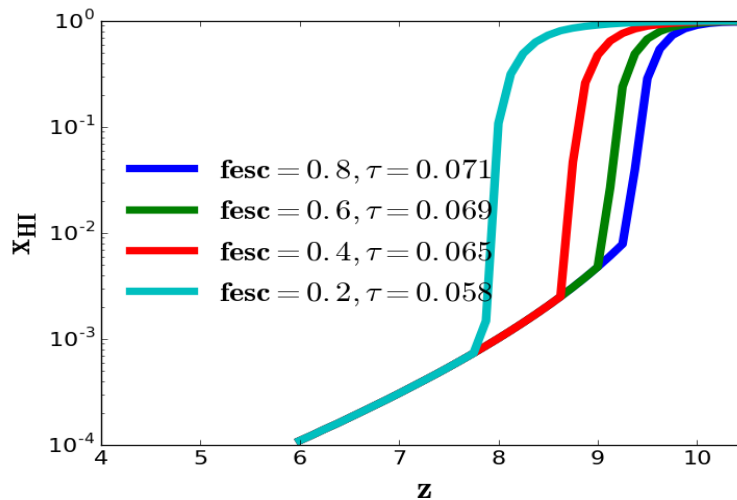
FIGURE 3.9: The reionisation history for our Time-integrated model with different $f_{\rm esc}$ values while fixing the $A_{\rm ion}$ and $C_{\rm ion}$ to values implied by the recent Planck (2016) τ measurements. This clearly shows that the current Planck (2016) optical depth $\tau = 0.058 \pm 0.012$ does not provide tight $f_{\rm esc}$ constraints for models with rapid reionisation scenarios as the case with our Time-integrated EoR model.

3.5.2.3 The Becker & Bolton (2013) ionising emissivity constraints

The integrated emissivity of ionising photons $\dot{\rm N}_{\rm ion}$ quantifies the total ionisation rate density from all ionising sources that escape galaxies to fill the intergalactic medium. Mathematically, $\dot{\rm N}_{\rm ion} = \sum f_{\rm esc} R_{\rm ion}$ divided by the simulation's comoving volume. To compare with Becker & Bolton (2013) $\dot{\rm N}$ion measurements, we add up $f_{\rm esc} R_{\rm ion}$ from all halos and divide by the simulation comoving volume at z=4.75. As with the SFR data, our model permits a direct comparison with the $\dot{\rm N}$ion data since we use a parameterisation for $R_{\rm ion}$ rather than a single efficiency parameter.

Figure 3.10 shows the posteriors for our three free parameters constrained only to match the Becker & Bolton (2013) $\dot{\rm N}$ion data. As with the SFR and τ constraints, the $f_{\rm esc}$ is unconstrained by this data. Similar to Planck (2016) τ constraints, we find that models with high $A_{\rm ion}$ and $C_{\rm ion}$ values are disfavored by Becker & Bolton (2013) $\dot{\rm N}$ion measurements, but again this is within 1σ of the SFR-only constraints.

The slight tendency of $\dot{\rm N}$ion data towards negative values of $C_{\rm ion}$ (negative slope of $R_{\rm ion}$-M_h relation) favours small halos being the dominant ionising photon sources contributor to match the post-reionisation measurements. In contrast, SFR and τ data prefers the positive side of $C_{\rm ion}$ values, implying that massive halos are more important during the reionisation. This shows that reionisation requires more ionising photons while matching post-reionisation data requires fewer ionising
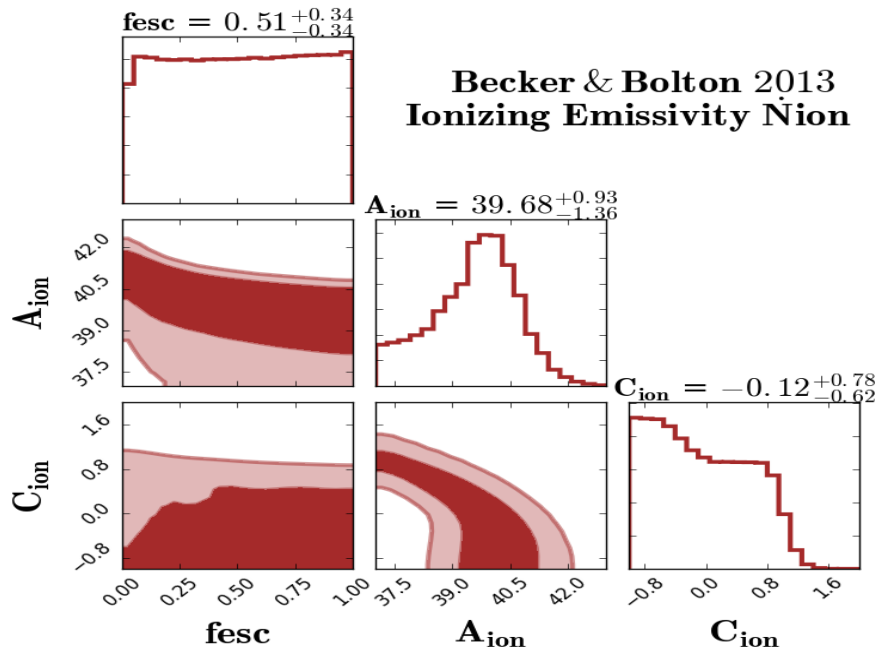
FIGURE 3.10: The Becker & Bolton (2013) ionising emissivity (z=4.75) constraints on our model parameters. Values on top of the 1-D PDFs diagonal represent the best fit parameters with 1-σ (14th and 84th percentiles). Dark and light shaded regions correspond to 1-σ and 2-σ levels respectively. Similar to previous constraints, the f_{esc} is poorly constrained and similar to τ constraints, the data prefers lower f_{esc} values. The $\dot{\mathrm{N}}$ion data also prefers models with negative C_{ion} in our selected prior range. This shows that matching to post-reionisation data requires fewer ionising photons and prefers models with dominant contributions from small dark matter halos.

photons. This stands as one of the theoretical challenges for the EoR models as it is not easy to match simultaneously observational constraints during and after reionisations. $\dot{\mathrm{N}}$ion measurements at higher redshifts ($z \sim 6, 7$) would be very useful to see if this tension extends into the overlapping redshift regime (Keating et al., 2014).

3.5.2.4 Combined SFR + τ + $\dot{\mathrm{N}}$ion constraints

To obtain the strongest constraints given the observations we consider, we now combine our three key EoR constraints: the Bouwens et al. (2015) SFR observations, Planck (2016) optical depth measurements and the Becker & Bolton (2013) $\dot{\mathrm{N}}$ion data. This represents the best available constraints we can make given current data, and serves to provide our base model from which we will do forecasting for 21cm experiments.

EoR Constraint	f_{esc}	$\log10(A_{ion})$	C_{ion}
Bouwens et al. (2015) SFR all at z=8,7,6	$0.51^{+0.33}_{-0.34}$	$39.61^{+0.18}_{-0.16}$	$0.45^{+0.08}_{-0.09}$
Planck (2016) optical depth τ	$0.46^{+0.36}_{-0.32}$	$39.08^{+1.39}_{-1.44}$	$0.28^{+0.76}_{-0.88}$
Becker & Bolton (2013) N_{ion} at z=4.75	$0.51^{+0.34}_{-0.34}$	$39.68^{+0.93}_{-1.36}$	$-0.12^{+0.78}_{-0.62}$
ALL = SFR+τ+N_{ion}	$0.25^{+0.26}_{-0.13}$	$39.62^{+0.17}_{-0.18}$	$0.44^{+0.09}_{-0.09}$
Values obtained from fitting to 6/256-RT	-	40.03	0.41

TABLE 3.2: Summary of our parameter estimations from individual and combined set of observations, as well as from matching to the 6/256-RT simulations.

Figure 3.11 shows the parameter estimates as fit to the combined sample of these EoR observations. We see that the A_{ion} and C_{ion} are tightly constrained, which as Figure 3.7 showed is driven by the Bouwens et al. (2015) SFR constraints, as the other observations did not provide very tight constraints on these parameters.

The more interesting difference is in f_{esc}, where the combined constraints now definitely prefers lower f_{esc} values, with best fit-value of $0.25^{+0.26}_{-0.13}$. This is still a rather wide range, and the posterior ellipses show that even very low escape fractions are not ruled out at more than a $\sim 1\sigma$ level, and very high f_{esc} values are only disfavoured at $\lesssim 2\sigma$. This tendency was hinted at from matching to Becker & Bolton (2013) N_{ion} and Planck (2016) optical depth individually. This result indicates that our previous findings of $f_{esc} = 0.04 - 0.06$ in chapter 2 is clearly possible for models with higher A_{ion} and C_{ion} values within their derived 1-σ level. A summary of the individual and combined constraints is provided in Table 3.2.

This shows that current observations can already constrain the basic power law parameters of the ionising photon output versus halo mass, but constraints on f_{esc} are still somewhat elusive. Note that we are also assuming a constant f_{esc} for all galaxies, while there may be some mass and/or redshift dependence; however, with even a single parameter already being poorly constrained, it is unlikely that adding more parameters will allow tighter constraints.

3.6 21cm forecasting and experiments sensitivities

The ultimate goal is to add the 21cm observations to these existing data (or future improved versions thereof), in order to ascertain how well we can understand the sources of reionisation. To do so, we adopt a forecasting approach by which we
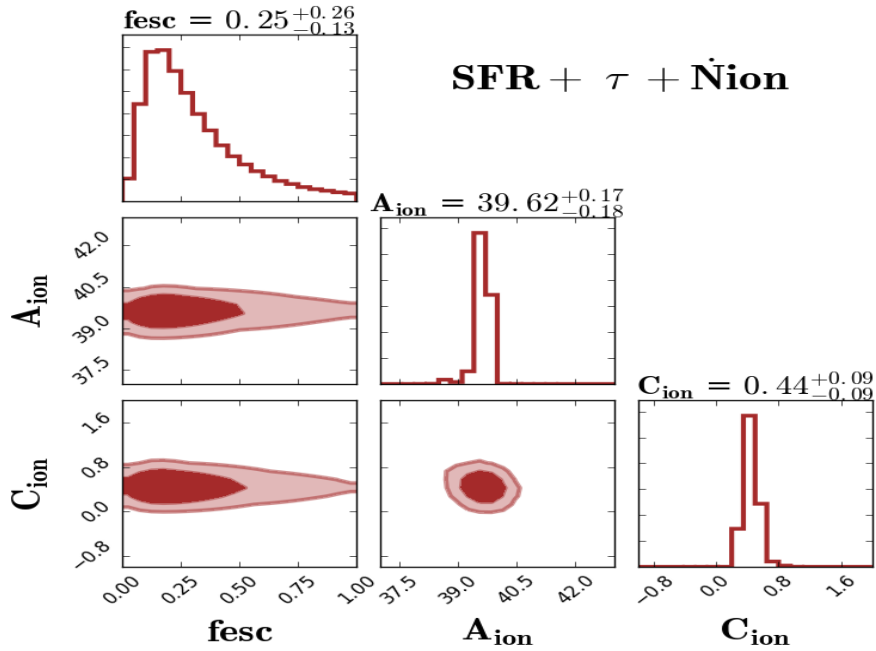
FIGURE 3.11: Combined constraints from SFR, τ and $\dot{N}$ion. Values on top of the 1-D PDFs diagonal represent the best fit parameters with 1-σ (14th and 84th percentiles). Dark and light shaded regions correspond to 1-σ and 2-σ levels respectively. Combining all these observations results in a tighter $f_{\rm esc}$ constraints while $A_{\rm ion}$ and $C_{\rm ion}$ still follow Bouwens et al. (2015) SFR constraints.

use expected uncertainties from future 21cm power spectrum measurements in concert with these existing data and ascertain how much improvement the 21cm data will provide in the precision with which our parameters are constrained. We will assume a base model that is the best-fit to our current constraints as listed in Table 3.2.

We focus our analysis on LOFAR, HERA, and SKA1-Low. For each experiment, we first compute the thermal noise power spectrum which dominates the errors in measuring the 21cm signal. We then add more uncertainties from the sample variance, while neglecting the shot noise since it has been shown to have a minimal effect at the relevant scales ($k < 2h{\rm Mpc}^{-1}$) for these telescopes sensitivities (Pober et al., 2013). We obtain these uncertainties using the 21cmSENSE package[5], and refer to Parsons et al. (2012) for the full mathematical derivation of the radio interferometer sensitivities, and to Pober et al. (2013, 2014) for more details on observation strategies and foreground removal models. We briefly highlight the basic equations and concepts used in 21cmSENSE to obtain the 21cm power spectrum error from a specific array configuration.

---

[5]https://github.com/jpober/21cmSense

The dimensionless power spectrum of the thermal noise (Parsons et al., 2012; Pober et al., 2013, 2014) can be obtained using:

$$\Delta_N^2(k) \approx X^2 Y \frac{k^3}{2\pi^2} \frac{\Omega}{2t} T_{sys}^2 \,, \tag{3.7}$$

where X^2Y is a conversion factor from angle and frequency units to comoving cosmological distances, Ω is the primary beam field-of-view, t is the integration time and T_{sys} is the system temperature (sky+receiver). It is then straightforward to add the sample variance to the thermal noise to obtain the total error (Pober et al., 2013) as follows:

$$\delta\Delta^2(k) = \left(\sum \frac{1}{\left(\Delta_N^2(k) + \Delta_{21}^2(k)\right)^2} \right)^{-\frac{1}{2}} \,, \tag{3.8}$$

where Δ_{21}^2 is the 21cm power spectrum and the summation runs over all measured independent k-modes.

We construct these experiments as follows:

- **LOFAR**: We use the Netherlands 48 High-Band Antennas (HBA) with positions listed in van Haarlem et al. (2013) following Pober et al. (2014). Each antenna has a diameter of 30.75 m which results in a total collecting area of 35,762 m^2 for the 48 HBA station. The receiver temperature T_{rcvr} is set to 140,000 mK as suggested by Jensen et al. (2013); Greig & Mesinger (2015).

- **HERA**: We consider the final design of 331 hexagonally packed 14 m antennas (Ewall-Wice et al., 2016; Beardsley et al., 2015). With this configuration, the total collecting area becomes 50,953 m^2. We assume an 100,000 mK receiver temperature T_{rcvr}, similar to previous works by Pober et al. (2014); Greig & Mesinger (2015).

- **SKA-LOW1**: We model SKA1-Low following the SKA1 System Baseline Design document by Dewdney (2013) in which the proposed array consists of 911 antennae in total. These antennae are distributed randomly to form a compact core using 866 dishes surrounded by the remaining 45 dishes along spiral arms. The 866 core antennae provide the vast majority of the sensitivity, and hence our SKA model ignores those 45 spiral arms stations (Pober et al., 2014; Greig & Mesinger, 2015). Each station of 866 antennae has a

diameter of 35 m which makes a total collecting area of 833,189 m^2. The receiver noise here is determined by: T$_{rcvr}$ = 0.1 T$_{sky}$ + 40 K, where the sky temperature is modelled using: T$_{sky}$ = $60\lambda^{2.55}$.

For a consistent comparison, we choose to operate these three array designs in a drift-scanning mode for 6 observing hours per day for 180 days at 8 MHz bandwidth. We consider Pober et al. (2014) moderate foreground removal model where the foreground wedge extends 0.1 h Mpc^{-1} beyond horizon limit.

3.6.1   Including the 21cm data

We combine three different redshifts of 21cm power spectrum observations, namely $z = 9.0, 8.5, 8.0$, which provides tighter constraints than considering any single epoch observations. With multiple redshifts 21cm observations, one accounts simultaneously for the variation in redshift (density field) and neutral fraction (ionisation field) evolution, which are the main components in determining the 21cm fluctuations. Given the rapid reionisation behaviour of the Time-integrated model as shown in figure 3.1, our selected redshifts ($z = 9, 8.5, 8$) correspond to a wide range of neutral fractions that account for different reionisation epochs such as the initial bubble growth and the bubble overlap phase. We next construct the likelihood from these observations by simply adding up their individual χ^2. We limit our analysis to a wide k-range of 0.15-1.0 Mpc^{-1}, consistent with Greig & Mesinger (2015). From this k-range, we select 10 bins of the power spectrum which is sufficient to capture the fluctuations for a given 21cm power spectrum.

We use the well-calibrated Time-integrated model with parameters derived from fitting to our combined set of EoR observations as discussed in § 3.5.2.4 and shown in figure 3.11. Specifically, we use the following parameters: (f_{esc}, log10(A$_{ion}$), C$_{ion}$) = (0.24, 39.63, 0.43), consistent with the 1-σ level of constraints by our combined set of EoR observations. We then use these parameters to create our mock observations with a large box size of $L = 300$ Mpc and $N = 560$ per side which results in a resolution of 0.375 h^{-1} Mpc. We determine the error in measuring the 21cm power spectra for our mock observation by using the telescope sensitivity code 21cmSense for each specific array experiments at our chosen redshifts as described above. We use the same pipeline discussed in § 3.5.1 to sample the 21cm power spectrum space, except now we include the 21cm mock observation power
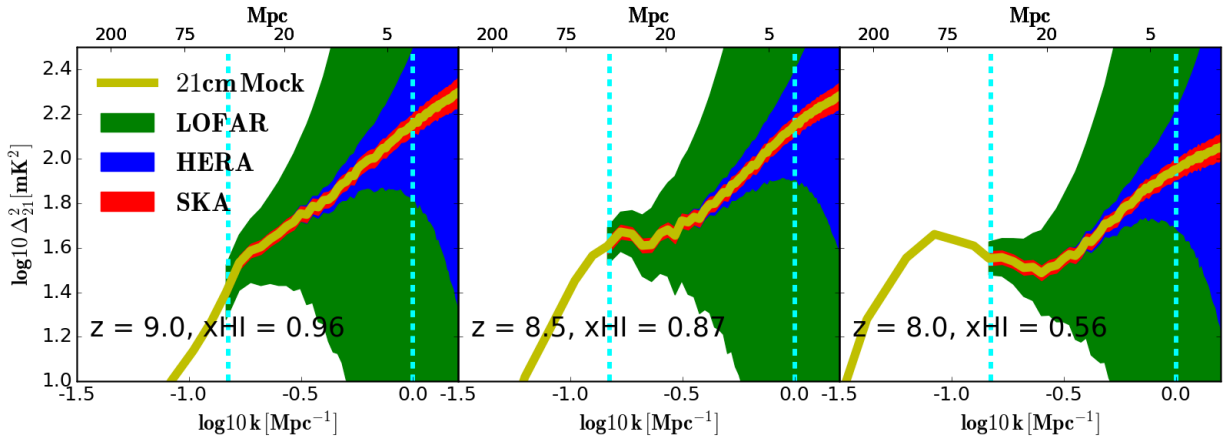
FIGURE 3.12: Three redshifts mock 21cm EoR observations using the well-calibrated Time-integrated EoR model with parameters (f_{esc}, $\log 10(A_{ion})$, C_{ion}) = (0.24, 39.63, 0.43). Yellow solid line represents the 21cm power spectrum from the Large box mock observation (L=300/N=560). Shaded area shows the erorrbars obtained using 21CM-SENSE package for our constructed EoR arrays: SKA (red), HERA (blue), LOFAR (green). Redshifts and neutral fractions for 21cm mock observations are quoted in each panel. Vertical cyan dashed lines show our chosen k-range to preform the 21cm MCMC.

spectra among the pre-computed runs to study how well the MCMC technique may recover the input model parameters.

Figure 3.12 shows our 21cm mock observations at several redshifts. The shaded area corresponds to the error in measuring the 21cm power spectrum for our large mock observations using the 21CMSENSE package. LOFAR (green shading), operating currently, will be able to constrain only the largest scales considered here, while HERA (blue), under construction now, will be further sensitive to intermediate scales, while the future SKA1-Low (red) will provide tight constraints into the sub-Mpc scale regime owing to its wider baselines and hence better resolution. These uncertainties depend mainly on our telescope configurations as described above. Hence the main improvement as these facilities develop will be to better constrain the 21cm power spectrum towards smaller scales, and each generation will provide significant gains in this.

3.6.2 21cm MCMC

We now ask how well the 21cm data can constrain our free parameters. First, we consider the 21cm power spectrum data as shown in Figure 3.13 by itself, to see how tightly our parameters can be constrained by such observations alone.
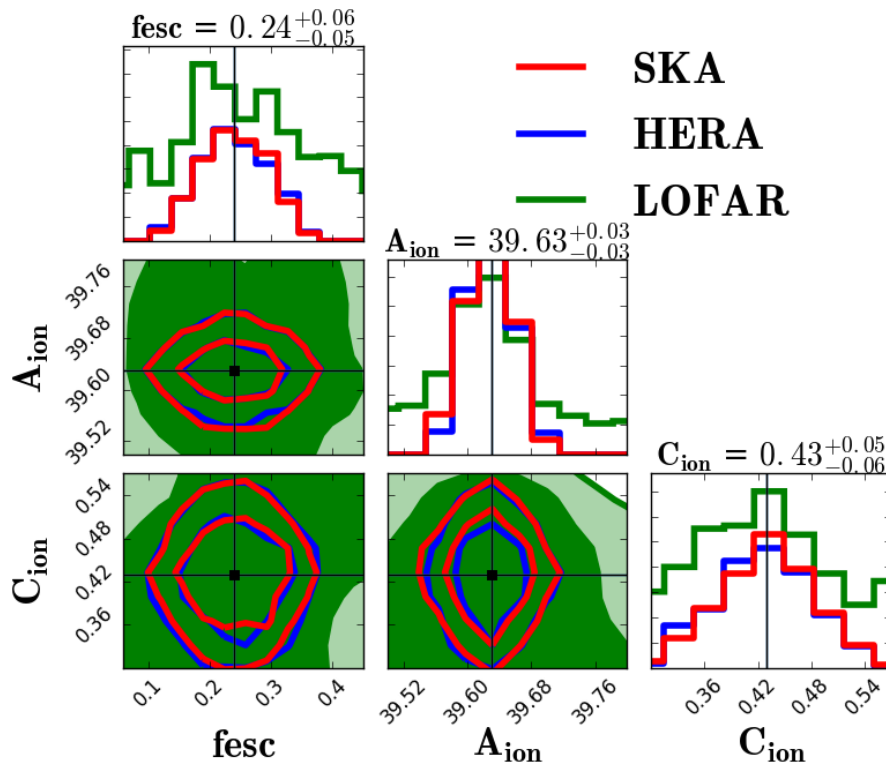
FIGURE 3.13: 21cm power spectrum constraints on our three EoR parameters from several redshifts (z=9.0,8.5,8.0) mock observations. SKA, HERA, and LOFAR constraints are shown by red, blue, and green contours respectively. Values on top of the 1D PDFs represent the best fit parameters as implied by the SKA mock observations while black square points correspond to the input mock observation parameters: $(f_{esc}, \log10(A_{ion}), C_{ion}) = (0.24, 39.63, 0.43)$. The MCMC technique is able to recover the input model parameters. It is evident that the future 21cm observations can tightly constrain our model parameters for experiments with small and intermediate levels of uncertainty in detecting the expected signal such as SKA and HERA respectively.

Then we add the 21cm data to our other existing observational constraints. In each case we use our MCMC framework to determine our best-fit values of our free parameters and their uncertainties using the entire data set, for the case of each telescope facility. This provides forecasting for how much improvement can be expected from future 21cm observations.

Figure 3.13 shows the 1D PDFs and 2D contours of our three parameters from the combined redshifts ($z = 9.0, 8.5, 8.0$) of 21cm mock observations by our three selected EoR experiments. To begin, we see that our MCMC search well recovers the best-fit input model (mock observation) parameters (black square points). This is to be expected, since this same input model was used to generate the 21cm

data. The improvement to be noted here is the reduction of the uncertainties on these parameters relative to the previous case without 21cm data.

For LOFAR (green shaded area), we see that the 21cm observations don't provide tight constraints due to large uncertainties as seen in figure 3.12. Essentially, mildly constraining the large-scale power provides little information on the ionisation sources that drive reionisation.

In contrast, HERA (blue) and SKA (red) provide quite tight constraints on the free parameters. Note that the scale of the posteriors is substantially reduced relative to our previous plots in order to enhance visibility. Hence future 21cm data alone can already independently constrain reionising sources, without adding in any other observations. Interestingly, there is almost no difference between the SKA and HERA constraints. This arises because the parameter constraints are predominantly driven by the larger scales, and HERA and SKA provide similar constraints on the power spectrum for scales $\gtrsim 2$ Mpc.

Comparing the 21cm constraints with constraints obtained from combining several EoR key observables, we find that constraining to 21cm observations yield smaller parameter errors. This can be clearly seen when comparing the 1-σ level of $f_{\rm esc}$ and $A_{\rm ion}$ found by constraining to the 21cm observations (fig 3.13) versus to the combined EoR sample (SFR, $\dot{N}_{\rm ion}$, τ) (fig 3.11). However, it is evident that the 21cm future observation can constrain the $f_{\rm esc}$ tighter than the current EoR key observables.

In previous work by Greig & Mesinger (2015), the authors used a similar semi-numerical framework and performed similar analysis to constrain their free parameters to future 21cm mock observations. However, they did not have the photon escape fraction as a free parameter and rather constrained their efficiency parameter ζ, from which the $f_{\rm esc}$ can be computed for various assumptions about gas fraction in stars and ionising photons number per baryons (see their eq. (2)). However, we here constrain the $f_{\rm esc}$ directly without making further assumptions about the gas and baryons fractions, hence our presented $f_{\rm esc}$ results are direct, albeit the inherent photon conservation issues in these semi-numerical models, which we will discuss later.

We finally constrain our free parameters by combining the 21cm mock observations with the current EoR key observables (SFR, $\dot{N}_{\rm ion}$, τ) as shown in figure 3.14. From this figure, we see that our three parameters are well-constrained by the combined
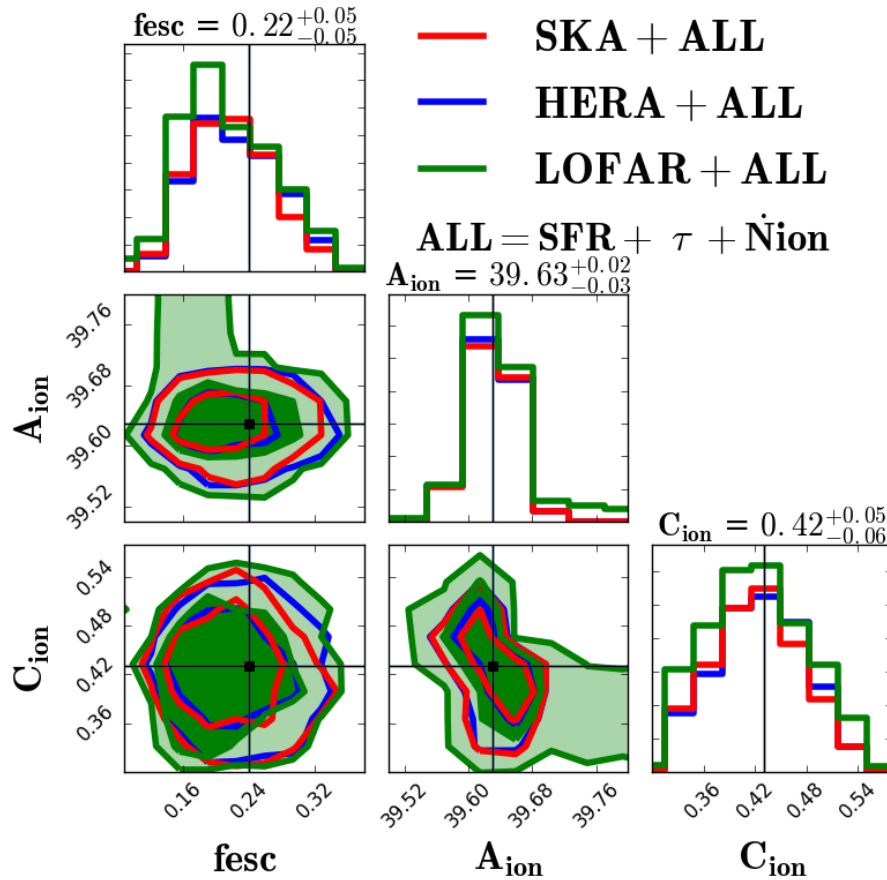
FIGURE 3.14: Parameter estimates from combining the current EoR observations with the 21cm mock observations. The current EoR observations here are our previous combined sample: SFR, τ and $\dot{N}$ion while the 21cm mock observations are combinations of several 21cm redshifts at z=9.0,8.5,8.0. SKA, HERA, and LOFAR constraints are shown by red, blue, and green contours respectively. Values on top of the 1D PDFs represent the best fit parameters as implied by the SKA mock observations while black square points correspond to the input mock observation parameters: $(f_{esc}, \log10(A_{ion}), C_{ion}) = (0.24, 39.63, 0.43)$. It is evident that adding the current EoR observations on top of the 21cm mock observations provide more tighter constraints even for experiments with large 21cm power uncertainties such as the case with LOFAR.

set of current EoR and 21cm mock observations. Adding our combined EoR sample (SFR, $\dot{N}_{ion}$, τ) on top of the 21cm mock observations improves the error in estimating our free parameters, particularly for arrays with large 21cm errorbars such as LOFAR. This shows that the future 21cm observations are important in constraining the model astrophysical parameters and complement the other existing EoR various observations. A summary of our 21cm mock observations constraints combined with the other EoR observations is given in table 3.3.

Our 21cm forecasting shows that the future 21cm power spectrum observations

	f_{esc}	$log10(A_{ion})$	C_{ion}
21cm Mock Observations			
SKA	$0.240^{+0.056}_{-0.054}$	$39.628^{+0.030}_{-0.032}$	$0.431^{+0.052}_{-0.056}$
HERA	$0.237^{+0.061}_{-0.054}$	$39.626^{+0.031}_{-0.025}$	$0.425^{+0.055}_{-0.058}$
LOFAR	$0.415^{+0.384}_{-0.239}$	$39.229^{+0.606}_{-1.117}$	$0.445^{+0.341}_{-0.274}$
21cm Mock Observations + ALL (SFR, $\dot{N}_{ion}$, τ)			
SKA+ALL	$0.217^{+0.052}_{-0.048}$	$39.631^{+0.024}_{-0.029}$	$0.423^{+0.053}_{-0.057}$
HERA+ALL	$0.221^{+0.058}_{-0.051}$	$39.630^{+0.029}_{-0.029}$	$0.427^{+0.053}_{-0.059}$
LOFAr+ALL	$0.206^{+0.069}_{-0.045}$	$39.634^{+0.042}_{-0.033}$	$0.421^{+0.065}_{-0.060}$

TABLE 3.3: Summary of our parameter estimations from the 21cm mock observations and from combining the 21cm mock observations with the current EoR observations (SFR, $\dot{N}_{ion}$, τ).

will be crucial for providing tight constraints on various parameters related to the sources of reionisation. Even by themselves, such data will provide improve constraints over what can be obtained using current observations. When combined with other observations, the constraints get quite tight, even for the difficult-to-constrain photon escape fractions f_{esc}. The tightness of the constraints suggest that it may be possible to independently constrain variations in the escape fraction with mass or redshift; we will examine this in future work.

3.6.3 Photon conservation

To make use of our f_{esc} constraints, we here test the photon conservation problem in our semi-numerical model. Previous semi-numerical models, based on the excursion set formalism, have pointed out a violation in the photon number conservation. In Zahn et al (2007), the authors found that their semi-numerical model loses about 20% photons. They have argued that this photon loss arises from ionised bubbles overlapping, which they compensated by boosting the efficiency parameter ζ. More recent work by Paranjape et al. (2016) have developed a Monte Carlo Model of bubble growth to resolve the photon conservation problem in their semi-numerical model. Although their bubble growth model didn't resolve the problem completely, nevertheless improvements have been achieved and they have demonstrated that the problem comes from the fact that the excursion set-based models use the average mass of the bubbles rather than tracking the actual mass of sources and bubble local density fluctuations.

However, there are two methods to flag the spherical regions as ionised in the excursion set-formalism. The first is to flag the whole cells in the bubble (whole

flagging) whereas the second is to flag only the center cell of the bubble (center flagging). We next use these two methods to verify the photon conservation in our Time-integrated EoR model. We would expect that, during time interval dt, the total number of escaped ionising photons ($f_{esc}R_{ion}\,dt$) minus the total number of recombinations ($R_{rec}\,dt$) should be equal to the number of ionisations in the neutral hydrogen atoms (($x_{HII}(t_{i+1}) - x_{HII}(t_i))N_H$). In other words, the successful photons that manage to escape from the interstellar medium (corrected by f_{esc}) and from high density regions along the way (subtracted by $R_{rec}\,dt$) should be equal to the total number of neutral atoms that have been ionised during time dt. We can write the photon conservation ratio as follows:

$$\text{Photon Conservation Ratio} = \frac{(x_{HII}(t_{i+1}) - x_{HII}(t_i))N_H}{(f_{esc}R_{ion} - R_{rec})\,dt}, \tag{3.9}$$

where $dt = t_{i+1} - t_i$. This ratio should be equal to unity for an ideal photon conserving model. However, the ratio can be less than unity when the universe is highly ionised. We then apply this ratio to the two methods, whole flagging versus center flagging, to check the photon conservation problem in both. We note that center flagging scheme requires about 20% more ionising photons to match the reionisation history obtained by whole flagging method. We then adjust the f_{esc} in two methods to reproduce identical reionisation history (identical τ) while keeping other parameters fixed.

In figure 3.15. we plot the photon conservation ratio for the two methods, whole flagging (green solid line) and center flagging (green dashed line) with the reionisation history (blue solid line). We find that the center flagging scheme under-uses photons during all reionisation redshifts, even after reionisation (z < 8), which might partly explain the need for higher f_{esc} with this method. The photon loss in the whole flagging scheme agrees qualitatively with center flagging at higher redshifts when the universe is almost neutral.

As reionisation proceeds, the whole flagging starts to over-use photons and ionises more neutral atoms than expected. The photon excess/loss in the two methods are clearly redshift dependent. In the center flagging method, the photon loss is by a factor of $\sim 3,7,20$ at z= 7.75, 9.25, 11 respectively. The whole flagging scheme shows photon loss (under-using photons) at high redshifts and photon excess (over-using photons) at the end of reionisation. At high redshifts, the photon loss, in the whole flagging, is by a factor of $\sim 2,4,7$ at z= 8.75,9,11 respectively. This
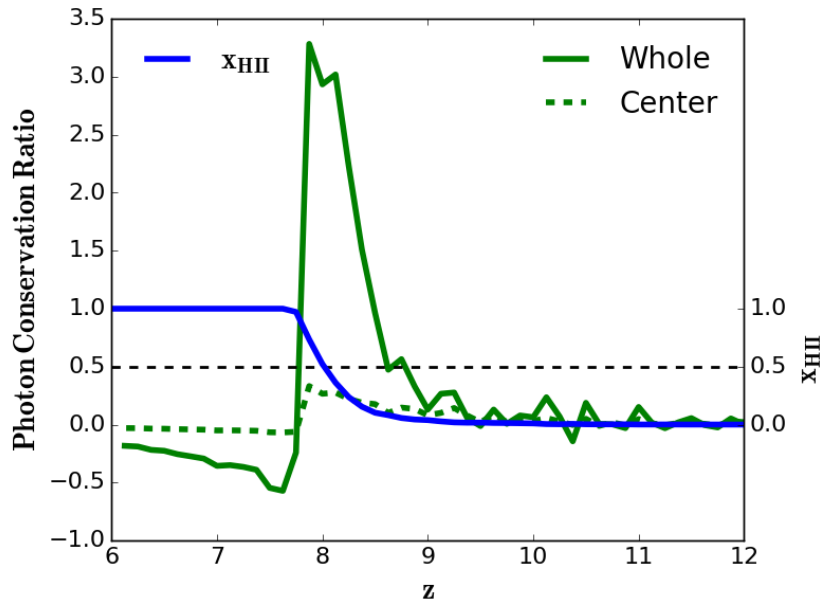
FIGURE 3.15: Photon conservation ratio from the Time-integrated EoR model using whole flagging (green solid) versus center flagging (greed dashed) scheme, with their reionisation history (blue solid). Horizontal black dashed line represents the 50% neutral/ionised fraction limit. Both methods violate the photons number conservations as seen by the under-ionisation at high redshifts and over-ionisation at end of reionisation.

shows that, at high redshifts, the photon loss, in the whole flagging method, is less by a factor of $\sim$ 2,3 as compared with center flagging method. At z=8.5 ($x_{HI} \sim$ 0.9), the whole flagging method satisfies the photon conservation condition as the ratio becomes unity, but the ratio does not converge at unity afterwards. After this point, the whole flagging scheme starts to overuse photons increasingly by a large amount till the end of reionisation. We find the photon excess is about 10% at z=8.4 and 70% at z=7.75 (end of reionisation).

We note that all our EoR models adopts the whole flagging method. This shows that our constrained photon escape fractions f_{esc} are, in fact, over-estimated by the photon excess associated with the whole flagging method. All our previous f_{esc} estimations can be corrected and lowered by 10% up to 70% depending on redshifts. The photon loss/excess evolution in redshift suggests that the f_{esc} might be required to change with redshift in order to preserve photon number conservation as a temporary solution.

3.7 Conclusion

We have improved our SimFast21 semi-numerical code for computing the EoR on large scales by incorporating a more physically-motivated criterion for determining whether a region of space is ionised, as well as integrating our framework into a full MCMC parameter search framework so we can forecast how well current and future observations can constrain the physical properties of the sources driving reionisation.

We have calibrated our new model to various current observations of the EoR, namely the Bouwens et al. (2015) SFR observations, the Planck (2016) optical depth measurements, and the Becker & Bolton (2013) Ṅion data. We also compared our new EoR model to our previous EoR model from chapter 2 in terms of their EoR history, H II bubble sizes, and 21cm power spectra. We further studied variations in the 21cm fluctuations produced by all possible variants of our ionisation conditions.

We then presented a robust MCMC analysis to constrain our generalized source model's free parameters against current EoR observations. We used the well-calibrated EoR model to predict the 21cm power spectrum for the future EoR array experiments SKA, HERA, and LOFAR. We show how the future 21cm observations are important for complementing the existing EoR current observations in order to tightly estimate the astrophysical parameters of EoR sources.

Our key findings are as follows:

- The Time-integrated EoR model produces very large H II bubbles as compared with the Instantaneous EoR model, and fewer small bubbles. This difference is clearly shown in their evolving HI maps (figure 3.2) and the ionisation field (figure 3.3). This results in a larger ionisation and 21cm power spectrum on large scales by 1-1.2 orders of magnitude as seen in (Figure 3.4 and 3.5).

- By considering all possible combinations between the hydrogen atoms and recombination terms in the ionisation condition, we showed that recombinations are subdominant in determining the 21cm power spectrum particularly on large scales (Figure 3.6). The 21cm power spectrum amplitude and shape are highly sensitive to accounting for the amount of and fluctuations in the

neutral hydrogen density. This means semi-numerical models must carefully account for the neutral hydrogen to robustly predict the expected 21cm signal.

- The Bouwens et al. (2015) SFR observations provide tight constraints on the ionising emissivity amplitude $A_{\rm ion}$ and the slope of the $R_{\rm ion}$-M_h relation $C_{\rm ion}$, but provide no constraint on the photon escape fraction $f_{\rm esc}$ (Figure 3.7). The recent Planck (2016) optical depth (Figure 3.8) and the Becker & Bolton (2013) $\dot{N}$ion measurements (Figure 3.10) poorly constrain our model parameters, while they slightly prefers models with lower values of $f_{\rm esc}$, $A_{\rm ion}$ and $C_{\rm ion}$.

- Combining all of SFR, τ and $\dot{N}$ion together results in tighter parameter constraints, as seen in Figure 3.11. The $A_{\rm ion}$ and $C_{\rm ion}$ here follow the previous constraints by the SFR observations, but combining these measurements yields better escape fraction constraints of $f_{\rm esc} = 0.25^{+0.26}_{-0.13}$, though still not very tight. The parameters determined directly from the full hydrodynamic simulations analysed in chapter 2 are consistent with these constraints.

- Using the well-calibrated Time-integrated EoR model, we predict the 21cm power spectrum at different redshifts ($z = 9, 8.5, 8$) for several constructed radio array designs, namely SKA, HERA, and LOFAR (Figure 3.12). While LOFAR does not provide strong constraints except at the largest scales, future experiments will tightly constrain the 21cm power spectrum to smaller scales that can better constrain the reionising source population.

- By adding current EoR observations (SFR, τ, $\dot{N}$ion) to the 21cm mock observations, we find that all experiments recovers the input model parameter accurately and the parameters error are futher improved. This illustrates how future 21cm observations can complement and substantially improve upon existing EoR observations in order to more tightly constrain the emissivity of EoR sources and their relationship to the underlying halo population.

- We find that photon conservation is sub-optimal owing to the way the excursion set formalism is generically implemented in current semi-numerical codes, including SimFast21. The root difficulty is that cells are treated as fully neutral or fully ionised, with no possibility of intermediate ionisation levels. While some tuning could be done to minimise the problem, a robust solution likely lies in replacing the excursion set-formalism with

a proper photon-conserving radiative transfer approach. We leave this for future work.
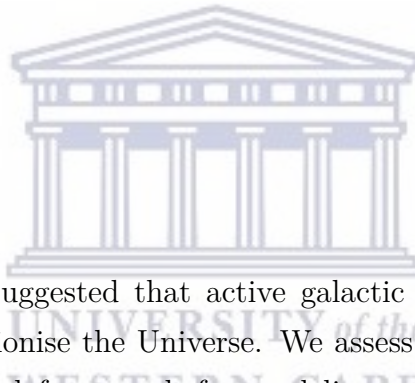
We have discussed the uncertainty associated with ionization condition in the excursion set-based models and found that a slight change in the ionization condition could lead to a big difference in the 21cm power spectrum particularly on large scales as seen between the Time-integrated and Instantaneous model. A possible approach to break such degeneracy and resolve the ionization condition uncertainty is to compare these models' 21cm power spectra to radiative transfer simulations. For this reason, we are currently developing our own radiative transfer routine (SIMFAST21-RT) and the result will be forthcoming.

The SIMFAST21-MCMC platform developed here will be applicable for a wide range of EoR forecasting science cases. By robustly incorporating all the current observables within an MCMC framework and being able to straightforwardly incorporate new data, we are building the tools necessary to optimally connect future redshifted 21cm power spectrum from the EoR to physical quantities associated with the population of reionising sources. Such a framework can be used to explore and constrain exotic source populations such as mini-quasars or Population III stars, as well as to potentially extend to multi-tracer cross-correlation approaches. The most immediate hurdle will be to develop a more robust yet still fast radiative transfer method that conserves photons, so we can more reliably assess the obtained source population parameters. There is much exciting work to be done as we continue to prepare for the 21cm EoR era.

Chapter 4

Constraining the contribution of active galactic nuclei to reionisation

Abstract

Recent results have suggested that active galactic nuclei (AGN) could provide enough photons to reionise the Universe. We assess the viability of this scenario using a semi-numerical framework for modeling reionisation, to which we add a quasar contribution by constructing a Quasar Halo Occupation Distribution (QHOD) based on Giallongo et al. observations. Assuming a constant QHOD, we find that an AGN-only model cannot simultaneously match observations of the optical depth τ_e, neutral fraction, and ionising emissivity. Such a model predicts τ_e too low by $\sim 2\sigma$ relative to Planck constraints, and reionises the Universe at $z \lesssim 5$. Arbitrarily increasing the AGN emissivity to match these results yields a strong mismatch with the observed ionising emissivity at $z \sim 5$. If we instead assume a redshift-independent AGN luminosity function yielding an emissivity evolution like that assumed in Madau & Haardt model, then we can match τ_e albeit with late reionisation; however such evolution is inconsistent with observations at $z \sim 4-6$ and poorly motivated physically. These results arise because AGN are more biased towards massive halos than typical reionising galaxies, resulting in stronger clustering and later formation times. AGN-dominated models produce larger ionising bubbles that are reflected in $\sim \times 2$ more 21cm power on all scales. A model

with equal parts galaxies and AGN contribution is still (barely) consistent with observations, but could be distinguished using next-generation 21cm experiments HERA and SKA-low. We conclude that, even with recent claims of more faint AGN than previously thought, AGN are highly unlikely to dominate the ionising photon budget for reionisation.

4.1 Introduction

The nature of the sources driving the epoch of reionisation (EoR) in the early Universe remains uncertain. It is canonically believed that star-forming galaxies have provided the bulk of the ionising photon budget required to complete reionisation (Barkana & Loeb, 2001; Loeb & Barkana, 2001). This is because there is a significant decrease of observed active galactic nuclei (AGN) candidates at redshifts $z > 3$, such that the contribution from star-forming galaxies is expected to well exceed that of AGN at $z > 6$ (Shapiro & Giroux, 1987; Shankar & Mathur, 2007; Hopkins et al., 2007; Glikman et al., 2011; Masters et al., 2012; Haardt & Madau, 2012; Micheva et al., 2017; Ricci et al., 2017). However, there remain large uncertainties in the contribution of both star-forming galaxies and AGN to reionisation. Current constraints are now consistent with a minimal contribution from very low metallicity Population III stars (e.g. Robertson et al., 2015), but there is still the issue of the highly uncertain ionising photon escape fraction $f_{\rm esc,\star}$. Direct observations of $f_{\rm esc,\star}$ are quite difficult at $z \gtrsim 4$ owing to the ubiquity of strong absorption systems that suppress Lyman continuum flux and the difficulty in removing foreground interlopers, but careful measurements generally indicate $f_{\rm esc,\star}$ less than a few percent (e.g. Grazian et al., 2016; Vasei et al., 2016), with some evidence for a higher $f_{\rm esc,\star}$ in lower-mass galaxies (Vanzella et al., 2016; Grazian et al., 2017; Bian et al., 2017).

Theoretical models have tried to constrain $f_{\rm esc,\star}$ indirectly by matching models to other data, making a variety of assumptions for $f_{\rm esc,\star}$ such as a constant (e.g. Robertson et al. 2013; Finkelstein et al. 2015; Ma et al. 2015; Hassan et al. 2016), redshift-dependent (e.g. Kuhlen & Faucher-Giguére 2012; Mitra et al. 2013; Finlator et al. 2015; Qin et al. 2017), mass-dependent (e.g. Gnedin 2007; Yajima et al. 2011; Wise et al. 2014; Paardekooper et al. 2015), and recently UV magnitude-dependent $f_{\rm esc,\star}$ (Anderson et al., 2017; Japelj et al., 2017) in order to match simultaneously various reionisation constraints. The currently-favoured

lower value of Thomson scattering integrated optical depth ($\tau = 0.058 \pm 0.012$) measured by Planck (2016) prefers rather sudden and late reionisation scenarios, which relaxes the previously stringent constraints on the ionising photon budget. In chapter 3, we performed a detailed Monte Carlo Markov Chain (MCMC) analysis to constrain our semi-numerical model to several EoR key observables and found that $f_{\mathrm{esc},\star}$ is highly degenerate with the ionising emissivity amplitude, leading to a best fit value of $f_{\mathrm{esc},\star} = 0.25^{+0.26}_{-0.13}$, which allows a substantial range but is generally higher than available (lower-redshift) observations. Without a firmer understanding or direct measurement of $f_{\mathrm{esc},\star}$, it is difficult to conclusively argue that star-forming galaxies can provide all the photons required for reionisation.

Recently, there has been renewed interest in assessing the contribution of AGN to the reionising photon budget. Previous estimates of the AGN contribution relied on an extrapolation to faint luminosities based on lower-redshift results. But recent deep observations have enabled a more direct characterisation of the faint end. Giallongo et al. (2015, hereafter G15) identified 22 faint AGN candidates at $z > 4$ and inferred a significantly steeper faint-end slope than what is seen at lower redshifts. We note that claims of such a steep faint end remain controversial; for instance Parsa et al. (2017) was unable to confirm a substantial fraction of the G15 candidates based on additional multi-wavelength data. Furthermore, recent spectroscopic surveys (Kim et al., 2015; Jiang et al., 2016) have concluded that the observed quasars population at high redshift might not be enough to fully reionise the Universe. Nonetheless, the differing claims have led to speculation that AGN could provide the primary ionising photon contribution in order to keep the inter-galactic medium (IGM) highly ionised (e.g. Madau & Haardt, 2015). These claims further favor a late reionisation scenario in which the flatness observed in the ionising emissivity measurements by Becker & Bolton (2013) might arise naturally. In addition, they might also support the early and extended Helium reionisation observed by Worseck et al. (2016). Independently, Chardin et al. (2017) argued that the large scale opacity fluctuations in the Lyα forest measured by Becker et al. (2015) could be explained if AGN dominate the ionising UV background at $z \sim 6$ (see also Chardin et al. 2015). Hence the contribution of AGN to reionisation remains uncertain and potentially important or even dominant.

The idea that AGN might have driven cosmic reionisation has so far been investigated mostly in terms of global quantities, such as the ability to match the optical depth or comoving ionising emissivity constraints (e.g. Madau & Haardt, 2015;

Mitra et al., 2016; Mao & Kim, 2016; Khaire et al., 2016; Qin et al., 2017). It remains to be demonstrated whether AGN-driven models are able to simultaneously satisfy all the current reionisation-epoch constraints. An important upcoming addition to the pantheon of constraints will be the 21cm EoR power spectrum, which may be substantially different for AGN- versus star formation-driven reionisation, if AGN and star-forming galaxies cluster in different ways as one might naively expect. An early attempt by Geil & Wyithe (2009) to assess the effect of AGN on the 21cm power spectrum using a seminumerical scheme concluded that the effect is likely to be small, but more recent semi-numerical models by Kulkarni et al. (2017) have suggested the opposite, that AGN produce signficantly different 21cm signal. However, Kulkarni et al. (2017) populates AGN only in the most massive halos using abundance matching to the halo velocity, employing the observed velocity-black hole mass relation at lower redshifts (Tremaine et al., 2002; Ferrarese, 2002), which thus effectively adopts a unity duty cycle of AGN for massive halos. However, recent results from Hyper Suprime-Cam suggest that quasars do not necessarily live in the most overdense regions where massive halos are expected to reside, and that their duty cycle is below a few percent (He et al., 2017). Accounting for sub-unity duty cycles inevitably drives black holes into lower-mass halos, altering the implied emissivity associated with haloes and epochs where they are not directly-measured. Moreover, the G15 data suggest that the AGN driving reionisation are rather faint, which may not be associated with the most massive halos. Without a proper treatment for AGN occupancy (duty cycle) and a more comprehensive analysis of all the implications of AGN-driven reionisation, it is difficult to properly assess the viability of this scenario.

In this chapter, we build on our semi-numerical framework based on the SIM-FAST21 code to evolve the EoR ionisation field, which allows us to examine a range of EoR observations as we have done in previous chapters. To explore the AGN contribution, we populate AGN into halos with a more physically motivated approach that utilises both the observed luminosity function and abundance matching, thereby generating a Quasar Halo Occupancy Distribution (QHOD); our scheme partially follows the recipe summarized in Choudhury & Ferrara (2005). We constrain our QHOD to match the G15 AGN LF fit at $z = 5.75$, and assign AGN randomly into halos. This QHOD *predicts* a duty cycle that is close to unity for extremely massive halos, but drops to sub-percent values at intermediate halo masses. To obtain the AGN emissivity, we utilise the strong correlation observed

between the circular velocity and black hole mass following low redshift observations (Tremaine et al., 2002; Ferrarese, 2002). We account for this additional AGN photon contribution while we evolve our SimFast21 density and ionisation field, including the effects of recombination and time-evolving neutral fractions.

This work improves on previous efforts in several ways. First, using our SimFast21-based framework, we examine a wider variety of simultaneous constraints on the evolution of AGN-driven reionisation, including the Thomson optical depth, the mean cosmic neutral fraction evolution, and the ionising emissivity at the end of reionisation. Second, our model for populating quasars into halos is more realistic than previous works because we apply constraints beyond just abundance matching, allowing us to directly constrain the duty cycle of AGN as a function of halo mass. Third, we forecast upcoming 21cm EoR power spectrum measurements from LOFAR, HERA, and SKA, and illustrate how such future data might be able to constrain the fractional contribution of AGN to reionisation. Our primary conclusion is that it is very difficult to reconcile purely AGN-driven reionisation based on the (optimistic) G15 AGN luminosity function measurements with current global reionisation constraints. Future 21cm data should provide a new avenue to more precisely characterise the contribution of AGN to reionisation.

This chapter is organized as follows: In Section 4.2, we describe our semi-numerical simulation and the AGN model implementation and calibration. We compare AGN with star-forming galaxy models in terms of their EoR observables, present the 21cm predictions, and discuss how future experiments can discriminate between these models in Section 4.3. We finally conclude in Section 4.4. Throughout this work, we adopt a ΛCDM cosmology in which $\Omega_{\mathrm{M}} = 0.3$, $\Omega_{\Lambda} = 0.7$, $h \equiv H_0/(100\,\mathrm{km/s/Mpc}) = 0.7$, a primordial power spectrum index $n = 0.96$, an amplitude of the mass fluctuations scaled to $\sigma_8 = 0.8$, and $\Omega_b = 0.045$. We quote all results in comoving units, unless otherwise stated.

4.2 Simulations Using SimFast21

We use the recently developed Time-integrated version of our semi-numerical code SimFast21 (Santos et al. 2010) that has been presented in chapter 3, which we here briefly review.

The dark matter density field is generated using a Monte-Carlo Gaussian approach, which is dynamically evolved into the non-linear regime via applying the Zel'dovich (1970) approximation. The dark matter halos are generated using the well known excursion set formalism (ESF). In the Time-integrated model, the ionised regions are identified using a similar form of the ESF that is based on comparing the time-integrated ionisation rate $R_{\rm ion}$ with that of the recombination rate $R_{\rm rec}$ and the local neutral Hydrogen density within each spherical volume specified by the ESF. Regions are flagged as ionised if:

$$\int f_{\rm esc} R_{\rm ion} \, dt \geq \int x_{\rm HII} \, R_{\rm rec} \, dt + (1 - x_{\rm HII}) \, N_{\rm H} \,, \qquad (4.1)$$

where $f_{\rm esc}$ is the photon escape fraction, $x_{\rm HII}$ is the ionised fraction, and $N_{\rm H}$ is the total number of hydrogen atoms. This is a generalized form of the ionisation condition in the Time-integrated model, which can be used for any ionising source or sink populations to run the reionisation calculations. With this ionisation condition, reionisation occurs more suddenly compared to our previous Instantaneous model developed in chapter 2, in which the ionisation condition was based on an instantaneous comparison of $R_{\rm ion}$ and $R_{\rm rec}$. The more sudden reionisation is favoured by recent Planck (2016) data, and in chapter 3 we showed that the Time-integrated ionisation condition produces larger ionised bubbles, resulting in 21 power spectrum enhancement on large scales.

4.2.1 Sink model

Reionisation, in short, is an evolving battle between ionising photon sources and sinks. To model sinks, we must account for the clumping effects from small scales below what we can directly evolve using the large-scale SimFast21 code (typically, sub-Mpc scales). We thus parametrize the inhomogeneous recombination rate $R_{\rm rec}$ from high-resolution full radiative transfer hydrodynamic simulations (hereafter 6/256-RT) (Finlator et al., 2015) as a function of over-density Δ and redshift z, as follows:

$$\frac{R_{\rm rec}}{V} = A_{\rm rec}(1 + z)^{D_{\rm rec}} \left[\frac{(\Delta/B_{\rm rec})^{C_{\rm rec}}}{1 + (\Delta/B_{\rm rec})^{C_{\rm rec}}} \right]^4 \,, \qquad (4.2)$$

where $A_{\rm rec} = 9.85 \times 10^{-24} {\rm cm}^{-3} {\rm s}^{-1}$ (proper units), $B_{\rm rec} = 1.76$, $C_{\rm rec} = 0.82$, $D_{\rm rec} = 5.07$. Consistent with Sobacchi & Mesinger (2014), our recombination

rate $R_{\rm rec}$ parametrization suppresses the ionisation and 21cm power spectrum on large scales, as seen in chapter 2.

We note that AGN-only reionisation scenarios are found to substantially heat the IGM (D'Aloisio et al., 2016; Oñorbe et al., 2017), which lowers the recombination rate. This may reduce $R_{\rm rec}$ by up to a factor of ~ 2 in our AGN-only models, which in turn may slightly advance reionisation by AGN, and hence improving the viability of AGN-only models. We do not account for this effect in our calculation since we expect it to be sub-dominant compared to other effects related to halo growth, and here simply use the same sink model to compare reionisation histories produced by Galaxies versus AGN.

4.2.2 Source model: Star-forming galaxies

For the stellar contribution, we use a parametrization obtained from combining the 6/256-RT with larger-volume hydrodynamic galaxy formation simulation (Davé et al., 2013) (hereafter 32/512), that have both been shown to match a range of observations including lower redshift data. From these simulations, we parametrize the non-linear ionisation $R_{\rm ion,\star}$ rate as a function of halo mass $M_{\rm h}$ and redshift z as follows:

$$\frac{R_{\rm ion,\star}}{M_{\rm h}} = A_{\rm ion} \left(1 + z\right)^{D_{\rm ion}} \left(M_{\rm h}/B_{\rm ion}\right)^{C_{\rm ion}} \exp\left(-(B_{\rm ion}/M_{\rm h})^{3.0}\right), \qquad (4.3)$$

where $A_{\rm ion} = 1.08 \times 10^{40}~{\rm M}_\odot^{-1}{\rm s}^{-1}$, $B_{\rm ion} = 9.51 \times 10^7~{\rm M}_\odot$, $C_{\rm ion} = 0.41$ and $D_{\rm ion} = 2.28$. This ionisation rate is computed directly from the star formation rate (SFR) of these simulations based on stellar population models applied to star formation histories of simulated galaxies.

In chapter 3 we considered a more generalized form of this source model, and found that constraining these parameters against several EoR observations using MCMC analysis resulted in best-fit values that matched the above parameters to within uncertainties, thereby validating the extrapolation from the small scales of 6/256-RT and 32/512 simulations to large scales covered by SimFast21 simulations. We further showed that using this non-linear ionisation rate relation boosts the small scales 21cm power spectrum as compared with models assuming a linear relation between the ionisation rate and halo mass; see previous chapters for more details.

4.2.3 Source model: AGN

The new aspect of the source model for this work is the AGN ionising photon output. We compute the ionisation rate from AGN $R_{\rm ion,AGN}$ following partially the recipe summarized in Choudhury & Ferrara (2005). Motivated by low redshift observations (Tremaine et al., 2002; Ferrarese, 2002), the basic assumption is that the black hole mass $M_{\rm bh}$ is strongly correlated with the hosting halo's circular velocity $v_{\rm cir}$. We assume that this correlation is independent of redshift and valid during the reionisation redshifts. This correlation can be written as:

$$\frac{M_{\rm bh}}{M_\odot} = A \left(\frac{v_{\rm cir}}{159.4\,{\rm km\,s^{-1}}}\right)^5 , \tag{4.4}$$

where A may be regarded as the black hole formation efficiency, which is our only free parameter in the AGN source model at fixed $f_{\rm esc,AGN}$. We then fix A to match the AGN ionising emissivity constraints from G15, as we describe in §4.2.4. It is worthwhile to mention that this observed correlation (Equation 4.4) would naturally arise if one applies a self-regulation condition on the black hole growth as previously shown by Wyithe & Loeb (2003).

For our adopted cosmology, the circular velocity $v_{\rm cir}$ of a given halo mass M_h is given by:

$$\frac{v_{\rm cir}}{\rm km\,s^{-1}} = 0.014 \left(M_h \sqrt{\Omega_m(1+z)^3 + \Omega_\Lambda}\right)^{1/3} . \tag{4.5}$$

Having obtained the black hole mass $M_{\rm bh}$, the Eddington luminosity in the B-band is given by (Choudhury & Ferrara, 2005)

$$\frac{L_B}{L_{\odot,B}} = 5.7 \times 10^3 \frac{M_{\rm bh}}{M_\odot} . \tag{4.6}$$

Given this B-band luminosity, we must now determine the ionising photon output. Following Schirber & Bullock (2003) and Telfer et al. (2002), we assume the spectral energy distribution for AGN takes a power law form:

$$L_\nu = L_{912} \left(\frac{\nu}{\nu_{912}}\right)^{-1.57} , \tag{4.7}$$

where L_{912} is the luminosity at the Lyman limit that is given by:

$$\frac{L_{912}}{\rm ergs\,s^{-1}\,Hz^{-1}} = 10^{18.05} \frac{L_B}{L_{\odot,B}} . \tag{4.8}$$

We then integrate the above over all frequencies to find the ionisation rate $R_{\rm ion,AGN}$ as follows:

$$R_{\rm ion,AGN} = \int_{\nu_{912}}^{\infty} \frac{L_\nu}{h\nu}\,d\nu = \frac{L_{912}}{1.57\,h}. \tag{4.9}$$

This explains how we compute the AGN ionisation rate $R_{\rm ion,AGN}$ given the host halo properties.

Next, we must populate the AGN into our halos. Here is where we make use of the G15 AGN Luminosity Function (LF). G15 evaluated this at $\lambda = 1450$ for several redshifts higher than $z = 4$. We then use G15 LF fit at their highest redshift z=5.75 to compute the number of AGN as a function of halo mass in our simulations. G15 LF at z=5.75 can be best fit using a double power law as follows:

$$\phi = \frac{\phi^*}{10^{0.4(M_{\rm break}-M)(\beta-1.0)} + 10^{0.4(M_{\rm break}-M)(\gamma-1.0)}}, \tag{4.10}$$

where ϕ is the comoving AGN density, M is the absolute magnitude computed via the standard relation $M_{\rm AB} = -2.5\log_{10}(L_\nu) + 51.60$, $\log_{10}\phi^* = -5.8$ Mpc^{-3}, $M_{\rm break} = -23.4$, $\beta = 1.66$, and $\gamma = 3.35$.

Putting this together, our procedure to populate AGN into halos is as follows:

1. We bin the halo catalogs as a function of halo mass, and find the average halo mass in every bin of $\Delta \log_{10} M_{\rm h} = 0.34$.

2. Using Equation 4.4 to 4.7, we compute the corresponding AGN L_{1450} and M_{1450} of each halo mass bin.

3. We then obtain the number of AGN for each halo mass bin using Equation 4.10, which turns out to always be less than the actual number of halos; the ratio of these numbers is the duty cycle of AGN for that halo mass bin.

4. We randomly assign the appropriate number of AGN into halos within that mass bin.

Note that in step (3) one ideally may assume Poisson fluctuations around the number of AGN following McQuinn et al. (2009) QSO Method I, since the luminosity function, in principle, yields the average number of AGN at a given magnitude bin per the simulation volume. We ignore these fluctuations for two complementary reasons. First, the number of AGN obtained from the G15 LF is very large,

particularly, at the faint end (N $\sim 10^6$) around which the Poisson fluctuations can be neglected ($\sqrt{N} \sim 10^3$). Second, as will be seen later, our results are mainly driven by the strong AGN clustering at the faint end, and hence adding Poisson fluctuations at the very bright end (e.g. first few magnitude bins) is unlikely to affect the results since bright sources are rare. In such a situation, the average number of AGN is a very good approximation to the actual number of AGN. We then round off the resulting AGN number in order not to populate halos with fractional AGN, but this in fact is a small correction.

Following the above procedure, we now have plausible AGN population in our simulation box at $z = 5.75$. To quantify the evolution of the AGN population, we must make a choice regarding the evolution of AGN relative to that of the halos. Given that theoretical predictions for AGN evolution are relatively uncertain, the simplest assumption is to assume that the relationship between AGN and their host halos do not change at $z \geq 5.75$. In other words, we assume that the Quasar Halo Occupation Distribution (QHOD) is non-evolving. This is a reasonable assumption since the HOD of galaxies have been studied extensively (see Yoshikawa et al. 2001; Berlind et al. 2003, and references therein) and it is found that the HOD is nearly a redshift-independent quantity.

The QHOD as a function of halo mass M_h can directly be calculated from G15 LF fit at z=5.75 (Equation 4.10) as the ratio between the number of AGN to that of their hosting halos for each halo mass bin. Our QHOD can be well fit with a constant plus a power law as follows:

$$\mathrm{N} = \left(\frac{M_h}{2.19 \times 10^{12}}\right)^{0.9} + 0.023\,. \qquad (4.11)$$

Note that the QHOD changes with different values of our free parameter A relating black hole mass to circular velocity, which translates into a shift in magnitudes of the AGN. Here we have used $A = 5 \times 10^5$, a value at which our constant QHOD AGN model is calibrated to reproduce the G15 ionising emissivity constraints, as will be discussed next in §4.2.4.

Figure 4.1 shows the QHOD computed from G15 observations at z=5.75 (closed circles) and our QHOD fit in Equation 4.11. The QHOD represents a plausible description of the AGN occupancy in their hosting halos. Indeed, this can also be regarded as an AGN duty cycle, if one (reasonably) postulates that every halo contains a black hole but only some fraction of them are detectably active. The
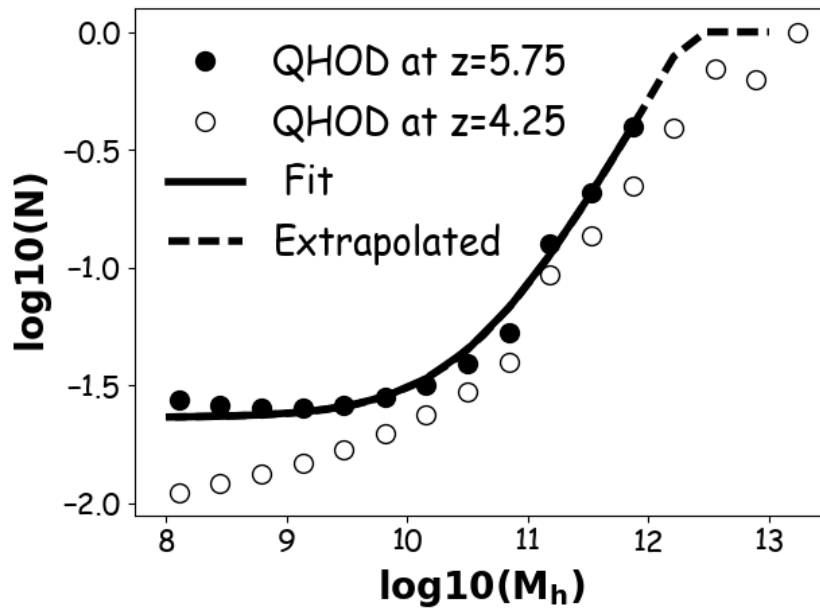
FIGURE 4.1: The Quasar Halo Occupancy Distribution (QHOD) as function of halo mass M_h computed from G15 LF at z=5.75 (Equation 4.10, closed circles) and at z=4.25 (open circles). The QHOD is relatively similar at these two redshift bins, providing an evidence that the QHOD doesn't evolve strongly with redshift. The solid line represents the fitting function written in Equation 4.11 for QHOD data at z=5.75. The fitting function is extrapolated (dashed) for halo masses higher than $M_h = 10^{12}$ and set to unity as an extreme occupation condition since AGN number should not exceed halos number. The QHOD increases as the M_h increases, showing that there are few AGN at massive halo mass bins. This fitting function will be used to evolve AGN from z=5.75 to high redshifts in our constant QHOD AGN fiducial model.

He et al. (2017) observations suggest a duty cycle of $0.001 - 0.06$ for moderate-mass halos, which is somewhat lower than our model assumes but qualitatively agrees with the trend that the duty cycle is smaller in lower-mass halos. For comparison, we also plot the QHOD at $z = 4.25$ that is computed from G15 LF at that redshift bin (open circles in Figure 4.1). We notice that the QHOD data at $z = 5.75$ and $z = 4.25$ are fairly similar, differing by $\sim 30\%$ for all $M_h \gtrsim 10^{10} M_\odot$. This suggests that the QHOD doesn't evolve strongly with redshift, and motivates us to fiducially assume that the QHOD does not evolve. We will call this the "constant QHOD" case. In this case, we replace Equation 4.10 with Equation 4.11 in step (ii) to compute directly the number of AGN in each halo mass bin at higher redshifts. Note that in step (iv) AGN assignment is completely random and redshift-independent. As a result, halos with AGN may or may not have AGN at the next time step. This is realistic since the simulation time step (dz=0.125) is typically larger than the AGN lifetime.

As a counterpoint to this case, we also consider a model where the AGN luminosity function is constant with time. Here, we calculate the AGN number at all redshifts based on G15 LF fit at $z = 5.75$ (Equation 4.10). We will call this the "constant LF" case. This is less realistic because the QHOD here increases strongly with redshift, since there are many fewer halos at higher redshifts but the number of AGN remains fixed following the assumed constant LF. Also, observations of the AGN LF at lower redshifts ($z \lesssim 6$) exhibit significant evolution, so it seems unlikely that this evolution should suddenly cease. Nonetheless, the emissivity evolution in this case turns out to be similar to the AGN comoving ionising emissivity model assumed by Madau & Haardt (2015), hence it represents an interesting contrasting case that we will examine in §4.3.

4.2.4 AGN source model calibration

Our next task is to calibrate the relationship between black hole mass and circular velocity via the normalization parameter A in Equation 4.4. Observationally, this parameter is not tightly constrained and has only been measured at low redshifts.

We first calibrate the constant QHOD and constant LF AGN models to at least match the G15 ionising emissivity constraints at z=5.75 in order to verify the possibility to complete reionisation solely by AGN. This we achieve by tuning the black hole formation efficiency A in our AGN models to match the total ionising emissivity measurements at 912 (ϵ_{912}), which is the total escaped L_{912} of all AGN divided by the simulation comoving volume. The simulation configurations of these models are presented in §4.3 with the rest of our fiducial models. We assume $f_{\text{esc,AGN}} = 100\%$ for AGN, which is standard (e.g. Madau & Haardt, 2015).

We find that the constant LF AGN model can match the G15 ionising emissivity constraints with $A = 10^6$ whereas the constant QHOD AGN model requires $A = 5 \times 10^5$. We note that what is really constrained here is the product of $Af_{\text{esc,AGN}}$, so we have the freedom to keep A fixed and tune $f_{\text{esc,AGN}}$ instead; all our results would be unchanged. In this case, the constant QHOD and constant LF AGN models would require $f_{\text{esc,AGN}} = 50, 100\%$ at $A = 10^6$ to match the G15 constraints, respectively. Note that we do make the assumption here that the product $Af_{\text{esc,AGN}}$ does not vary with redshift.
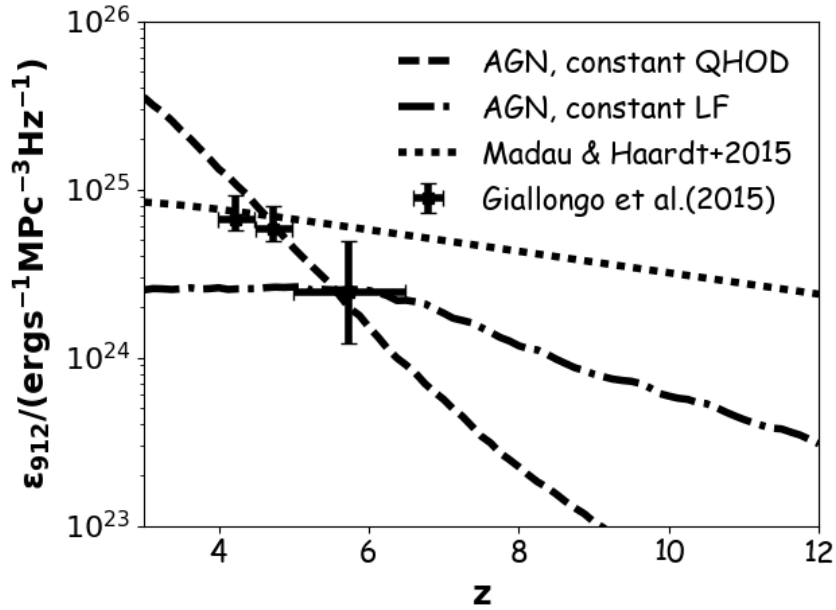
FIGURE 4.2: The comoving ionising emissivity of AGN at 912 . The constant LF AGN model (dot-dashed) only matches the G15 constraints (1-σ level) at z=5.75 which exhibits a slowly growing emissivity evolution that is somewhat similar to the emissivity shape by Madau & Haardt (2015) (dotted). The constant QHOD AGN model (dashed) yields more physical evolution as the ionising emissivity grows rapidly which in turn results in matching almost all of G15 data.

In Figure 4.2, we show the comoving ionising emissivity evolution obtained with the procedure discussed above. The constant LF AGN model produces a slowly growing emissivity, which is similar to the evolution expected from models in which ionising radiation is dominated by star-forming galaxies, and similar in shape to that assumed in Madau & Haardt (2015). While matching the G15 constraints at $z = 5.75$, the constant LF AGN model under-estimates the ionising emissivity by a factor of ~ 3 as compared with G15 constraints at $z = 4.75$ and $z = 4.25$. In contrast, the emissivity from our fiducial constant QHOD AGN model matches simultaneously G15 data at several redshifts bins due to the rapidly growing emissivity evolution as expected from an AGN dominated model. This further validates our assumption that using constant QHOD is a more physically motivated approach than using the constant LF.

Note that we have intentionally not applied a magnitude cut-off in computing the integral of emissivity (ϵ_{912}); G15 used a cutoff of $M_{1450} = -18$. At $z = 5.75$, the total comoving ionising emissivity is $\epsilon_{912} = 2.12 \times 10^{24}$ erg s^{-1} Mpc^{-3} Hz^{-1}, whereas with a magnitude cut-off of $M_{1450} = -18$ it becomes $\epsilon_{912} = 1.58 \times 10^{24}$ erg s^{-1} Mpc^{-3} Hz^{-1}. This shows that those fainter AGN contribute $\sim 25\%$ to the

total emissivity, which is modest but not negligible. We include this in order to check whether including all faint AGN would allow reionisation completion to be consistent with neutral fraction and optical depth constraints. This means that we are effectively studying an optimal case for reionisation by AGN, since those fainter than $M_{1450} > -18$ might already be a part of the galaxy population as discussed in Chardin et al. (2017), due to the overlap between the galaxy and AGN luminosity functions at this faint limit. Applying a magnitude cut-off would suppress the ionising emissivity and further delay reionisation.

In summary, we have described our procedure to obtain the ionising emissivity of AGN as a function of halo mass, and then populate AGN into halos within SimFast21 via constraining the halo occupancy of AGN (QHOD) using the G15 AGN LF. The total emissivity is calibrated to match that observed by G15 at $z = 5.75$, which fixes our free parameter relating black hole mass to halo circular velocity. Our fiducial model assumes a constant QHOD, and we will also consider a constant AGN LF. We now study the predictions of our model for reionisation observables, and compare the results with our previous SimFast21 models where we considered only star-forming galaxies.

4.3 EoR Observables

4.3.1 SimFast21 runs

We run all of our EoR realizations using the Time-integrated model from chapter 3 to establish a proper comparison between the different source models. Using the same density field and halo catalogs generated in a box size L= 300 Mpc and N= 560^3 number of cells, we run 4 different EoR models based on different ionisation sources as follows (and summarized in Table 4.1):

- **Galaxies**: This model only considers ionising photons emitted by star-forming galaxies using Equation (4.3) with parameters: $f_{\mathrm{esc},\star} = 0.25$, A_{ion} = 4.27×10^{39}, $C_{\mathrm{ion}} = 0.44$. These parameters are suggested by our recent MCMC analysis in chapter 3 to match simultaneously various EoR constraints including the SFR densities at several redshift bins as compiled by Bouwens et al. (2015), integrated ionising emissivity at z ∼ 5 by Becker & Bolton (2013) and Planck (2016) optical depth.

Model	$f_{\mathrm{esc},\star}$	$f_{\mathrm{esc,AGN}}$	ionisation rate	τ_e	z_{reion}
Galaxies	0.25	0.0	$f_{\mathrm{esc},\star}\, R_{\mathrm{ion},\star}$	0.057	7.5
constant QHOD AGN	0.0	1.0	$f_{\mathrm{esc,AGN}}\, R_{\mathrm{ion,AGN}}$	0.036	5.0
50-50	0.125	0.5	$f_{\mathrm{esc},\star}\, R_{\mathrm{ion},\star} + f_{\mathrm{esc,AGN}}\, R_{\mathrm{ion,AGN}}$	0.049	6.5
constant LF AGN	0.0	1.0	$f_{\mathrm{esc,AGN}}\, R_{\mathrm{ion,AGN}}$	0.048	4.0

TABLE 4.1: Summary of models considered in section 4.3 to compare between the AGN and star-forming galaxies impacts on different reionisation constraints. Columns (from left to right) are: models' names, the photon escape fractions from star-forming galaxies $f_{\mathrm{esc},\star}$ and AGN $f_{\mathrm{esc,AGN}}$, the ionisation rate used in Equation (4.1), the optical depth τ_e, and reionisation redshift z_{reion} defined at neutral fraction limit $x_{\mathrm{HI}} < 10^{-3}$.

- **constant QHOD**: This is our fiducial AGN model in which the AGN are the only source for ionising radiation using $f_{\mathrm{esc,AGN}}$=1.0, and our QHOD fitting function (Equation 4.11) computed from G15 LF fit at $z = 5.75$.

- **50-50**: This model contains an equal contribution from the **Galaxies** and **constant QHOD** models, specifically we use $f_{\mathrm{esc},\star} = 0.125$ and $f_{\mathrm{esc,AGN}} = 0.5$.

- **constant LF**: This is our alternative AGN model which uses the actual LF fit of G15 at $z = 5.75$ to compute the number of AGN at all redshifts, with $f_{\mathrm{esc,AGN}}$=1.0.

4.3.2 Ionising emissivity

We begin by comparing the integrated ionising emissivity $\dot{N}_{\mathrm{ion}}$ of these models, which is the total number of ionising photons per second per comoving volume. We compare our models with results from Qin et al. (2017) based on the DRAGONS simulation, which uses the MERAXES semi-analytic galaxy formation model built upon the TIAMAT N-body simulation. The Qin et al. (2017) model is able to track the growth of central super-massive black holes and reproduce wide range of observations including the observed quasar LF from $z \sim 0.6 - 6$. Their model predicts that AGN contribution to EoR is minimal, so it is interesting to compare our AGN emissivity with theirs.

Figure 4.3 shows the redshift evolution of the comoving integrated ionising emissivity $\dot{N}_{\mathrm{ion}}$, in units of 10^{51} s^{-1}Mpc^{-3}, for our four models. For the Qin et al. (2017) models (blue lines), we show their full galaxies+AGN model as well as
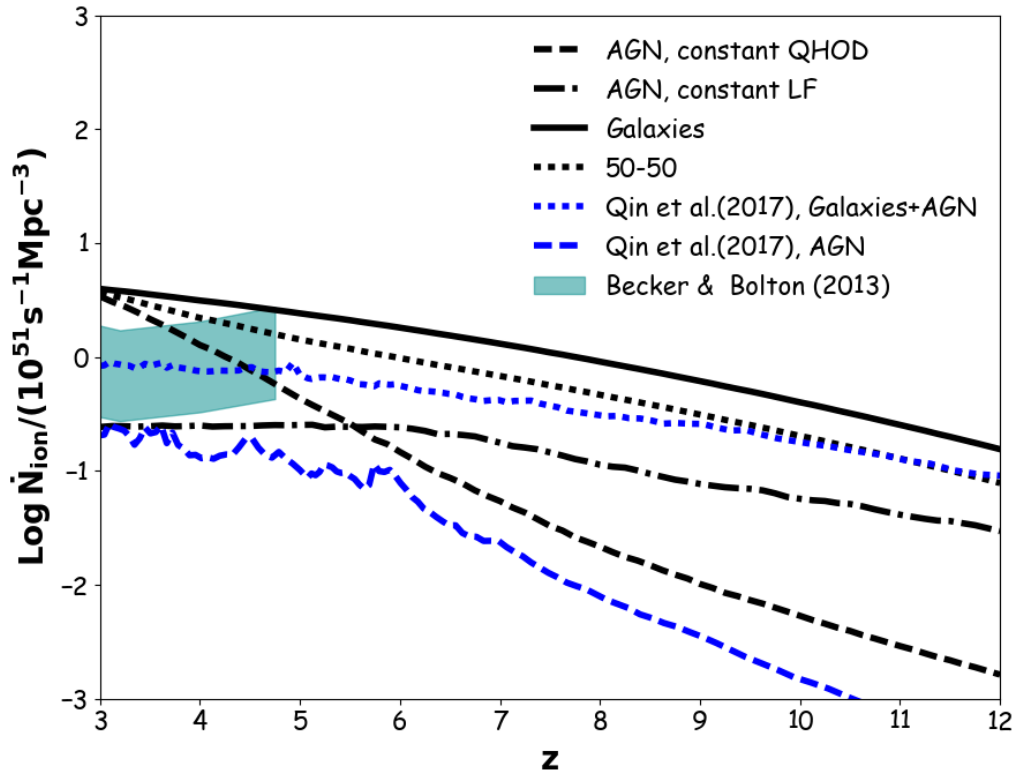
FIGURE 4.3: The comoving integrated ionising emissivity as a function of redshift. The Becker & Bolton (2013) measurements are shown with the cyan shaded area (1-σ level). The emissivity evolution in our Galaxies model (black solid) and Galaxies+AGN model (dotted blue) by Qin et al. (2017) is similar with an amplitude difference due to these models' basic framework and assumption (see text for details). The emissivity in constant LF AGN model (dot-dashed black) grows slowly similar to galaxies driven-EoR models, which reflects the poor assumption of using a fixed AGN LF through all times. Our fiducial constant QHOD AGN model (dashed black) produces reasonable emissivity evolution with a steep decline towards high redshift, consistent with the AGN model (dashed blue) by Qin et al. (2017).

their AGN-only contribution. At $z \lesssim 5$, we show the observational constraints from Becker & Bolton (2013) inferred from Lyα forest measurements.

Our Galaxies model skirts the upper limit of Becker & Bolton (2013) constraints while simultaneously calibrated to reproduce the Bouwens et al. (2015) SFR and Planck (2016) optical depth, as discussed in chapter 3. Adopting a mildly redshift-dependent or even mass-dependent $f_{esc,\star}$ would permit a better match with the amplitude and flat redshift dependence of the Becker & Bolton (2013) emissivity measurements, as suggested by Mutch et al. (2016), without much altering the Thomson optical depth.

Our fiducial constant QHOD model shows a much more rapid growth of ionising

emissivity with time than the Galaxies model, which matches the Becker & Bolton (2013) ionising emissivity at the upper end of the observed redshift range but overshoots the low end. In this model, the AGN contribution overtakes the Galaxies contribution at $z \sim 3$, which is in agreement with what is typically inferred (e.g. Haardt & Madau, 2012).

We further see that our 50-50 model (dotted black in Figure 4.3) is similar and much closer to the Galaxies model than to the constant QHOD model. This indicates that the contribution from star-forming galaxies dominates the ionising emissivity while AGN contribution is minor.

Finally, the constant LF model shows a relatively shallow evolution, approximately parallel to the galaxies case but significantly lower in amplitude. This falls just below the ionising emissivity data at $z \lesssim 5$.

The blue dotted and dashed lines show the evolution of the emissivities from the Qin et al. (2017) model, with the latter showing only the contribution from AGN. Their AGN contribution shows a similar redshift dependence to our constant QHOD model, which further supports the validity of this assumption, at least down to $z \sim 6$. It is possible that our assumption breaks down at $z \lesssim 5$ as their AGN contribution flattens, and if ours did this then the agreement with the observed evolution of the emissivity would improve. However, DRAGONS also predicts that galaxies dominate the ionising photon budget at all redshifts, which may be contrary to studies of the hardness of the ionising background in the $z \sim 2 - 4$ IGM (e.g. Schaye et al., 2007; Oppenheimer et al., 2009).

The emissivity evolution in our Galaxies model is similar to that from the Galaxies+AGN model by Qin et al. (2017), whereas there is a difference in the amplitude due to these models' differences in the f_{esc} treatment (constant versus redshift-dependent). As previously noted, the constant LF AGN model shows a slowly growing emissivity similar to those of our Galaxies model and Galaxies + AGN model by Qin et al. (2017).

In summary, our fiducial constant QHOD AGN model matches the Becker & Bolton (2013) emissivity measurements reasonably well, at least at $z \sim 5$, but shows a dramatically different redshift evolution compared to our Galaxies and constant LF models. The Qin et al. (2017) DRAGONS model shows an evolution during reionisation that is consistent with our constant QHOD model for their AGN component, and with our Galaxies model for their overall emissivity (which

is dominated by galaxies), but somewhat lower in amplitude in each case. All these models are broadly in agreement with the emissivity measures at $z \sim 5$ given current uncertainties.

4.3.3 Global ionisation history and optical depth

We now explore our model predictions for other current observational constraints on the global evolution of reionisation, particularly the evolution of the volume-weighted neutral fraction x_{HI} and the integrated Thomson optical depth to electron scattering to the CMB τ_e.

Figure 4.4 shows a comparison between our models in terms of their global ionisation history, as characterised by the volume-weighted average neutral fraction x_{HI}. We see that our Galaxies and 50-50 models are consistent with several Ly-α forest measurements (shaded areas from Fan et al. 2006; Becker et al. 2015; Bouwens et al. 2015 and orange upper limits by McGreer et al. 2015). While both are consistent with data, the 50-50 model delays reionisation by $\Delta z \sim 1.0$, owing to the fact that galaxies are the main driver of reionisation as discussed in the previous section and their contribution has been halved in this model.

Turning to our AGN-driven reionisation models, we see that both the constant LF and constant QHOD reionise the Universe very late, with $x_{\mathrm{HI}} < 10^{-3}$ not occurring until $z \sim 4$ and $z \sim 5$, respectively. This is highly inconsistent with the Bouwens et al. (2015) constraints as seen in Figure 4.4, as well as direct observations of the Lyα forest in quasars at these epochs (Fan et al., 2006; Becker et al., 2015). The constant LF AGN model starts reionisation earlier than constant QHOD AGN model due to its higher emissivity at high redshifts (Figure 4.3). This too-late reionisation strongly suggests that AGN are unable to drive the bulk of reionisation, when constrained to match the observed ionising emissivity after the end of reionisation ($z \sim 5$).

As mentioned earlier, all models use the Time-integrated ionisation condition (Equation 4.1) to identify the ionised regions in the excursion set-formalism. We showed in previous chapters that this ionisation condition results in a more sudden reionisation as opposed to our previous Instantaneous model which yields an extended reionisation scenario. From Figure 4.4, all models yield a fairly sudden reionisation, consistent with our previous results, except the constant LF AGN
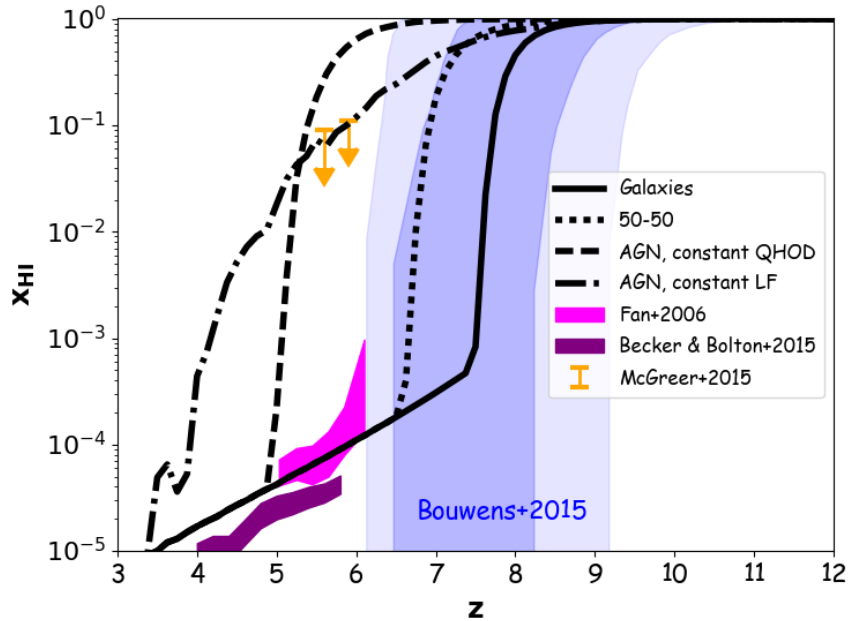
FIGURE 4.4: The volume-weighted averaged neutral fraction evolution as a function of redshift. The shaded areas: magenta, purple, and light blue are from Ly-α forest measurements by Fan et al. (2006), Becker et al. (2015), and several AGN and ly-α constraints (1-σ and 2-σ) as compiled by Bouwens et al. (2015), respectively. We also compare to the model independent upper limits by McGreer et al. (2015) (orange errorbars) using Ly-α and Ly-β forest. It is evident that Galaxies (solid) and 50-50 (dotted) models are consistent with all observations, which implies the importance of including star-forming galaxies to match with observations. Our AGN models, constant LF (dot-dashed) and constant QHOD (dashed), both complete reionisation very late. This indicates that AGN contribution to cosmic reionisation is minor.

model that shows an extended reionisation. This is because the fixed LF likely over-estimates the number of AGN at high redshifts, and furthermore the source population does not grow in concert with the growing sink population, which delays reionisation.

Figure 4.5 shows the evolution of the Thomson scattering optical depth (τ_e) as a function of redshift in these models. The Galaxies model is consistent with the recent Planck (2016) measurements (red shaded areas), mostly because it was constrained to do so via MCMC. The 50-50 and constant LF yield a lower optical depth of about $\tau \sim 0.049$, consistent with the lower limit of 1-σ level. However, the optical depth obtained by our fiducial constant QHOD AGN model is very low ($\tau \sim 0.036$) at the lower limit of the 2-σ level. Essentially, this model does not produce enough early photons in order to obtain a sufficient ionised path length to the CMB.
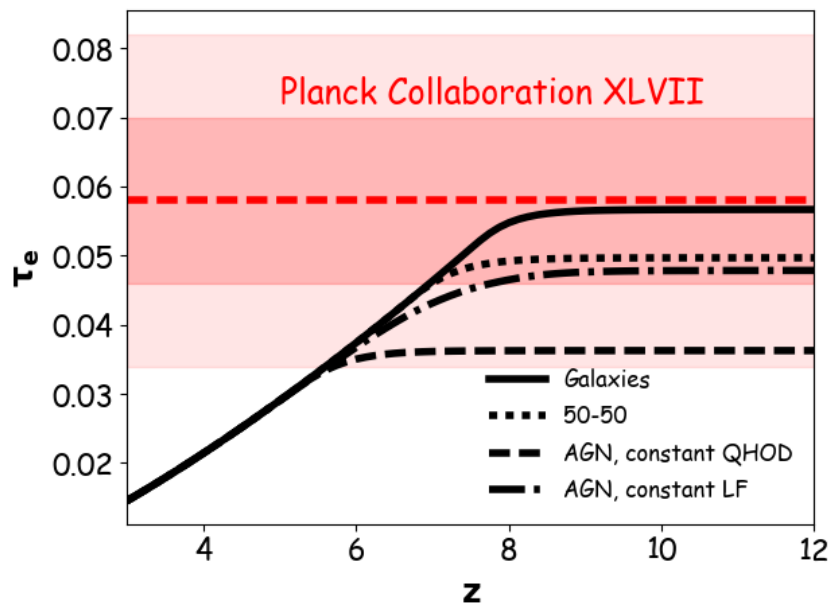
FIGURE 4.5: Thomson scattering optical depth evolution as a function of redshift. The shaded red dark and light areas represent the 1-σ and 2-σ levels of the recent Planck (2016) optical depth measurement whereas the dashed red horizontal line marks the measured *Planck* value ($\tau = 0.058 \pm 0.012$). The Galaxies model (solid) is consistent with the actual optical depth value. The 50-50 and constant LF models obtain a lower optical depth of $\tau \sim 0.049$, matching the lower 1-σ level of planck. Our fiducial constant QHOD AGN models produces a very low optical ($\tau \sim 0.036$) which lies at the lower limit of 2-σ level.

One might question why Madau & Haardt (2015) was able to match these constraints based on the G15 model and thereby argue for purely quasar-driven reionisation, whereas we reach an opposite conclusion. There are two main differences. First, Madau & Haardt (2015) made a rough fit to the ionising emissivity, which resulted in a much flatter redshift dependence than we obtain from our constant QHOD model, more like our constant LF model except higher in amplitude by $\sim \times 2 - 3$ (see Figure 4.2). Indeed, our constant LF model results in an ionising emissivity evolution much like theirs, and is consistent (albeit marginally) with τ_e. Second, Madau & Haardt (2015) purely relied on counting emitted photons, and did not account for an evolving spatially-clustered nature of sinks which absorbs more photons, and hence retards reionisation particularly at early epochs compared to a spatially-homogeneous clumping factor model. These differences result in substantially more neutral gas at early epochs in our model, and lead to strong disagreement with the measured τ_e as well as x_{HI}.

Our 50-50 model can plausibly match the constraints within current 1σ uncertainties. Recall that for our Galaxies model, we previously found $f_{\rm esc} = 0.25^{+0.26}_{-0.13}$, which means that the galaxy contribution alone in the 50-50 model corresponds to an escape fraction that is at the 1σ bound allowed by the MCMC fit. Correspondingly, the predicted τ_e and the redshift of reionisation are near the 1σ-low end of their respective allowed observational ranges.

The Qin et al. (2017) AGN model yields an optical depth of $\tau \sim 0.025$, corresponding to an end of reionisation at $z \sim 3$. Our constant QHOD AGN model would obtain similar results if a magnitude cut-off had been implemented in the ionising emissivity integral to exclude the very faint AGN. Even with our more favorable case of reionisation by AGN, reionisation still occurs very late.

Overall, we find that our constant QHOD model that is constrained to match the AGN emissivity of G15 can adequately match the global ionising emissivity at $z \sim 5$, but strongly fails to reionise the Universe by $z \sim 6$ and produces too low Thomson optical depth. A constant LF model does somewhat better at matching constraints, but the underlying assumption is not physically well-motivated, does not match the observed emissivity evolution from $z \sim 6 \to 4$, and is inconsistent with the self-consistent calculations of Qin et al. (2017). A 50-50 model is still within the allowed bounds of the observations considered here, but any larger contribution from AGN would be disfavoured – and we reiterate that our AGN model is already pushed towards increasing the AGN emissivity as much as possible. Our $x_{\rm HI}$ and τ_e constraints for all these models are listed in Table 1. Our results thus suggest that AGN-dominated reionisation is highly unlikely, and therefore that galaxies dominate the ionising photon budget during the EoR.

4.3.4 EoR topology

We have shown that our AGN-only models are highly disfavoured given current observational data. However, a 50-50 model is still permissible, if only marginally. Clearly, increasing the precision of current measures should in principle enable more stringent constraints on the relative contribution of AGN and star-forming galaxies to reionisation. But we can also appeal to other aspects such as the topology of reionisation in order to discriminate between models. This will be particularly fruitful in the era of 21cm EoR experiments, which will quantify the power spectrum of neutral hydrogen on large-scales. In this section, we discuss the

topology of neutral gas in our various models, and in the following section we will quantify this by forecasting the 21cm power spectrum for upcoming experiments.

We first investigate these models' differences in terms of their ionisation field maps. We choose to compare these models' maps at a fixed neutral fraction, since we have shown in the previous chapter that the 21cm fluctuations are more sensitive to the topology of the ionisation field while the density field contribution is secondary. This then allows us to compare the topology even though the actual redshift where a given ionisation occurs varies substantially between models.

Figure 4.6 shows 2D maps of the ionisation field of all models at different neutral fractions ($x_{\mathrm{HI}} \approx 0.25, 0.5, 0.75$), projected through the entire volume. Note that the redshifts at which this occurs are much later for the AGN-only models, consistent with their late reionisation.

Our Galaxies model shows a range of bubble sizes, with many small bubbles around low-mass galaxies that have low clustering. The largest bubbles towards the end of reionisation span ~ 100 Mpc, in agreement with many previous studies (e.g. Barkana & Loeb, 2004; Furlanetto et al., 2004; Mesinger et al., 2011; Zahn et al., 2011; Iliev et al., 2014; Majumdar et al., 2014). It is clear that there will be significant power on all scales owing to this topology.

The constant QHOD and constant LF AGN models show fairly similar H II bubble sizes and distributions. Compared to the Galaxies case, there are fewer small bubbles owing to the fact that AGN tend to populate more massive halos than the typical galaxy contributing to reionisation in the Galaxies model. However, there are still some small halos hosting small bubbles even in the AGN case. This contrasts with the Kulkarni et al. (2017) AGN model where AGN are assigned only in the massive halos using a circular velocity cut-off, and thus their model does not yield any small-scale H II regions (see their Figure 2). Nonetheless, because the duty cycle of AGN in our model is very low in low-mass halos, many fewer small bubbles are seen compared to the Galaxies case.

For large ionisations, the ionisation maps of the constant QHOD and constant LF AGN models display larger H II regions as compared with those of Galaxies model. This is necessary to compensate for the lack of numerous small bubbles, in order to achieve a similar neutral fraction. This is driven by the strong AGN clustering as suggested by the input G15 LF at its faint end.
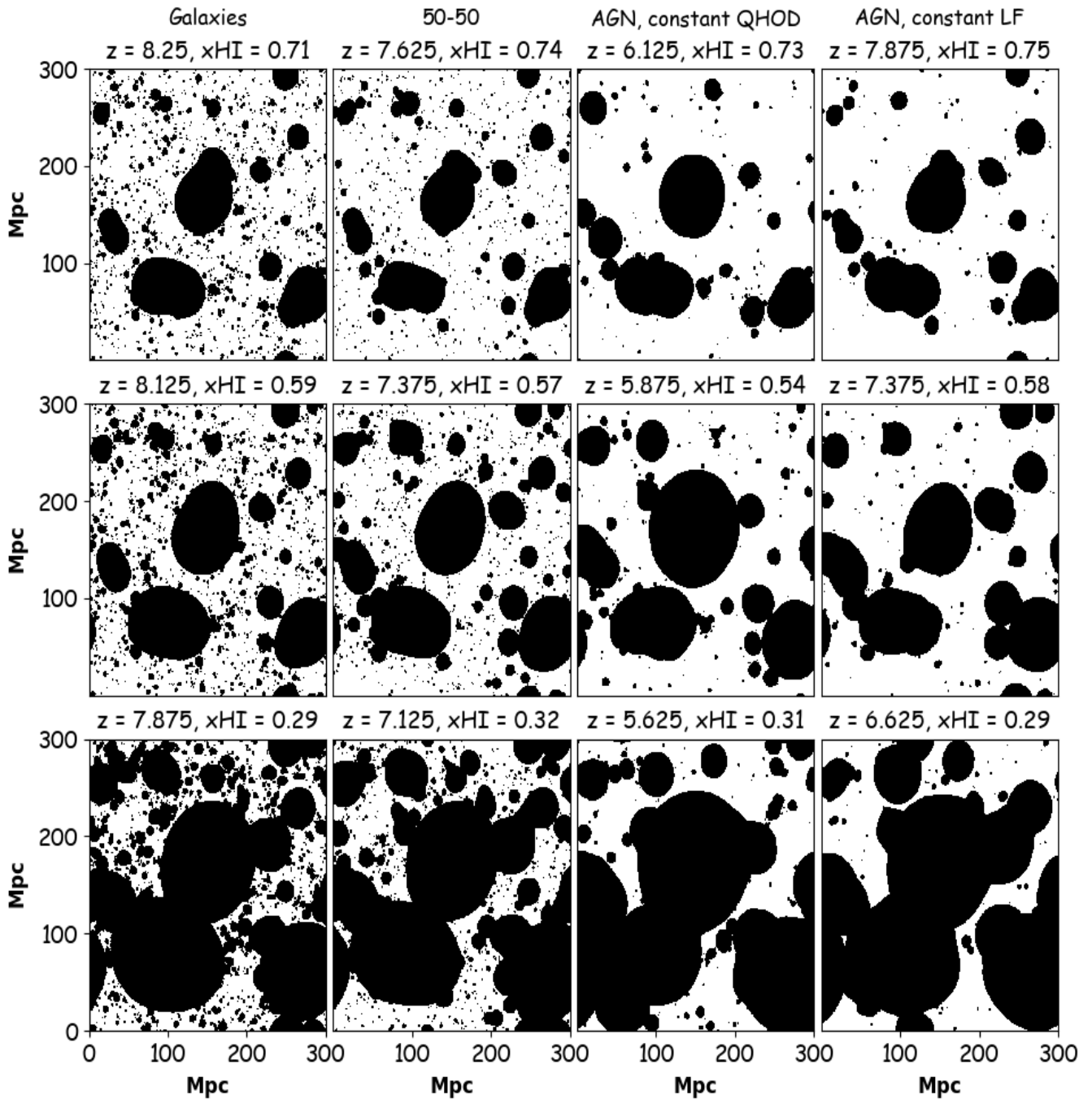
FIGURE 4.6: Slices of the ionisation box each of a size $300 \times 300 \times 0.535$ Mpc^3 from our four models at different stages of reionisation. Top to bottom: $x_{HI} \approx 0.25, 0.5, 0.75$. Left to right: Galaxies, 50-50, constant QHOD, constant LF models. White and black represent neutral and ionised regions respectively. The constant QHOD and constant LF AGN models show large HII bubbles as compared to Galaxies model. The Galaxies and 50-50 models show similar topology, indicating that galaxies play stronger role in determining the HII regions properties. Actual redshifts and neutral fractions are quoted on top of each map.

The 50-50 model is, not surprisingly, intermediate between the Galaxies and AGN-only models. The small bubbles are less prominent owing to the lower $f_{\mathrm{esc},\star}$. The maximum bubble sizes are comparable to but slightly larger than in the Galaxies model. Hence the star-forming galaxies tend to drive the topology even when substantial AGN are present. This comes from the facts that each halo mass bin (magnitude bin) includes fewer AGN than the number of possible hosting halos as implied by the AGN duty cycle estimates (e.g. Shankar et al. 2009), and hence star-forming galaxies would overcome the impact of those fewer AGN on the ionisation field topology. The difference between AGN (constant QHOD and constant LF) and star-forming galaxies (Galaxies and perhaps 50-50) dominated models increases as reionisation proceeds and becomes clear at late stage of reionisation (bottom row for $x_{\mathrm{HI}} \sim 25\%$ of Figure 4.6). We expect these trends to be reflected quantitatively in their 21cm power spectra.

4.3.5 The 21cm power spectrum

Using the ionisation fields of these models at fixed neutral fractions (Figure 4.6), we now compute our key EoR observable, namely the 21cm power spectrum. Assuming that the spin temperature is much higher than the CMB temperature, the 21cm brightness temperature takes the following form:

$$\delta T_b(\nu) = 23 x_{\mathrm{HI}} \Delta \left(\frac{\Omega_b h^2}{0.02} \right) \sqrt{\frac{1+z}{10} \frac{0.15}{\Omega_m h^2}} \left(\frac{H}{H + dv/dr} \right) \mathrm{mK}, \qquad (4.12)$$

where dv/dr is the comoving gradient of the line of sight component of the peculiar velocity. Using this equation, it is straightforward to create the 21cm brightness temperature boxes from which we compute the 21cm power spectrum as follows: $\Delta_{21}^2 \equiv \mathrm{k}^3/(2\pi^2\,\mathrm{V}) < |\delta \mathrm{T_b(k)}|_{\mathrm{k}}^2 >$.

In top panels of Figure 4.7, we show a comparison between our models' predicted 21cm power spectrum, as well as with the AGN-dominated models of Kulkarni et al. (2017). Bottom panels show the ratio of each model 21cm power spectrum to the Galaxies model, in order to clearly display the models differences as a function of the scale k. Consistent with the ionisation maps (Figure 4.6), the Galaxies model has less power than the AGN-only models, which at a fixed x_{HI} are themselves rather similar. This shows that the 21cm power spectrum is somewhat insensitive to the method by which we populate AGN (constant QHOD versus constant LF),
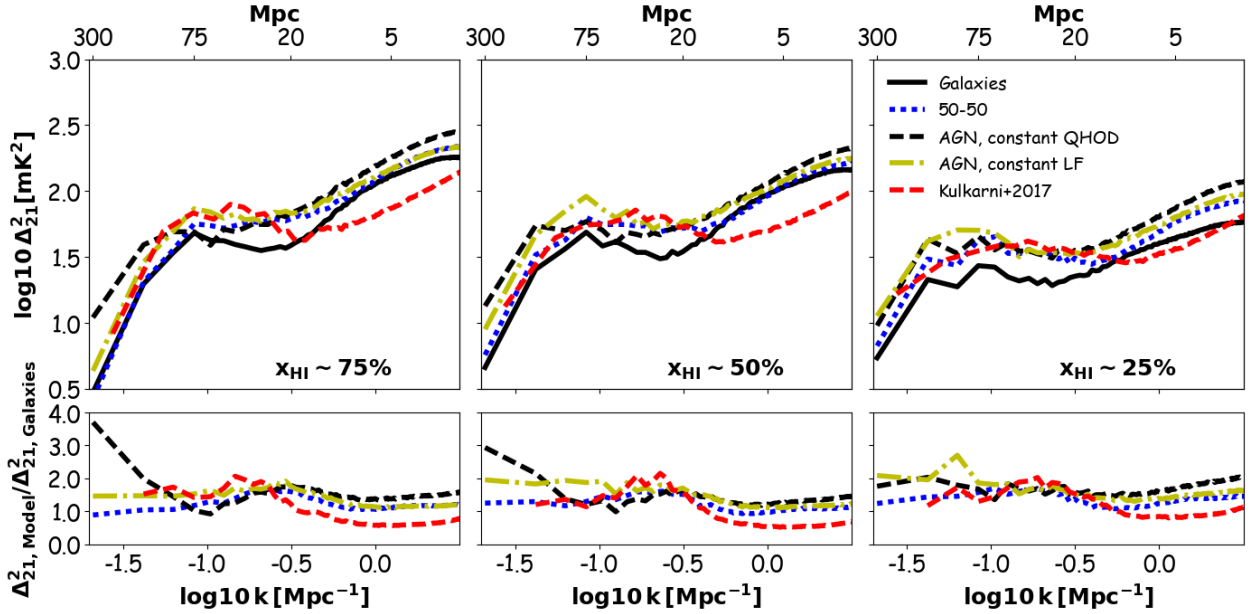
FIGURE 4.7: Top: the 21cm power spectrum comparison between all models at fixed neutral fractions. We also compare to the recent AGN model developed by Kulkarni et al. (2017) (dashed red). The Galaxies (black solid) and 50-50 (dotted blue) models produce similar power spectra on small and large scales, particularly at intermediate ($x_{HI} \sim 0.5$) and early ($x_{HI} \sim 0.75$) stages of reionisation. Likewise, the constant QHOD (dashed black) and constant LF (dot-dashed yellow) AGN models yield similar power spectra. The AGN models produce power spectra that is higher by a factor of $\sim \times 1.5-2$ than the Galaxies model. The power spectra obtained by Kulkarni et al. (2017) AGN model agree with our AGN models relatively on large scales but they are lower by a factor of $\sim \times 2-2.5$ on small scales, due to these models' differences in populating AGN into halos (see text for details). Bottom: the ratio of each model power spectrum to that of Galaxies as function of the scale k, which shows the difference between each model to Galaxies.

even though there is a clear difference in the reionisation histories due to differences in the ionising emissivity evolutions (see Figures 4.3 & 4.4). Relative to the Galaxies case, at early epochs the differences with the AGN-only models peaks at intermediate scales (k $\sim 0.3 - 0.1$), typical of the AGN bubble sizes. At later epochs, however, there is not much scale dependence to the variation, and the AGN models are simply about a factor of $1.5 - 2\times$ higher than the Galaxies model, owing to the stronger clustering of G15 AGN observations. The 50-50 models yield similar 21cm power spectra both on small and large scales to the Galaxies case at the early ($x_{HI} \sim 0.75$) and intermediate ($x_{HI} \sim 0.5$) stages of reionisation. This confirms our previous finding that star-forming galaxies are dominant in determining the ionised regions properties and hence their associated 21cm fluctuations during the early stages of reionisation. At later stages, there is an increasing difference between the 50-50 model and the Galaxies case, owing

to the increased contribution of AGN at later epochs. Hence it may be optimal to look at the latter stages of reionisation in order to obtain more quantitative constraints on the fractional contribution of AGN.

Our AGN models agree with the Kulkarni et al. (2017) AGN model reasonably well for the large-scale 21cm power spectrum, while their small scale power is suppressed by a factor of $\sim \times 2 - 2.5$ relative to ours. As mentioned before in §4.3.4, our AGN model yields small-scale ionised regions owing to populating AGN randomly at all halo mass bins (magnitude bins) into their hosting halos using the actual number of AGN as suggested by the G15 LF observations, as opposed to a unity duty cycle in massive halos in the Kulkarni et al. (2017) AGN model. By constraining our LF to that observed, our AGN model predicts a non-unity duty cycle, which occasionally populates small halos with AGN and thus boosts the 21cm power spectrum on small scales.

4.3.6 Forecasting 21cm power spectra to constrain AGN models

Our work has shown that AGN driven-EoR models are photon-starved, in agreement with many others, and as such plausible AGN models are unlikely to fully drive reionisation. Nonetheless, a substantial AGN contribution such as in our 50-50 model is still allowable given current data, which begs the question, will future 21cm data provide more stringent constraints on the contribution of AGN to reionisation?

To answer this question, we focus our analysis on three different low-frequency radio interferometer designed to measure the 21cm EoR power spectrum: the Low Frequency Array (LOFAR)[1], the Hydrogen Epoch of Reionisation Array (HERA)[2], and the Square Kilometer Array (SKA-Low)[3].

To forecast the power spectra for these facilities, we use the same recipe presented in the previous chapter, outlined as follows: We first select the redshift (observed frequency) at which we compute the 21cm power spectrum for each model. To establish a proper comparison, we operate these three array designs, with parameters summarized in Table 4.2, in a drift-scanning mode for 6 observing hours per

---

[1]http://www.lofar.org/
[2]http://reionization.org
[3]https://www.skatelescope.org

Experiment	Design of antennae	Diameter [m]	Collecting area [m^2]	Receiver temperature [mK]
LOFAR	48 tiles of bow-tie high band	30.75	35,762	$T_{sky} + 140,000$
HERA	331 hexagonally packed	14	50,953	$T_{sky} + 100,000$
SKA	866 compact core	35	833,189	$100\ T_{sky} + 40,000$

TABLE 4.2: Summary of parameters used in 21cmSense package to obtain the thermal noise sensitivity for each experiment. Columns (from left to right) are: experiments' names, designs, antenna diameter, total collecting area, and the reciver temperature. The sky temperature is given by $T_{sky} = 60\lambda^{2.55}$ K.

day for 180 days at 8 MHz bandwidth. We then add the total uncertainty which includes the thermal noise and sample variance using the 21cmSense[4], a package for calculating the sensitivity of 21cm experiments to the EoR power spectrum. We refer to Parsons et al. (2012) for basics of the radio interferometer sensitivities, to Pober et al. (2013, 2014) for more details on observation strategies and foreground removal models, and to chapter 3 for the experiments designs and configurations. We only change the foreground removal method to use the optimistic model developed in Pober et al. (2014) in which the foreground wedge extends to the Full-Width Half-Max (FWHM) of the experiments' primary beam. This will extend our analysis to cover more large scales than using a moderate model in which foreground wedge extends only to 0.1 h Mpc^{-1} beyond horizon limit.

From Figure 4.7, we notice that the large variations between the Galaxies and constant QHOD AGN models occurs at the late stages of reionisation ($x_{HI} \sim 25\%$) when the HII bubbles begin to overlap. We thus create our 21cm mock observations at these epochs. Since the reionisation occurs very late in the constant QHOD AGN model (see Figure 4.4), we re-tune the model (using $A = 1.25 \times 10^7$, which we note would substantially overproduce the ionising emissivity constraints) to match the optical depth as obtained by Galaxies model. We then perform our 21cm mock observations at $z = 8$ and $x_{HI} \sim 0.3$ for both models in order to conduct a comparison at the same redshift and neutral fraction.

Figure 4.8 shows a 21cm mock observation comparison at z=8 ($x_{HI} \sim 0.3$) between Galaxies and the re-tuned constant QHOD AGN models. The shaded area shows the total uncertainties (1-σ level) expected from the experimental designs summarised in Table 4.2 using the 21cmSense package. The vertical lines mark the scale at which the 1-σ errorbars from a specific experiment overlap, corresponding to the sensitivity limit for each experiment where the models can be distinguished.

---

[4]https://github.com/jpober/21cmSense
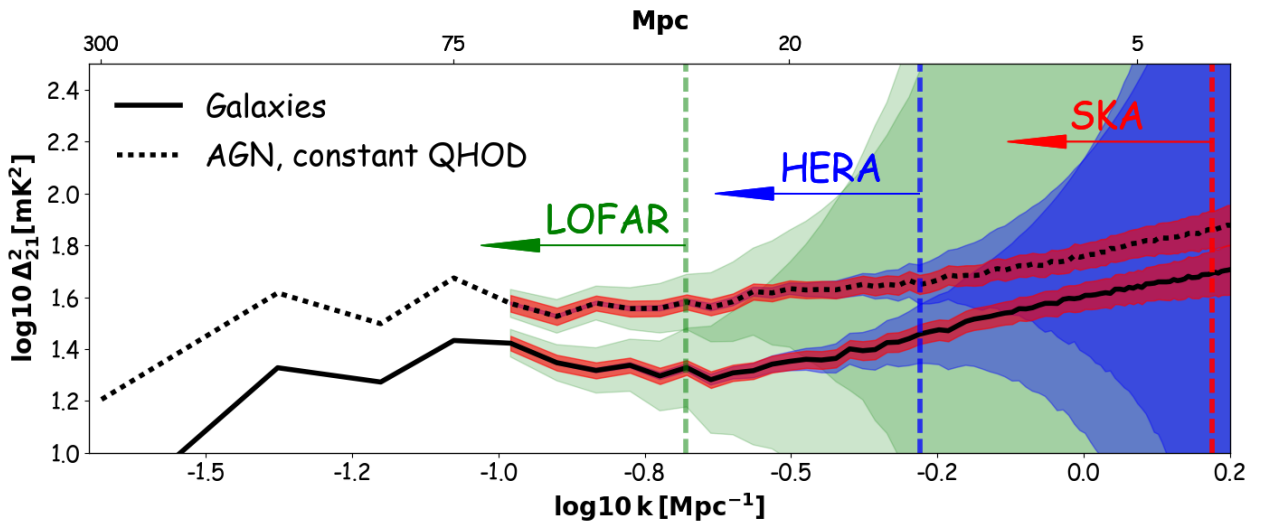
FIGURE 4.8: Mock 21cm EoR power spectrum observations using the same telescope designs and configurations at z = 8 and $x_{HI} \sim 30\%$ from our Galaxies (black solid) and constant QHOD AGN (black dashed, tuned to match Galaxies model optical depth τ) models. Shaded areas show the 1-σ erorrbars obtained using 21cmSense package for our constructed EoR arrays: SKA (red), HERA (blue), LOFAR (green). Vertical dashed lines represent the scale at which a specific experiment may distinguish between these models (the scale at which errorbars overlap from a specific experiment). Future 21cm observations by these experiments will be able to discriminate between these models at their corresponding sensitivity limits.
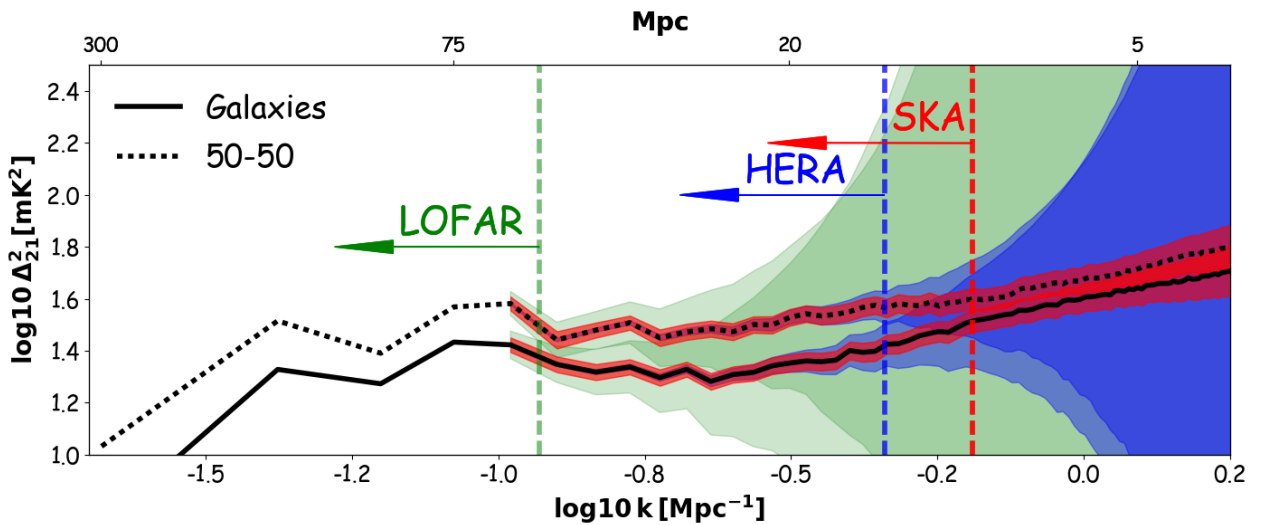
FIGURE 4.9: Mock 21cm EoR power spectrum observations using the same telescope designs and configurations at z = 8 and $x_{HI} \sim 30\%$ from our Galaxies (black solid) and 50-50 (black dotted, tuned to match Galaxies model optical depth τ) models, similar to Figure 4.8. Only future 21cm observations by HERA and SKA will be able to discriminate between these models at their corresponding sensitivity limits.

Given that it can only probe relatively large scales, LOFAR will have some difficulty discriminating between the Galaxies and constant QHOD models, as they lie within ~ 2-σ of each other. However, HERA should be able to distinguish between these models rather well on scales above about 10 Mpc, and the larger baselines of SKA-low will enable discrimination to significantly smaller scales. From Figure 4.8, we see that LOFAR, HERA, and SKA can discriminate between these models during the latter stages of reionisation at scales of $k < 0.21$ Mpc^{-1} (> 30 Mpc), $k < 0.53$ Mpc^{-1} (> 12 Mpc) and $k < 1.66$ Mpc^{-1} (> 4 Mpc), respectively.

The fact that HERA and SKA can easily discriminate AGN-only and Galaxies-only models suggests that it may be possible to constrain the fractional contribution of AGN using such data. We thus repeat the same steps above, except now for the 50-50 model, tuned to match Galaxies τ_e.

Figure 4.9 shows a forecasting comparison between the Galaxies and 50-50 models. Since the 50-50 model yields 21cm power amplitude that is closer to Galaxies than constant QHOD model does, the scales at which experiments overlap are shifted towards large scales (compare vertical dashed lines in figure 4.8 versus 4.9). This shows that LOFAR is unlikely to discriminate between these models, unless a very optimistic foreground removal is applied to detect the signal on large scales ($k < 0.12$ Mpc^{-1} (> 53 Mpc)), which are highly contaminated by foregrounds (Pober et al., 2014). Given a successful foreground removal, HERA and SKA can discriminate between the Galaxies and 50-50 models during the latter stages of reionisation at scales of $k < 0.46$ Mpc^{-1} (> 14 Mpc) and $k < 0.65$ Mpc^{-1} (> 10 Mpc), respectively as shown by vertical dashed lines in Figure 4.9.

Note that we have shown 1-σ uncertainties, which is unlikely to be sufficient to robustly discriminate between Galaxies and AGN models. If one instead requires 3-σ to distinguish between the models, then LOFAR fails to distinguish between our models, but HERA and SKA are still successful albeit on scales somewhat larger than those obtained with the 1-σ limit.

Figure 4.8 & 4.9 both illustrate how future 21cm observations could potentially help constrain the nature of the source population. While current observations cannot rule out the 50-50 model, in principle HERA and SKA should be able to do so straightforwardly, assuming they can reach their target sensitivities. Until these facilities come online, ancillary observations will continue to improve. Hence comprehensive models that are able to make predictions for, and constrain

to, a wide variety of EoR data are vital for optimizing the scientific information extracted from future observations including 21cm data.

4.4 Conclusion

We have presented predictions for the 21cm power spectrum arising from AGN-driven reionisation models, and contrasted them with predictions from galaxy-driven models and models with a mixture of sources. The AGN source population is placed into galaxy halos using a physically motivated prescription based on the G15 AGN observations, deriving a Quasar Halo Occupancy Distribution of AGN at $z = 5.75$ from this and using it to evolve the number of AGN to higher redshifts. This framework is implemented into our Time-integrated version of SIM-FAST21, which self-consistently accounts for recombinations and the evolution of structure. We have calibrated these AGN models to reproduce ionising emissivity constraints, and compared them with models in which ionising radiation is dominated by star-forming galaxies. Our key findings are as follows:

- When tuned to match the G15 ionising emissivity constraints, AGN-only models produce very late reionisation at $z \ll 6$ (Figure 4.4). If we assume a constant halo occupancy for AGN as is consistent with other observational constraints and models, then the predicted Thomson optical depth is only 0.036, well below Planck constraints (see Figure 4.5). This strongly disfavours AGN as providing the dominant source for reionising photons.

- We determine a quasar halo occupancy distribution (QHOD) that is near unity for very massive halos, but drops to sub-percent level for more typical halos. This is directly interpretable as a duty cycle for AGN. This also explains why reionisation is so late in this AGN-only model, because AGN populate massive halos more frequently and hence their emissivity contribution grows strongly only at late epochs (Figure 4.3), thereby not ionising enough volume to match the optical depth measurements.

- Our results are consistent with those from the AGN-only models by Qin et al. (2017) using the DRAGONS semi-analytic models, who also found that AGN could not dominate reionisation. Our Galaxies model is also in broad

agreement with their full model, supporting their result that star-forming galaxies can provide sufficient photons as a function of redshift to reionise.

- A model where we assume a constant AGN luminosity function at $z \geq 5.75$ can barely match the Planck τ_e, but still reionises very late, and moreover it is not physically well motivated and disagrees with the measured evolution of the AGN luminosity function at $z \sim 4 - 6$ (Giallongo et al., 2015). It does, however, result in a global emissivity evolution similar to that assumed in Madau & Haardt (2015), but even in this case we do not confirm their result that such a model is viable, likely because we include the effects of recombinations along with a more sophisticated accounting of the clustering of sources and sinks.

- Our AGN-only model produces larger HII bubbles as compared with our Galaxies-only model (see Figure 4.6), consistent with results from another semi-numerical model by Kulkarni et al. (2017) (Figure 4.6). This results in a larger 21cm power spectrum amplitude by $\sim \times 1.5 - 2$ as compared with that from the galaxies-only model (see Figure 4.7).

- We examine a model which includes a 50% contribution from galaxies and AGN (assuming a constant QHOD). We find that this model can barely satisfy current τ_e and x_{HI} constraints. At early epochs, the galaxies contribution dominates the power spectrum, but during the latter stages of reionisation the quasars contribution is more significant, and the power spectrum deviates more substantially from the galaxies-only case.

- Future 21cm observations by LOFAR, HERA and SKA can discriminate between the constant QHOD AGN and Galaxies models during late reionisation at scales of $k < 0.21 \ \mathrm{Mpc}^{-1}$ ($> 30 \ \mathrm{Mpc}$), $k < 0.53 \ \mathrm{Mpc}^{-1}$ ($> 12 \ \mathrm{Mpc}$) and $k < 1.66 \ \mathrm{Mpc}^{-1}$ ($> 4 \ \mathrm{Mpc}$), respectively (see Figure 4.8). HERA and SKA will also be able to distinguish between our 50-50 and galaxies-only models, and thus potentially constrain the fractional contribution of AGN to reionisation.

- We have assumed an optimistic model for the AGN photon output rate by extrapolating to very low luminosities ($M_{1450} > -18$). There are also suggestions that G15 over-estimates the number of high-z AGN and thus their total emissivity (e.g. Parsa et al., 2017). In either scenario, our claim that AGN cannot dominate reionisation is further strengthened.

It might still be possible that our AGN-only models could match all EoR observations simultaneously, if we relax some of these models' assumptions. For instance, our AGN-only models depend on two parameters, namely, the photon escape fraction $f_{\rm esc,AGN}$ and the black hole formation efficiency A (see Equation 4.4). These results are already obtained using 100% $f_{\rm esc,AGN}$, and it is clear that those models would reionise much earlier if we adopt $f_{\rm esc,AGN} \gg 100\%$, which is not physical. The A parameter has been tuned to allow these models to reproduce the G15 data at z=5.75. If we choose not to calibrate these models to match the G15 data, we then can adopt larger A which results in a smaller QHOD and earlier reionization. For example, the QHOD in the most faint magnitude bin at z=5.75 decreases from $\sim 2.7\%$ to 1.7% as the A increases from 5×10^5 to 10^6. This shows that allowing the AGN-only models to form more efficient black holes (large A) result in a fewer number (less QHOD) of them since the QHOD quantifies the fraction of active halos with AGN. From Figure 4.4, we see that the reionization in the constant LF AGN model (with $A = 10^6$) starts earlier than in the constant QHOD AGN model (with $A = 5 \times 10^5$), but because there is no evolution in the source population (fixed LF), the model reionises much later than the constant QHOD. It is then clear that if we adopt larger A to form more effeicent black holes, our AGN-only models will yield an early reionization. In this case, these models might produce consistent reionization histories and optical depths as compared with the observations. Given the large uncertainties in the ionising emissivity measurements by G15 and Becker & Bolton (2013), these models might still be consistent with these measurements' 2-σ level at $A > 10^6$. We expect that the AGN clustering remains unaffected at a specific neutral fraction for larger A values and hence the future 21cm observations can still discriminate between our AGN-only versus Galaxy-only models. The AGN-only models also assume that $M_{\rm bh} - v_{\rm cir}$ correlation (Equation 4.4) is valid even at high redshifts. This adds more uncertainties since such a correlation has only been measured in the local universe. More physically motivated and self-consistent AGN modelling at high redshift is clearly required to understand their formation and evolution as a function of redshift. Analogously to our stellar source model, one may allow the black hole emissivity to scale super-linearly with black hole mass ($R_{\rm ion,AGN} \propto M_{\rm bh}^C$). This new parameter C would indeed affect the AGN clustering and the corresponding ionised bubble sizes, as previously seen in our star-forming galaxies models ($R_{\rm ion,\star} \propto M_{\rm h}^C$). We leave investigating this dependence for future works.

Improved high redshift AGN observations are clearly desirable in order to more robustly determine the AGN luminosity function, particularly at the low-luminosity end. The results of such observations can be incorporated straightforwardly into the framework we have presented here, and will provide better constraints on the contribution of AGN to reionisation. Our framework illustrates that the QHOD is an effective approach to evolve the number of AGN during the EoR. Our analysis indicates that despite there being potentially more faint AGN than previously believed, star-forming galaxies still dominate the neutral gas topology and ionising photon budget.

D'Aloisio et al. (2016), Mitra et al. (2016), and Oñorbe et al. (2017) have all independently demonstrated that AGN-only models overheat the IGM, inconsistent with Ly-α temperature measurements (Becker et al., 2011), due to the early onset of He II reionization. Finlator et al. (2016) further have shown that these models also over-ionise the metals when compared with observed metal absorption line measurements (D'Odorico et al., 2013). Our findings corroborate these results via a different approach.

AGN could still be important for reionisation because of their long-range heating effects owing to their harder emission spectrum, as well as for setting the shape of the metagalactic ionising flux that is important for interpreting metal-line absorption data (e.g. Finlator et al., 2016). Early AGN are in and of themselves interesting in order to understand the emergence of supermassive black holes particularly at early epochs. Our results here suggest that future 21cm experiments will have a key role to play in constraining the amount of AGN activity and its contribution to the metagalactic flux during the EoR.

Chapter 5

Conclusion

This thesis aims at extending and improving on the underlying astrophysics implemented in the standard semi-numerical models (e.g. SimFast21 written by Santos et al. (2010)) in order to provide more accurate and refined predictions of the 21cm signal from cosmic reionization for future radio interferometer experiments. Semi-numerical models usually neglect various astrophysical effects and perform only rough approximations of the sub-kpc scale astrophysics in order to generate coarse realizations of the ionization and 21cm fields on large cosmological scales with extremely minimal computational expenses. The central aim here is to improve on these approximations while keeping the simulation computationally efficient. The large uncertainties in these models are represented in the physical treatment of ionising source and sink populations during cosmic reionization. We have implemented new physically motivated recipes, to model the properties and evolution of ionising source and sink populations, that are taken from high-resolution radiative transfer simulations in order to account for the non-linear dependence on halo mass, redshift and environment. We have developed a robust parameter estimation pipeline in order to translate current reionization observables into constrains on the improved model astrophysical parameters and perform 21cm forecasting for future experiments. We finally have implemented a new model to populate and evolve AGN in the semi-numerical models in order to estimate the contribution of different ionising source populations to cosmic reionization. A summary of our main key findings in each chapter is provided next.

Chapter 1 presents a brief overview of cosmic reionization, observational constraints, and theoretical models of reionization with a focus on semi-numerical

models used in this thesis, in order to model cosmic reionization and its redshifted 21cm fluctuations on large cosmological scales.

Chapter 2 highlights the big problems encountered in simulating the 21cm signal using the standard semi-numerical models, and describes the new method by which we propose to solve these problems into more details. These problems include the use of a constant efficiency parameter ζ to model ionising photons from dark matter halos and identify the ionised regions without explicitly accounting for recombinations. To overcome these problems, we have obtained new derived parametrizations of the non-linear ionization R_{ion} and inhomogeneous recombination R_{rec} rates from our high-resolution radiative transfer simulations (Finlator et al., 2015) and larger volume hydrodynamical simulations (Davé et al., 2013), in order to identify the ionized regions more accurately, instead of using the standard ζ approach. These parametrizations provides an unique way to connect the small-scale astrophysics with large scale cosmology. The new version of SimFast21, with R_{ion}-R_{rec} approach, is able to simultaneously reproduce various reionization constrains (optical depth τ, ionising emissivity $\dot{N}_{\mathrm{ion}}$, and neutral fraction x_{HI} by end of reionization) with only 4% photon escape fraction f_{esc}. The R_{ion} boosts the 21cm power spectrum on small scales while R_{rec} suppresses the large scale 21cm power spectrum by a factor of $\times 2-3$ as compared with the vanilla SimFast21. Our key findings show the importance of accurately treating ionising photon source and sink populations during reionization in order to provide more accurate predictions for future 21cm surveys.

Chapter 3 further extends our improved SimFast21 version to modify the previously implemented instantaneous criterion in order to account for time-integrated effects by comparing the actual number of photons to that of recombinations, in addition to the neutral hydrogen atoms from partially ionised regions following the reionization history. This new model yields larger H II regions and a more sudden reionization, leading to an order of magnitude 21cm power enhancement on large scales. We then have developed a more flexible and robust MCMC parameter estimation pipeline in order to constrain the model's astrophysical parameters against several reionization observations, instead of hand-tuning our free parameters. We also have generated several redshifts 21cm Mock observations to test the capability of future 21cm observations (LOFAR, HERA, SKA) to constrain our free parameters. We have found that future 21cm observations alone will provide tighter constraints on the astrophysical parameters than a combination of the

current reionization observations (SFR, τ, $\dot{N}_{\mathrm{ion}}$). Our key findings indicate that future 21cm surveys will play a leading role in constraining the ionising sources contribution and evolution.

Chapter 4 presents a detailed discussion on the ongoing debate of AGN versus galaxies reionization scenarios. To participate in this debate, we have developed a new method to populate AGN in the semi-numerical modelling framework. Our new method improves on previous efforts by accounting for the quasar duty cycle to obtain the AGN number density at a given magnitude bin and evolving AGN to higher redshifts assuming a fixed Quasar Halo Occupancy Distribution based on recent Giallongo et al. (2015) observed luminosity functions. We have found AGN-dominated reionization scenario cannot simultaneously reproduce current reionization observations. AGN-only models produces larger ionized regions and 21cm power spectrum as compared with galaxies-dominated scenarios. We have also illustrated how future 21cm observations can potentially discriminate between these two scenarios and constrain different ionising sources contribution to cosmic reionization. Our key findings suggest that AGN are highly unlikely to drive cosmic reionization.

5.1 Current and Future Works

5.1.1 SimFast21-RT

Semi-numerical models are known to violate the photon number conservation (as shown in Chapter 3) due to the excursion set formalism which identifies only fully ionized regions. This can be solved by applying the actual radiative transfer equations which allows tracking partial ionizations. This new radiative transfer routine is currently under development in which I assume a mean free path with a super-cell optimization to reduce the computational costs. I am currently testing the ability of SimFast21-RT to successfully pass the standard radiative transfer tests (e.g. Iliev et al., 2006) such as the single isothermal H II region expansion in a uniform medium and the multiple source expansion in a cosmological density. The results of this RT routine will eventually be submitted to a Peer-reviewed journal.

5.1.2   Reionization Models Classifier using 21cm Map Deep Learning

Next-generation observations with the LOFAR, HERA and SKA will provide a large amount of excellent images of reionization on large cosmological scales. An intrinsic key challenge for theoretical models of reionization lies in the ability to handle such a large amount of data more efficiently. Although the semi numerical models are extremely fast to run as compared to radiative transfer simulations, nevertheless they are still slow for future big data era. Fastest semi-numerical run with a reasonably large box size (~ 100 Mpc) spends few minutes to obtain the 21cm predictions. However, applying machine learning techniques has shown a dramatic cost reduction in computational expenses (e.g. Kern et al., 2017; Schmit & Pritchard, 2017). With these techniques, the running wall-time from few minutes can be reduced to few seconds, and hence providing more suitable tools to manage the huge output expected from future 21cm observations.

Although the 21cm power spectrum is powerful in quantifying the small and large scales ionised bubbles, the actual 21cm field (2- or 3-dimensions) will contain more information than the power spectrum (1-dimension), and hence providing an alternative way to constrain the contribution of different reionizing source populations to cosmic reionization (similar to Chapter 4 when using the 21cm power spectrum to distinguish between AGN-only versus galaxy-only models). The aim here is to employ machine learning techniques using Convolutional Neural Network to build up reionization models classifier to discriminate between 21cm maps as produced by AGN-only versus Galaxies-only models. I have successfully created a network that is efficiently able to discriminate between these models in the presence of a realistic simulated noise from different experiments, but using the same underlying density field. I am currently testing the capability of this classifier to discriminate between these models when the density field is different by changing the initial seed for density fluctuations. The results of this classifier will eventually be submitted to a Peer-reviewed journal.

5.1.3 Linking SimFast21 to Galaxy Formation Semi Analytical Models

The key findings in this thesis strongly indicate that the 21cm signal is highly sensitive to the physical treatment of ionising source model. I here propose to take a step further to link the improved version of SimFast21 to a Semi-Analytic Model (SAM) for co-evolution of galaxies, black holes and AGN (Somerville et al., 2008), that has been shown to reproduce wide range of observations at low and high redshifts. With this approach, one can naturally and simultaneously track the growth of black holes, metallicities, star formation rates, heating effects, and galaxies emission/absorption lines spectra through the merger history. The merger histories will enable self-consistent calculations of ionising emissivities as produced by different source models. Following the merger histories, the SAM will open the window to study the nature of ionising sources at the beginning of reionization and cosmic dawn. Therefore, I expect that the ionising emissivity calculations will be more accurate and account for the local fluctuations as a function of the environment. However, the wealth of information provided by the SAM on SimFast21 cosmological dynamic range will be suitable to address several problems during reionization and in galaxy formation. Future projects with this new model will include providing new improved 21cm predictions, studying implications on the EoR observables, extracting new constraints on the astrophysical parameters, generating several line-intensity mapping for CII, CO, OIII and Ly- , and studying galaxies and AGN luminosity functions at high-redshift.

5.2 Future prospects

This thesis provides several theoretical developments that are important for current and future reionization observational efforts. It begins with disentangling the various complex astrophysical processes, that are usually combined and quantified with a single efficiency parameter ζ, into a set of astrophysical parameters to *directly* quantify the photon escape fraction, dependence on mass, redshift and environment, separating the models of ionising source (R_{ion}) and sink (R_{rec}) populations. It also presents a robust and more flexible parameter estimation pipeline to constrain this set of parameters against current and future reionization observations. Finally, it introduces an AGN source model to test the ability of different

source populations to complete reionizations. In all aspects, it is evident that future 21cm observations will provide the most tight constraints on reionization astrophysical parameters (see Chapter 3 and Greig & Mesinger, 2015, for similar analysis and conclusions).

However, all reionization 21cm experiments encounter many challenges and systematics (e.g. foregrounds, ionosphere, and sky model assumption) that contribute to the excess noise. While these challenges persist, several groups have already published their first upper limits on the 21cm power spectrum including the LOFAR (Patil et al., 2017), the Giant Metrewave Radio Telescope (GMRT, Paciga et al., 2013), the Murchison Widefield Array (MWA, Beardsley et al., 2016), and the Precision Array for Probing the Epoch of Reionization (PAPER, Ali et al., 2015). All these upper limits are associated with large uncertainties and more than $1-2$ order of magnitudes as compared to current theoretical predictions (see also Kulkarni et al., 2016). The observational efforts of these precursor and pathfinder experiments are essential to improve the main telescope designs of future HERA and SKA experiments in order to obtain more accurate measurements. It is likely that AGN-only models might be the first scenarios to be ruled out by future 21cm surveys, due to their larger 21cm signal as compared with galaxy-only models (see Chapter 4 and Kulkarni et al., 2017, for a similar conclusion).

Other indirect probes of reionization (e.g. CMB, high-redshift quasars and galaxies) are also crucial in order to obtain additional constraints on reionization scenarios, source populations and their astrophysical parameters. From Chapter 3, it is clear that the parameter estimation results can be significantly improved, if more accurate measurements, with smaller errorbars, are provided by current reionization experiments. The current uncertainties of various reionization observables (e.g. SFR, τ, $\dot{N}_{\mathrm{ion}}$, x_{HI}) are very large which easily allows several reionization scenarios with wide range of parameters. For instance, one single observation (e.g. τ or $\dot{N}_{\mathrm{ion}}$) alone can poorly constrain the ionising source parameters. In addition, there is a tension on the astrophysical parameters when calibrating the model to reproduce observational constraints during reionization (e.g. SFR and τ) versus post-reionization era (e.g. $\dot{N}_{\mathrm{ion}}$). The SFR and τ constraints require more ionising photon output from massive halos whereas $\dot{N}_{\mathrm{ion}}$ constraint requires only fewer. More refined measurements of these observables at higher redshifts are clearly desirable to connect the different stages of reionization.

Besides future 21cm observations, the future ultra-deep near-infrared surveys by the James Webb Space Telescope (Webb)[1] will enable direct detection of the source population at every epoch in the history of the universe, including the first stars, galaxies and black holes that are important for cosmic reionization. These observations will also reveal the nature of sources responsible for reionization, in terms of their properties (e.g. mass and luminosity), thereby improving our understanding of cosmic reionization.

The theoretical tools developed in this thesis already enabled transforming the current observational uncertainties into direct constraints on a set of astrophysical parameters that prescribe the source population properties and evolution during reionization. These developed tools are also flexible to incorporate newly improved data from next decade observations in order to ultimately set tigher constraints on the astrophysical parameters, and hence narrowing the range of possible different scenarios of cosmic reionization.

---

[1]https://jwst.nasa.gov/

Bibliography

Ali, Z. S., Parsons, A. R., Zheng, H., et al. 2015, ApJ, 809, 61

Akeret J., Seehars S., Amara A., Refregier A., Csillaghy A., 2013, Astronomy and Computing, 2, 27

Anderson L., Governato F., Karcher M., Quinn T., Wadsley J., 2013, MNRAS, stx709

Barkana, R. & Loeb, A. 2001, Phys. Rep., 349, 125

Barkana, R. & Loeb, A. 2004, ApJ, 609, 2, 474

Bauer, A., Springel, V., Vogelsberger, M., Genel, S., Torrey, P., Sijacki, D., Nelson, D., Hernquist, L., 2015, MNRAS, 453, 3593.

Beardsley, A. P., Morales, M. F., Lidz, A., Malloy, M., Sutter, P. M., 2015, ApJ, 800, 128.

Beardsley, A. P., Hazelton, B. J., Sullivan, I. S., et al. 2016, ApJ, 833, 1

Becker, Robert H.; Fan, Xiaohui. et al 2001, AJ, 122, 2850.

Becker G. D., Bolton J. S., Haehnelt M. G., Sargent W. L. W.,2011, MNRAS, 410, 1096

Becker, G. D., Bolton, J. S. 2013, MNRAS, 436, 1023

Becker, G. D., Hewett, P. C., Worseck, G., & Prochaska, J. X. 2013, MNRAS, 430, 2067

Becker, G. D. et al., 2015, MNRAS, 447, 3402

Behroozi, P. S., Wechsler, R. H., Conroy, C., 2013, ApJ, 770, 57.

Berlind A. A. et al, 2003, ApJ, 593,1

138

Bian, F., Fan, X., McGreer, I., Cai, Z., Jiang, L., 2017, ApJL, 837, 1

Bolton J. S., Haehnelt M. G., 2007, MNRAS, 382, 325

Bond, J. R., Cole, S., Efstathiou, G., Kaiser, N., 1991, ApJ, 379, 440

Bouwens J. R., Illingworth D. G., Oesch A. P., Trenti M., Labé I., Bradley L., Carollo M., Van Dokkum G. P., Gonzalez V., Holwerda B., Franx M., Spitler L., Smit R., Magee D., 2015, ApJ, 803, 34.

Bouwens, R. J., Illingworth, G. D., Oesch, P. A., et al., 2015, ApJ, 811, 140.

Chabrier G., 2003, PASP, 115, 763

Choudhury T. R., Haehnelt M. G., Regan J., 2009, MNRAS, 394, 960

Choudhury T. R., Ferrara A., 2005, MNRAS, 361, 577.

Chardin J. et al., 2015, MNRAS, 453, 2943

Chardin J., Puchwein E., Haehnelt G. M., 2017, MNRAS, 465, 3429

Ciardi, B. & Ferrara, A., 2005, Space Sci Rev, 116, 625.

D'Aloisio A., Upton Sanderbeck, R. P. et al, 2016, MNRAS, 468, 4691

D'Odorico, V., Cupani, G., Cristiani, S., et al. 2013, MN-RAS, 435, 1198

Davé, R., Katz, N., Oppenheimer, B. D., Kollmeier, J. A., Weinberg, D. H. 2013, MNRAS, 434, 2645

Davé, R., Oppenheimer, B. D., Finlator, K. M. 2011, MNRAS, 415, 11

Davé, R., Finlator, K. M., Oppenheimer, B. D. 2011, MNRAS, 416, 1354

Dekel, A. et al. 2009, Nature, 457, 451

Dewdney P. E., 2013, Technical report, SKA1 SYSTEM BASELINE DESIGN.

Eisenstein D. J., Hu W., 1998, ApJ, 496, 605

Ewall-Wice, A. et al, 2016, MNRAS, 460, 4320

Fan, X., Carilli, C.L., Keating B. 2006, Annual Review of Astronomy and Astrophysics, 44, 415

Fan X., Strauss M. A., Becker R. H. et al 2006b, AJ, 132, 117

Feroz, F., Hobson, M. P., Bridges, M., 2009, MNRAS, 398, 1601.

Finlator, K. Özel, F. & Davé, R. 2009, MNRAS, 393, 1090

Finlator, K., Davé, R., Özel, F. 2011, 743, 169

Finlator, Kristian; Oh, S. Peng; Davé, R., Özel, F. , 2012, MNRAS, 427, 2464.

Finlator, Kristian; Muñoz, Joseph A.; Oppenheimer, B. D.; Oh, S. Peng; Özel, F. & Davé, 2013, MNRAS, 436, 1818

Finlator, K., Thompson, R., Huang, S., Davé, R., Zackrisson, E., Oppenheimer, B. D. 2015, MNRAS, 447, 2526

Finlator, K., Oppenheimer B. D., Davé, R., Zackrisson, E., Thompson, R., Huang, S., 2016, MNRAS, 459, 2299

Foreman-Mackey D., Hogg D. W., Lang D., Goodman J., 2013, PASP, 125, 306

Villaescusa-Navarro F., Viel M., Datta K. K., Choudhury T. R., 2014, J. Cosmol. Astropart. Phys., 050

Furlanetto, S. R., Zaldarriaga, M., Hernquist, L., 2004, ApJ, 613, 1

Furlanetto, S. R., Oh, S. P., & Briggs, F. H. 2006, PHYS REP, 433, 181

Fumagalli M. et al., 2013, ApJ, 775, 78

Foreman-Mackey, D., 2016, JOSS, 24.

Finkelstein L. S. et al., 2015, ApJ, 810, 71

Ferrarese L., 2002, ApJ, 578, 90

Gabor, J. M. & Davé, R. 2012, MNRAS, 427, 1816

Gabor, J. M. & Davé, R. 2015, MNRAS, 447, 374

Geil, P. M., Wyithe, J. S. B., 2009, MNRAS, 399, 1877

Giallongo E., et al., 2015, A &A, 578, A83

Glikman, E., Djorgovski, S. G., et al., 2011, ApJL, 728, 26

Gnedin, N. Y. 2000, ApJ, 542, 535

Gnedin, N. Y., Jaffe H. A., 2001, ApJ, 551, 1

Gnedin, N. Y.; Kravtsov, A. V.; Chen, H. 2008, ApJ, 672, 765.

Gnedin, N. Y., 2014, ApJ, 793, 29.

Gnedin, N. Y., 2007, ApJ, 673, 1

Grazian, A. et al, 2016, A &A, 585, A48

Grazian, A. et al, 2017, A &A, 602, A18

Greig, B.; Mesinger, A., 2015, MNRAS, 449, 4246.

Greig, B.; Mesinger, A., 2016, MNRAS, 465, 4838.

Gunn, J. E., & Peterson, B. A. 1965, Ap.J., 142: 1633-1641

Haardt, F. & Madau, P. 2001, in Neumann D. M., Van J. T. T., eds, Proc. Clusters of galaxies and the high redshift universe observed in X- rays, Recent results of XMM-Newton and Chandra, XXXVIth Rencon- tres de Moriond , XXIst Moriond Astrophysics Meeting. University of California, Santa Cruz, US.

Haardt, F., Madau, P., 2012, ApJ, 746, 125

Hassan, S. and Davé, R., Finlator, K., Santos, M. G., 2016, MNRAS, 457, 1550

Hassan, S. and Davé, R., Finlator, K., Santos, M. G., 2017, MNRAS, 468, 122

Hassan, S. and Davé, R., Mitra, S., Finlator, K., Ciardi, B., Santos, M. G., 2018, MNRAS, 473, 227

He, W., Akiyama, M. et al, 2017, arXiv:1704.08461

Hopkins P. F., Richards G. T., Hernquist L., 2007, ApJ, 654, 731

Hinshaw, G. et al. 2013, ApJS, 208, 19

Hui, L., Gnedin, N. Y., 1997, MNRAS, 292, 27

Iliev, I. T., Ciardi, B., et al. 2006, MNRAS, 371, 1057

Iliev, I. T.; Mellema, G.; Pen, U.-L.; Merz, H.; Shapiro, P. R.; Alvarez, M. A. 2006, MNRAS, 369, 1625.

Iliev, I. T., Mellema, G., Ahn, K., et al. 2014, MNRAS, 439, 725

Iliev, Ilian T.; Santos, Mario G.; Mesinger, Andrei; Majumdar, Suman; Mellema, Garrelt; 2015 Proc. Sci., Epoch of Reionisation modelling and simulations for SKA. %SISSA, Trieste, PoS (AASKA14) 007.

Japelj et al. 2017, MNRAS, 468, 389

Jiang, L., McGreer, Ian D. et al, 2016, ApJ, 833, 222

Jensen, H. et al, 2013, MNRAS, 435, 460.

Kaurov, A. A. and Gnedin, N. Y. 2014, ApJ 787(2),146.

Kaurov, A. A. and Gnedin, N. Y, 2015, ApJ, 810, 2.

Katz, N., Weinberg, D. H., Hernquist, L. 1996, ApJS, 105, 19

Katz, H, Kimm, T., Sijacki, D., Haehnelt, M., 2016, MNRAS, 468, 4831.

Keating, L. C., Haehnelt, M. G., Becker, G. D., Bolton, J. S., 2014, MNRAS, 438, 1820.

Kennicutt, Jr., R. C. 1998, ARA&A, 36, 189

Kern, N. S., Liu, A., Parsons, A. R., Mesinger, A., Greig, B., 2017, ApJ, 848, 23

Kulkarni, G., Rollinde, E., Hennawi, J. F., Vangioni, E., 2013, ApJ, 772, 93

Kulkarni, G., Choudhury, T. R., Puchwein, E., Haehnelt, M. G., 2016, MNRAS, 463, 2583.

Khaire, V. et al., 2016, MNRAS, 457, 4051

Kim, Y., Im, I. et al, 2015, ApJL, 813, 35

Kulkarni, G., Choudhury, T. R., Puchwein, E., Haehnelt, M. G., 2017, MNRAS, 469, 4283

Kuhlen M., Faucher-Giguére C.-A., 2012, MNRAS, 423, 862

Loeb A., Barkana R., 2001, ARA&A, 39, 19

La Plante, P., Battaglia, N., Natarajan, A., Peterson, J. B., Trac, H., Cen, R., Loeb, A., 2014, ApJ, 789, 31.

Lidz, A., Zahn, O., McQuinn, M., Zaldarriaga, M., Hernquist, L., 2008, ApJ, 680, 962.

Mahmood A., Devriendt G. E. J., Silk J., 2005, MNRAS 359, 1363

Majumdar S., Mellema G., Datta K. K., Jensen H., Choudhury T. R., Bharadwaj S., Friedrich M. M., 2014, MNRAS, 443, 2843

Masters, D., Capak, P., Salvato, M., et al. 2012, ApJ, 755, 169

Ma X. et al, 2015, MNRAS, 453, 960

Mesinger A., Furlanetto S., 2007, ApJ, 669, 663

Madau P., Haardt F., Rees M. J., 1999, ApJ, 514, 648

Madau P., Haardt F., 2015, ApJ, 813, 1

Mao, J., Kim, M., 2016, ApJ, 828, 96

McGreer, I. D., Mesinger, A., D'Odorico, V., 2015, MNRAS, 447, 499.

Meiksin A., Madau P., 1993, ApJ, 412, 34

Mesinger, A. 2010, MNRAS, 407, 1328

Mesinger, A.; Furlanetto, S.; Cen, R. 2011, 411, 955.

Mitra, S., Choudhury T. R., Ferrara A., 2011, MNRAS, 413, 1569.

Mitra, S., Choudhury T. R., Ferrara A., 2012, MNRAS, 419, 1480.

Micheva, G., et al., 2017, MNRAS, 465, 302

Mitra, S., Ferrara, A., & Choudhury, T. R. 2013, MNRAS, 428, L1

Mitra, S., Davé, R., Finlator, K. 2015, MNRAS, 452, 1184

Mitra S, Choudhury T. R., Ferrara A. 2015, MNRAS, 454, L76

Mitra S, Choudhury T. R., Ferrara A. 2016, MNRAS, 473, 1416

Mellema, G., Iliev, I. T., Pen, U.-L., & Shapiro, P. R. 2006, MNRAS, 372, 679

McGreer, I. D., Mesinger, A., D'Odorico, V., 2015, MNRAS, 447, 499.

McQuinn, M., Lidz, A., Zahn, O., et al. 2007, MNRAS, 377, 1043

McQuinn, M., Lidz, A., et al., 2009, ApJ, 694, 2, 842

Mutch S. J. et al, 2016, MNRAS, 462, 250

National Research Council, 2010, The National Academies Press, Washington, DC.

Oppenheimer, B. D. & Davé, R. 2008, MNRAS, 387, 577

Oppenheimer, B. D., Davé R., Finlator, K., 2009, MNRAS, 396, 729

Oñorbe, J., Hennawi, J. F., Lukić, Z., Walther, M., 2017, ApJ, 847, 1

Ouchi, M. et al., 2017, arXiv:1704.07455

Paranjape, A., Choudhury, T. R, Padmanabhan, H., 2016, MNRAS, 460, 1801.

Paciga, G., Albert, J. G., Bandura, K., et al. 2013, MNRAS, 433, 639

Parsa, S., Dunlop, J. S., McLure, R. J., 2017, arXiv:1704.07750

Parsons, A., Pober, J., McQuinn, M., Jacobs, D., Aguirre, J., 2012, ApJ, 753, 81.

Patil, H. A., Yatawatta, S. et al., 2017, ApJ, 838, 1

Pawlik, A. H.; Schaye, J., 2008, MNRAS, 389, 651

Pentericci, L. et al. 2014, ApJ, 793, 113

Pober, J. C., Parsons, A. R. et al, 2013, AJ, 145, 65.

Pober, J. C., Liu, A. et al, 2014, ApJ, 782, 66.

Popping, A., Davé, R., Braun, R., Oppenheimer, B. D. 2009, A&A, 504, 15

Razoumov, A. O., Norman, M. L., Abel, T., & Scott, D. 2002, ApJ, 572, 695

Robertson, B. E., Furlanetto, S. R., Schneider, E., et al. 2013, ApJ, 768, 71

Robertson, B. E., Ellis, R. S., Furlanetto S. R., and Dunlop, J. S., 2015, ApJ, 802,2

Raičević, M., Theuns, T., 2011, MNRAS, 412, L16.

Paardekooper J., Khochfar S., Vecchia D. C., 2015, MNRAS, 451, 2563

Ricci et al., 2017, MNRAS, 465, 1915

Richardson J., et al, 2013, ApJ, 774, 2

Planck Collaboration XIII, Ade, P. A. R., Aghanim, N., et al. 2016, A&A 594, A13.

Planck intermediate results. XLVII, Adam, R., Aghanim, N., et al 2016, A&A 596, A108 .

Prochaska J. X., Worseck G., O'Meara J. M., 2009, ApJ, 705, L113

Santos M. G., Ferramacho L., Silva M. B., Amblard A., Cooray A. 2010, MNRAS, 406, 2421

Sheth R. K., Mo H. J., Tormen G., 2001, MNRAS, 323, 1

Sheth R. K., Tormen G., 1999, MNRAS, 308, 119

Shankar F., Weinberg D. H., Miralda-Escudé J., 2009, ApJ, 690, 1

Shankar, F., Mathur, S., 2007, ApJ, 660, 1051

Shapiro, P. R., Giroux, M. L., 1987, ApJ, 321, 107

Sobacchi E., Mesinger A., 2014, MNRAS, 440, 1662

Schirber M. Bullock J. S., 2003, ApJ , 584, 110

Schaye, J., Carswell, R. F., Kim, T.-S., 2007, MNRAS, 379, 1169

Schaerer, D. 2003, A&A, 397, 527

Schauer, A. T. P., Whalen D. J. ,Glover S. C. O. , Klessen R. S., 2015 MNRAS, 454, 2441

Schmit, C. J, Pritchard, J. R., 2017, arXiv:1708.00011

Smit, R., Bouwens, R. J., Franx, M., Illingworth, G. D., Labbé, I., Oesch, P. A.; van Dokkum, P. G., 2012, ApJ, 756, 14.

So, G. C., Norman, M. L.; Reynolds, D. R.; Wise, J. H. 2014, ApJ, 789, 149.

Somerville, R. S., Hopkins, P. F., Cox, T. J., Robertson, B. E., Hernquist, L., 2008, MNRAS, 391, 481

Somerville, R. S., Popping, G., Trager, S. C. 2015, MNRAS, 453, 4337

Songaila A., 2004, AJ, 127, 2598

Springel, V. & Hernquist, L. 2003, MNRAS, 339, 289

Springel, V. & Hernquist, L. 2003, MNRAS, 339, 312

Springel, V. 2005, MNRAS, 364, 1105

Sunyaev, R. A., & Zeldovich, I. B. 1980, MNRAS, 190, 413

Sutherland, R. S. & Dopita, M. A. 1993, ApJS, 88, 253

Thomas, R. M., Zaroubi, S., Ciardi, B., et al. 2009, MNRAS, 393, 32

Tremaine S., et al., 2002, ApJ, 574, 740

Telfer R. C., Zheng W., Kriss G. A., Davidsen A. F., 2002, ApJ, 565, 773

Tilvi, V., et al, 2013. ApJ, 768, 56.

van Haarlem, M. P. et al, 2013, A&A, 556, 2.

Vasei, K., Siana, B. et al, 2016, ApJ, 831, 1

Vanzella, E., de Barros, S. et al., 2016, ApJ, 825 , 41

Verner, D. A. & Ferland, G. J. 1996, ApJS, 103, 467

Worseck G., et al. 2014, MNRAS, 445, 1745

Worseck G., Prochaska J. X., Hennawi J. F., McQuinn M., 2016, ApJ, 825, 144

Wise, J. H., & Cen, R. 2009, ApJ, 693, 984

Wise, J. H. et al, 2014, MNRAS, 442, 2560

Wyithe, J. S. B., Loeb, A., 2003, ApJ, 595, 2, 614

Yajima H., Choi J.-H., Nagamine K.,2011, MNRAS, 412, 411

Yoshikawa K., Taruya A., Jing Y. P., Suto Y., 2001, ApJ, 558, 2

Qin Y. et al., 2017, MNRAS, 472, 2009

Zel'dovich Y. B., 1970, A&A, 5, 84

Zahn O., Lidz A., McQuinn M., Dutta S., Hernquist L., Zaldarriaga M., Furlanetto
S. R., 2007, ApJ, 654, 12

Zahn O., Mesinger A., McQuinn M., Trac H., Cen R., Hernquist L. E., 2011, MNRAS, 414, 727

Zaroubi S. (2013) The Epoch of Reionization. In: Wiklind T., Mobasher B., Bromm V. (eds) The First Galaxies. Astrophysics and Space Science Library, vol 396. Springer, Berlin, Heidelberg